# MICROWAVE EXCITATION OF ARGON ION AND HELIUM-KRYPTON ION LASERS

Paul J. Dobie

A Thesis Submitted for the Degree of PhD
at the
University of St Andrews

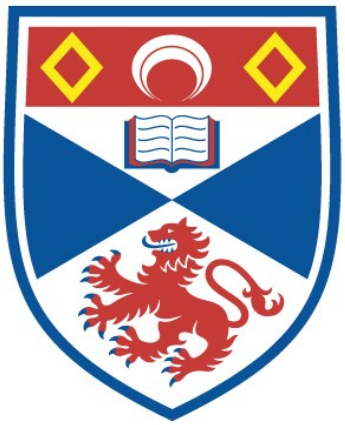

1989

# MICROWAVE EXCITATION OF

# ARGON ION AND HELIUM-KRYPTON ION LASERS

A thesis presented by Paul J. Dobie

to the

University of St.Andrews, Scotland

in application for the degree of

Doctor of Philosophy,

November 1988.

## Thesis Abstract

Pulsed microwave excitation of noble gas ion lasers at frequencies between 3 and 17 GHz is investigated. The advantages of using microwaves instead of conventional DC sources to pump a laser are explained. These include the lower electrode and discharge tube wear due to the oscillating nature of a microwave electric field.

The propagation of microwave radiation in an ionised gas is examined. At the frequencies used, the skin depth of an Argon ion laser discharge is shown to be approximately 1 mm, indicating good microwave power absorption. The dependence of the microwave power absorption on the frequency is shown to be weak. Microwave transmission at a dielectric/gas-discharge boundary, similar to those in the laser coupling structures used, is found to be around 1% of the incident power. It is suggested that for maximum laser efficiency, microwave power should be introduced directly into the gas discharge.

Two microwave coupling structure designs for supplying microwave power to the laser discharges are described. The first of these, a waveguide coupler device based on the 3dB branch guide coupler, produces a transverse electric field across the laser tube. The procedure used to design a branch guide coupler using a Chebyshev impedance taper and T-junction discontinuity corrections is outlined, and a description of the entire laser coupling structure is given. The second design comprises a helix wrapped round the laser tube and produces an axial electric field. The electric field distribution around a helix is calculated as a function of helix parameters and the effects of surrounding objects are considered. The best helix dimensions are found for optimum laser operation.

The characteristics of conventional Argon ion and Helium-Krypton

ion lasers are given. No significant differences between conventional noble gas ion lasers and the microwave excited lasers reported here are observed. At the input powers used (~100 kW peak, 1 uS pulses, 1000 pps), 100 mW, 1 uS and 30 mW, 5 uS laser pulses are observed from Argon and Helium-Krypton gas mixtures, respectively. The transverse and axially excited lasers perform equally well.

To my parents and grandparents,
& the view of Glasgow University
from the Kelvin Hall.

## Declaration

I hereby certify that this thesis has been composed by me, and is a record of work done by me, and has not previously been presented for a higher degree.

This research was carried out in the Physical Sciences Laboratory of St.Salvador's College, in the University of St.Andrews, Scotland, and at EEV Limited, Lincoln, England, under the supervision of Dr.A.Maitland.

Paul J. Dobie.

## Certificate

I certify that Paul J. Dobie has spent nine terms at research work in the Physical Sciences Laboratory of St.Salvador's College, in the University of St.Andrews, under my direction, that he has fulfilled the conditions of Ordinance No. 16 (St.Andrews) and that he is qualified to submit this thesis in application for the Degree of Doctor of Philosophy.

A. Maitland

Research Supervisor.

## Author's Career

Paul John Dobie was born in Falkirk, Scotland in 1963. He attended Corsehill Primary School, Kilwinning and then Ravenspark Academy, Irvine. He read Astronomy and Physics at the University of Glasgow (1981-85). As an employee of EEV Limited, Lincoln, he has spent the last three years (1985-88) studying the microwave excitation of lasers. This research was carried out for a Ph.D. degree in conjunction with the University of St.Andrews.

## Acknowledgements

I would like to thank the following people for the help they have given me during the last three years whilst I have been preparing this thesis. Arthur Maitland of the University of St.Andrews for his boundless energy and enthusiasm, and for his guidance and assistance. John Broadhead of EEV Limited, Lincoln for initiating the project and maintaining his support throughout its duration. John Duff (who succeeded John Broadhead) for continuing the support. The following staff from EEV: Janet Hewitt (microwave discharge theory), Alistair Ross (computing), Mark Hutcheon, Pete Hackney and Ian Peterkin (microwave theory and techniques), Tony Elvins and Neil Turney (helix research), Joanne Hurley (library), Colin Taylor (gas handling) and Graeme Clark (laser theory and techniques). From St.Andrews: the three Andys, Harvey, Flinn and Kidd, Graham Smith, Ian Park, Natalie Ridge and Colin Wilson for many interesting and occasionally volatile laboratory, corridor and coffee table discussions on Physics (and the rest). Tom McQueen of the Physics stores at St.Andrews for his help up to the last bolt. Also the workshop staff at both Lincoln and St.Andrews for producing good quality engineering despite excessive demands upon their time. Elizabeth Clingan for her loyal support.

Many of the above mentioned people have not only assisted me with the technical aspects of this project, but have also given me great friendship, helping make the last three years very good fun indeed.

## Contents

## Chapter 1 Introduction

This thesis reports research carried out to study the microwave excitation of noble gas ion lasers. The stress on the discharge tube and electrodes of a microwave excited laser is less severe than for the DC-excited case because of the oscillating nature of the microwave field. Thus, the discharge structure can be made to a simpler design than that used in a conventional DC-excited laser.

Continuous and pulsed DC-excitation are by far the most common techniques used to pump gas lasers. Other techniques include excitation by radio frequency (RF) and microwave electric fields. Radio frequency excitation uses an oscillating electric field of frequency between 1 KHz and 1 GHz and has the advantage that no electrodes in contact with the gas are required. Excitation at radio frequencies is used commercially in $CO_2$ lasers. When the frequency of the exciting electric field exceeds 1 GHz, we enter the realm of the microwave discharge. The processes occurring in a microwave discharge differ somewhat from those found in DC and RF discharges [1]-[2].

### The potential of microwave excitation

Microwave sources and their power supplies are easy and safe to use and microwave systems are generally well understood. The laser coupling structure operates at earth potential and all the high voltages are contained within the structure. This is unlike conventional lasers which often have lethal voltages at the electrodes.

Many lasers operate at high current densities, and normally the electrodes and the discharge tube have to be specially designed to

withstand the resulting thermal and physical stresses. The discharge tube of a microwave excited laser can be made to a much simpler design than many of the currently available tubes, because often a microwave discharge can be excited without the use of internal electrodes. Even if internal electrodes are used, the stress which they have to withstand is much less than in a conventional laser. This is because a microwave field has a high frequency of oscillation, and only a small percentage of the active electrons in the discharge actually interact with the electrodes, (the majority oscillate to and fro between them). This is not the case for DC and RF discharges where electrons are continually swept out of the discharge region onto the electrodes. Electron collisions cause damage to the electrodes and container walls and can result in the release of impurities into the laser gas.

As reported in [3]-[19], microwave excitation of Xenon-Chloride, Helium-Neon, Carbon Dioxide, Helium-Krypton, Xenon and Argon has been carried out at frequencies up to 10 GHz, but as far as the author is aware, no research has been carried out at higher frequencies. This thesis concentrates on microwave excitation at frequencies from 3 to 17 GHz of noble gas ion lasers and particular attention is given to pulsed Argon ion and Helium-Krypton ion lasers.

## Commercial considerations

A commercial microwave excited laser must be able to compete in price and performance with the currently available DC-excited lasers. Magnetrons, which are one of the cheapest high power microwave sources, can operate in either a pulsed or a CW mode. A typical DC-excited noble gas ion laser has an efficiency of less than 1% and so the introduction of a magnetron with an efficiency of around 60% has little effect, in

practical terms, on the overall system efficiency. The limiting parameter therefore, is the cost of the magnetron and its supply. The power supply of a pulsed magnetron is fairly complicated due to the DC-pulse forming elements required to drive it. The use of a CW magnetron is thus preferable on a cost basis. Microwave oven magnetrons, which operate at 2.45 GHz, and their associated power supplies, are particularly cheap, and these are probably the best sources to use. The use of higher frequencies has the advantage that smaller discharge structures can be used. Unfortunately high frequency magnetrons are more expensive than their low frequency counterparts thus limiting their commercial viability. Assuming typical laser efficiencies, a 1 kW, CW, 2.45 GHz magnetron could be used to drive a laser in the low to medium power range, at a cost comparable with current commercial systems.

The discharge tubes of a microwave excited laser can be easily interchanged due to their simplicity and low cost. Once a suitable microwave source and discharge structure are available, a tube containing any gas fill can be introduced. In this way, it should be possible to produce a range of laser tubes covering most of the common gas lasers.

The concept of using microwave power to drive a laser discharge has been outlined and in order to fulfill it, three things have to be achieved. Firstly it must be shown that a microwave discharge is capable of exciting a laser discharge as efficiently as, or better than, a DC-discharge. Secondly, a suitable discharge structure has to be developed which efficiently supplies microwave power to the laser discharge. And finally, the laser prototype must be able to meet all the major performance specifications of currently available commercial lasers. With regard to the final point, much of the long term performance of a gas laser depends on the quality of the gas fill and the tube processing.

Experience in this area would be required for the speedy development of a commercially acceptable device. In the chapters that follow, the properties of a microwave discharge and various coupling structures will be examined, to assess their suitability for exciting a laser.

## Thesis format

In order to assess the suitability of a microwave discharge for laser excitation, chapter 2 begins with a discussion of microwave propagation and absorption in an ionised gas. The situation is studied from two viewpoints. Firstly, a macroscopic treatment is applied to study microwave power propagation in an ionised gas. This analysis is then extended to consider the reflection of a wave at a dielectric/gas-discharge boundary. Secondly, a microscopic treatment is considered involving the solution of the Boltzmann distribution equation.

Chapters 3 and 4 describe the structures used to couple microwave power into the laser tube. The first of these chapters is devoted to the design of a structure, composed of three separate 3dB-microwave couplers connected together in series, which produces a transverse electric field. The design procedure for a single coupler is first outlined and then the entire structure is described. Similarly the following chapter describes a helical structure used to produce a longitudinal electric field. To find the best helix parameters, the field distributions around a free-standing helix, and the helix used in the coupling structure configuration are considered.

In chapter 5, the development history and some applications of noble gas ion lasers are given, followed by a description of the general characteristics of pulsed Argon ion and Helium-Krypton ion lasers. Chapter 6 contains data from experiments carried out on the microwave

excited Argon ion and Helium-Krypton ion laser prototypes, using either a 3, 10 or 17 GHz microwave source, with either a transverse or longitudinal electric field. A time-resolved analysis of the spontaneous emission spectra is carried out to determine the excitation mechanisms, and the dependance of the laser outputs on tube diameter, gas fill and input microwave power characteristics are examined.

The concluding chapter briefly summarises the findings of the previous chapters.

## References

[1] A.D.MacDonald
"Microwave Breakdown in Gases."
J.Wiley & Sons inc., 1966.

[2] S.C.Brown
"Basic Data of Plasma Physics."
Press of MIT and J.Wiley & Sons inc., 1959.

[3] P.J.K.Wisoff et al.
"Improved performance of the microwave-pumped XeCl laser."
IEEE J. Qu. Elect. QE-18 1839 1982.

[4] A.J.Mendelsohn et al.
"A microwave-pumped XeCl laser."
Appl. Phys. Letts. 38 603 1981.

[5] J.F.Young et al.
"Microwave excitation of excimer lasers."
Laser Focus p.63, Apr. 1982.

[6] S.A.Ahmed & R.Kocher
"Microwave electron cyclotron resonance pumping of a gas laser."
Proc. IEEE 52 1737 1964.

[7] V.N.Konenkov & V.A.Koshel'kov
"Study of a microwave-excited He-Ne laser."
Radio Eng. & Electron. Phys. (USA) 26 70 1981.

[8] Ya.N.Muller & V.A.Khrustalev
"Determination of unsaturated gain of an He-Ne laser with transverse microwave pumping."
Sov. J. Qu. Elect. 11 401 1981.

[9] K.G.Handy & J.E.Brandelik
"Laser generation by pulsed 2.45 GHz microwave excitation of $CO_2$."
J. Appl. Phys. 49 3753 1978.

[10] O.S.Vasyutinskii et al.
"Pulsed microwave discharge as a pump for the $CO_2$ laser."
Sov. Phys.-Tech. Phys. 23 189 1978.

[11] C.P.Christensen
"Pulsed transverse electrodeless discharge excitation of a $CO_2$ laser."
Appl. Phys. Letts. 34 211 1979.

[12] I. Kato et al.
"Output power characteristics of microwave-pulse-excited He-$Kr^+$ ion laser."
Jap. J. Appl. Phys. 14 2001 1975.

[13] I.Kato et al.
"Spectroscopic studies of microwave-pulse-excited He-$Kr^+$ ion laser."
Jap. J. Appl. Phys. 16 1219 1977.

[14] I.Kato et al.
"Time variation of internal plasma parameters in microwave-pulse-excited He-$Kr^+$ ion laser."
Jap. J. Appl. Phys. 16 597 1977.

[15] J.P.Goldsborough & A.L.Bloom
"New CW ion laser oscillation in microwave excited Xenon."
IEEE J. Qu. Elect. QE-3 96 1967.

[16] S.F.Paik & J.E.Creedon
"Microwave-excited ionised Argon laser."
Proc. IEEE 56 2086 1968.

[17] J.P.Goldsborough et al.
"RF induction excitation of CW visible laser transitions in ionised gases."
Appl. Phys. Letts. 8 137 1966.

[18] V.F.Kravchenko et al.
"Ion lasing utilizing microwave-excited Strontium vapour."
Sov. J. Qu. Elect. 14 725 1984.

[19] J.E.Brandelik & G.A.Smith
"Br, C, Cl, S and Si laser action using a pulsed microwave discharge."
IEEE J. Qu. Elect. QE-16 7 1980.

## Chapter 2 The Microwave Discharge

This chapter examines the properties of a gas discharge excited by a microwave field. Among the points to be considered in this chapter are, the propagation of microwave radiation in an ionised gas, reflection and transmission at a boundary, the motion of electrons in a microwave field, the significance of the ratio of collision frequency to microwave frequency, the electron energy distribution function and the microwave power absorption efficiency. These will be compared with the requirements for an efficient noble gas ion laser. Throughout this chapter the differences between a microwave-excited discharge and the more conventional DC and RF discharges will be emphasised.

### Propagation of microwave radiation in an ionised gas

To excite a microwave discharge most efficiently, the gas must absorb all the incident microwave power. One way of studying microwave absorption is to consider the propagation of microwave radiation through an ionised gas. This is essentially a macroscopic treatment to find the microwave power absorption and penetration into a gas discharge. In order to study propagation through an ionised gas, the simpler cases of non-conducting and conducting media will first be considered.

(i) Propagation in a non-conducting medium

In a non-conducting medium the electrical conductivity $\sigma$ is zero and there are no free charges. Maxwell's equations therefore can be written as [1],

$$\begin{aligned} \underline{\nabla} \cdot \underline{E} &= 0 \\ \underline{\nabla} \cdot \underline{B} &= 0 \\ \underline{\nabla} \times \underline{E} &= -\partial \underline{B}/\partial t \\ \underline{\nabla} \times \underline{B} &= \partial \underline{E}/\partial t, \end{aligned} \tag{2.1}$$

where E is the electric field intensity, B is the magnetic induction, and $\mu$ and $\epsilon$ are the permeability and permittivity of the medium. By assuming that the medium is non-magnetic and that the electric and magnetic fields have an $e^{i\omega t}$ variation, eqs 2.1 can be used to derive the wave equations,

$$\begin{aligned} \underline{\nabla}^2 \underline{E} + \mu_o \varepsilon \omega^2 \underline{E} &= 0 \\ \underline{\nabla}^2 \underline{H} + \mu_o \varepsilon \omega^2 \underline{H} &= 0, \end{aligned} \tag{2.2}$$

where H is the magnetic field intensity and $\omega$ is the angular frequency of the field. Assuming plane wave propagation in the z-direction, a solution of the electric field wave equation is,

$$E_x = E_{ox} \exp[i(\omega t - \beta z)]. \tag{2.3}$$

The maximum electric field intensity is $E_{ox}$ and $\beta$ $(= \omega\sqrt{\mu_o \varepsilon})$ is the phase constant (here equal to the propagation constant). The intrinsic impedance $\eta$ of the medium is defined as,

$$\eta = E_x/H_y, \tag{2.4}$$

and, by using eqs 2.1, this can be written as,

$$\eta = \sqrt{\mu_o/\varepsilon}. \tag{2.5}$$

It can be seen here that $\eta$ is a real quantity depending upon the permittivity of the medium. Here $E_x$ and $H_y$ are in phase, and in free space we have, $\eta = \sqrt{\mu_o/\varepsilon_o} = 377\ \Omega$.

(ii) Propagation in a conducting medium

As with (i) above there are no free charges, but the conductivity is given by,

$$\underline{J} = \sigma \underline{E}, \tag{2.6}$$

where J is the current density. Equations 2.1 must now be modified to accommodate this, and the Curl $\underline{B}$ equation becomes,

$$\underline{\nabla} \times \underline{B} = i\omega\mu_o(\varepsilon - i\sigma/\omega)\underline{E}. \tag{2.7}$$

Here the real permittivity for the non-conducting medium has been replaced by a complex permittivity and the electric field wave equation now becomes,

$$\underline{\nabla}^2\underline{E} + \mu_o(\varepsilon - i\sigma/\omega)\omega^2\underline{E} = 0. \tag{2.8}$$

This can be re-written as

$$\underline{\nabla}^2\underline{E} - \gamma^2\underline{E} = 0, \tag{2.9}$$

where the propagation constant $\gamma$ is given by,

$$\gamma = i\omega\sqrt{[\mu_o(\varepsilon - i\sigma/\omega)]}, \tag{2.10}$$

and eq 2.9 has a solution,

$$E_x = E_{ox} \exp[-\gamma z] \exp[i\omega t]. \tag{2.11}$$

Unlike the previous case, the propagation constant is now a complex quantity which can be expressed as $\alpha + i\beta$ and eq 2.11 can be written as

$$E_x = E_{ox} \exp[-\alpha z] \exp[i(\omega t - \beta z)] \tag{2.12}$$

The attenuation constant $\alpha$ represents the power loss from the wave due to ohmic heating of the medium. Equation 2.12 describes the electric field as it passes through the conducting medium. It can be seen that there is an exponential attenuation term and a propagation term, and these are both functions of the permittivity $\varepsilon$, the conductivity of the medium $\sigma$, and the frequency of the field. By solving eq 2.10, $\alpha$ and $\beta$ can be written as,

$$\begin{aligned} \alpha &= \omega\sqrt{\mu_o\varepsilon/2}\ \ [\sqrt{1 + (\sigma/\omega\varepsilon)^2} - 1]^{0.5} \\ \beta &= \omega\sqrt{\mu_o\varepsilon/2}\ \ [\sqrt{1 + (\sigma/\omega\varepsilon)^2} + 1]^{0.5} . \end{aligned} \tag{2.13}$$

As the conductivity $\sigma$ approaches zero, these equations reduce down to those for a non-conducting medium with $\alpha$ tending to zero and $\beta$ tending to $\omega\sqrt{\mu_o\varepsilon}$.

The exponential attenuation term is often expressed in terms of the skin depth $\delta$ which is the distance the field penetrates before its amplitude is reduced to 1/e (~37%) of its original value. Skin depth may therefore be defined as,

$$\delta = 1/\alpha. \tag{2.14}$$

The intrinsic impedance is now complex and is given by,

$$\eta = \sqrt{\mu_o/(\varepsilon - i\sigma/\omega)}. \tag{2.15}$$

This can be written in polar form as,

$$\eta = \eta' \exp[i\phi]. \tag{2.16}$$

Here, the electric field leads the magnetic field by $\phi$. For a good conductor we have, $\phi = \pi/4$.

(iii) Propagation in an ionised gas

The ionised gas under consideration here is assumed to be neutral with a uniform electron distribution. In this case the current density depends on the properties of the free electrons of the gas. The equation of motion of the average electron is,

$$m \frac{d\bar{\underline{v}}}{dt} = e\underline{E} - m\bar{\underline{v}}\nu_m , \tag{2.17}$$

where m and e are the electron mass and charge respectively. The mean electron velocity is $\bar{\underline{v}}$, and $\nu_m$ is the collision frequency for momentum transfer. For an exp(i$\omega$t) dependance of $\underline{E}$ and $\bar{\underline{v}}$, the equation has a solution,

$$\bar{\underline{v}} = \frac{e\underline{E}}{m(\nu_m + i\omega)} . \tag{2.18}$$

The current density in this case, given by $\underline{J} = N_e e\bar{\underline{v}}$, can now be written as

$$\underline{J} = \frac{N_e e^2 \underline{E}}{m(\nu_m + i\omega)} . \tag{2.19}$$

The curl equation of 2.1 and 2.7 is now written as,

$$\underline{\nabla} \times \underline{B} = i\omega\mu_o \left[ \left[ \varepsilon_o - \frac{N_e e^2}{m(\nu_m^2 + \omega^2)} \right] - i\left[ \frac{\nu_m}{\omega} \frac{N_e e^2}{m(\nu_m^2 + \omega^2)} \right] \right] \underline{E} \,. \tag{2.20}$$

The wave equation has the same form as eq 2.9, but this time $\gamma$ is given by,

$$\gamma^2 = \frac{-\omega^2}{c^2} \left[ \left[ 1 - \frac{\omega_p^2}{\omega^2 + \nu_m^2} \right] - i\left[ \frac{\nu_m}{\omega} \frac{\omega_p^2}{\omega^2 + \nu_m^2} \right] \right] . \tag{2.21}$$

where $\omega_p$ is the plasma frequency defined by,

$$\omega_p^2 = \frac{N_e e^2}{\varepsilon_o m} \,, \tag{2.22}$$

and c is the speed of light $(=\sqrt{1/\mu_o\varepsilon})$.

By following the same procedure that was used to derive eqs 2.13, eq 2.21 can be used to find $\alpha$ and $\beta$. This yields the following expressions,

$$\alpha^2 = \frac{-\omega^2}{2c^2} \left[ 1 - \frac{\omega_p^2}{\omega^2 + \nu_m^2} \right] + \frac{\omega^2}{2c^2} \left[ \left[ 1 - \frac{\omega_p^2}{\omega^2 + \nu_m^2} \right]^2 + \left[ \frac{\nu_m}{\omega} \right]^2 \frac{\omega_p^4}{(\omega^2 + \nu_m^2)^2} \right]^{0.5} \tag{2.23}$$

$$\beta^2 = \frac{\omega^2}{2c^2} \left[ 1 - \frac{\omega_p^2}{\omega^2 + \nu_m^2} \right] + \frac{\omega^2}{2c^2} \left[ \left[ 1 - \frac{\omega_p^2}{\omega^2 + \nu_m^2} \right]^2 + \left[ \frac{\nu_m}{\omega} \right]^2 \frac{\omega_p^4}{(\omega^2 + \nu_m^2)^2} \right]^{0.5} .$$

The wave equation has a solution of the form, (which is the same as the conducting medium case),

$$E_x = E_{ox} \exp[-\alpha z] \exp[i(\omega t - \beta z)] \,, \tag{2.24}$$

where $\alpha$ and $\beta$ from eq 2.23 are used. The attenuation constant represents the power loss from the wave due to excitation of the ionised gas. The phase constant $\beta$ is used to give the refractive index n of the gas where n is given by $(c/\omega)\beta$. Once again the intrinsic impedance $\eta$ is complex and the electric and magnetic fields are out of phase.

By examining eqs 2.23, a simple case can be considered where the collision frequency is much less than the angular frequency of the microwave field. Here, if the angular frequency is greater than the plasma frequency, the attenuation constant tends to zero and the wave

can propagate unhindered through the medium. When, however, the angular frequency is less than the plasma frequency, the phase constant tends to zero and the wave is said to be below the cutoff frequency. Here, the wave is attenuated exponentially. Generally, high frequency fields find it easier to propagate through an ionised gas.

This chapter is concerned primarily with an ion laser discharge with an electron density of around $10^{20}$ $m^{-3}$. This gives a plasma frequency in excess of 500 GHz and so for the purposes of this chapter, the angular frequency of the field is always considerably less than the plasma frequency. Figures 2.1 and 2.2 contain graphs of the attenuation and phase constants as a function of the $\omega/\nu_m$ ratio, with electron density $N_e$, as a parameter. The skin depth $\delta$ which is the inverse of the attenuation coefficient is plotted on fig 2.3. It can be seen from figs 2.1 and 2.3, that when $\omega/\nu_m$ is greater than 1, the attenuation constant remains approximately fixed.

Up until now, the effect of any discontinuities upon the propagation of a microwave signal has been ignored. In some cases however, these can be very significant indeed, as will be seen in the next section.

## Wave transmission and reflection at a boundary

In the previous section, the behaviour of a wave as it passes through a medium was described. The propagation of such a wave can be affected by sudden changes in the properties of the medium. The effect of such discontinuities will be outlined here. This is of interest because, in the discharge devices to be described in chapters 3 and 4 of this thesis, the microwave power has to pass across a free-space/glass-tube boundary and then a glass-tube/gas-discharge boundary. The

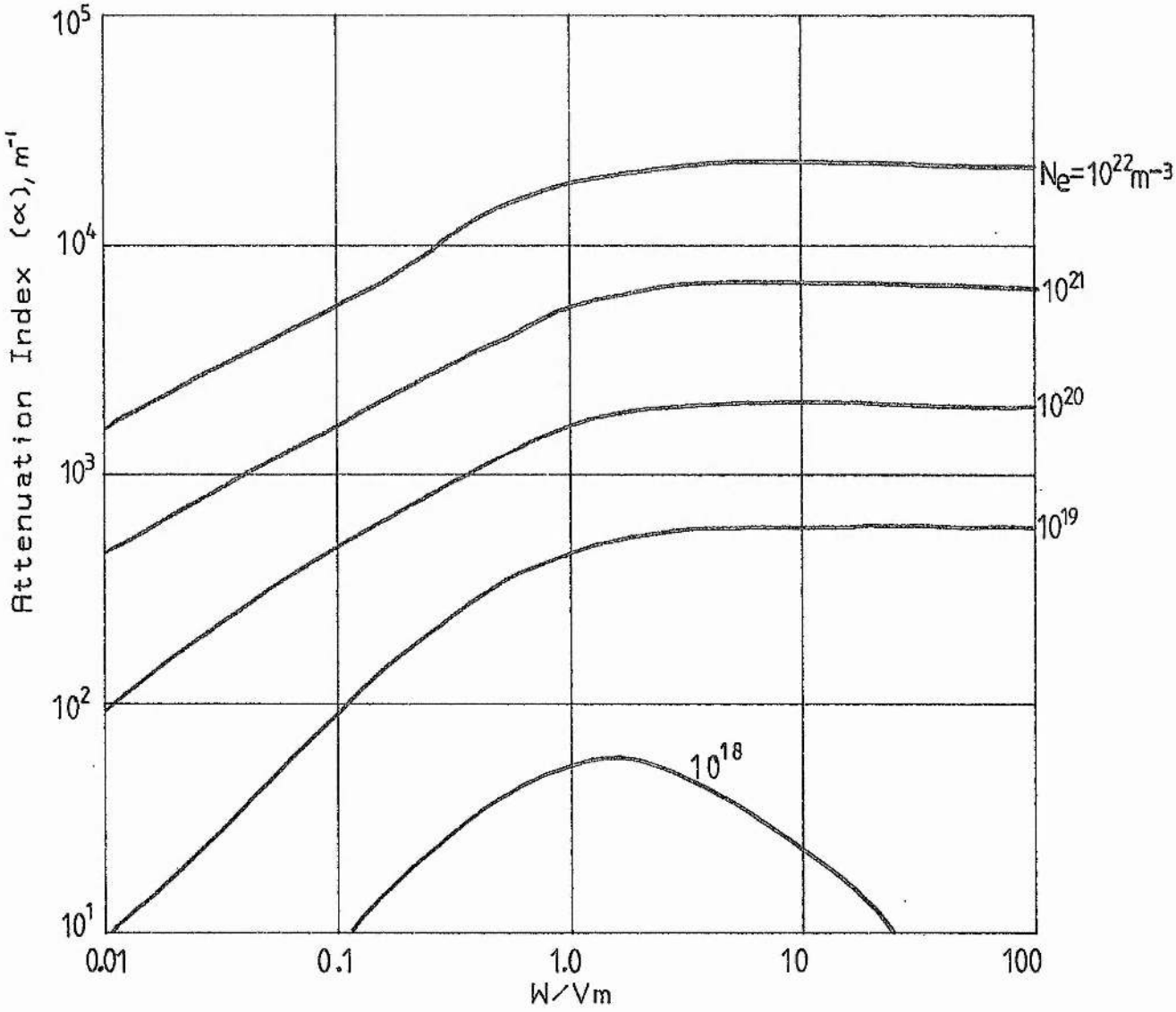


FIGURE 2.1

ATTENUATION INDEX AGAINST W/Vm

FOR AN IONISED GAS

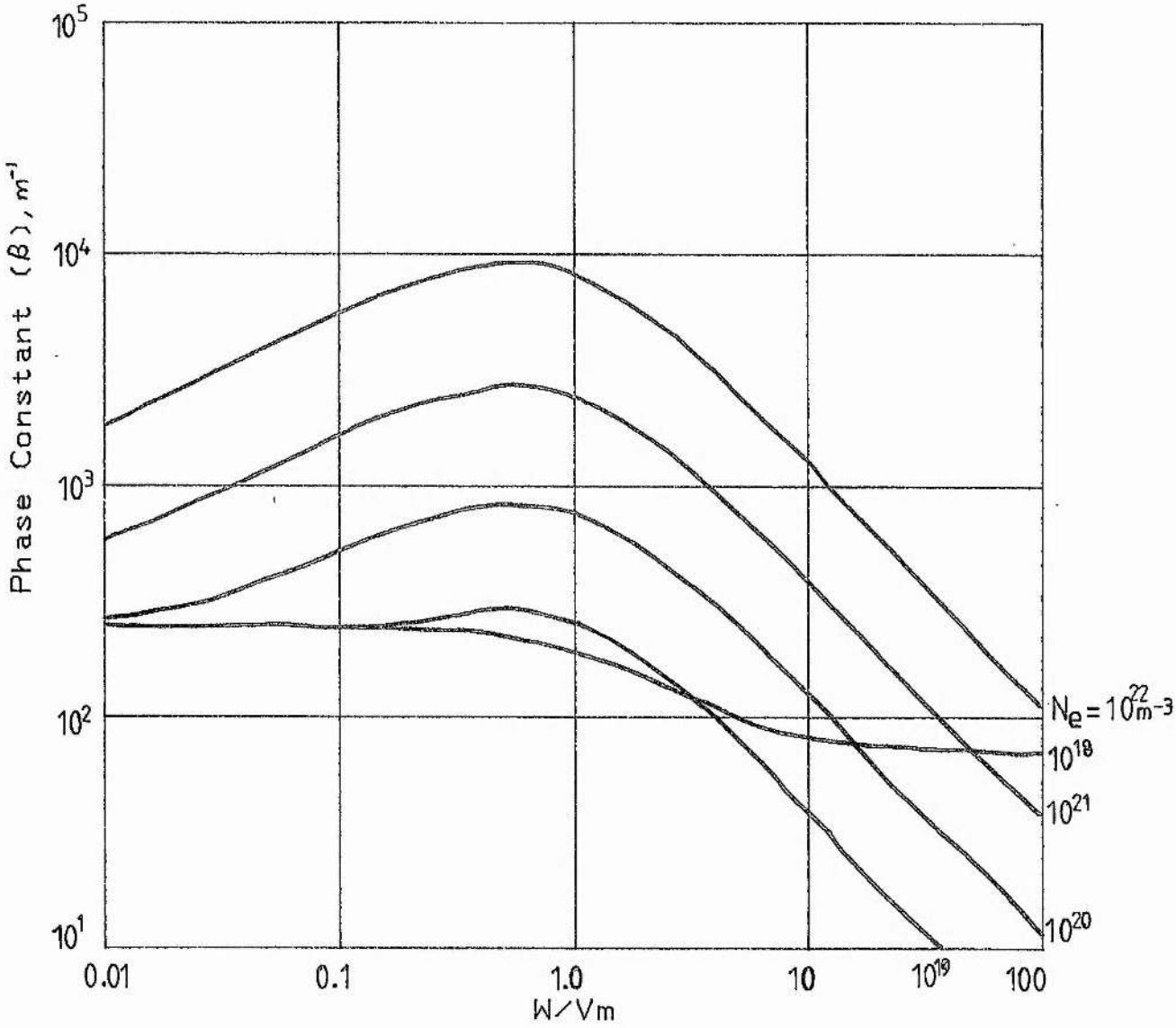


FIGURE 2.2

PHASE CONSTANT AGAINST W/Vm

FOR AN IONISED GAS

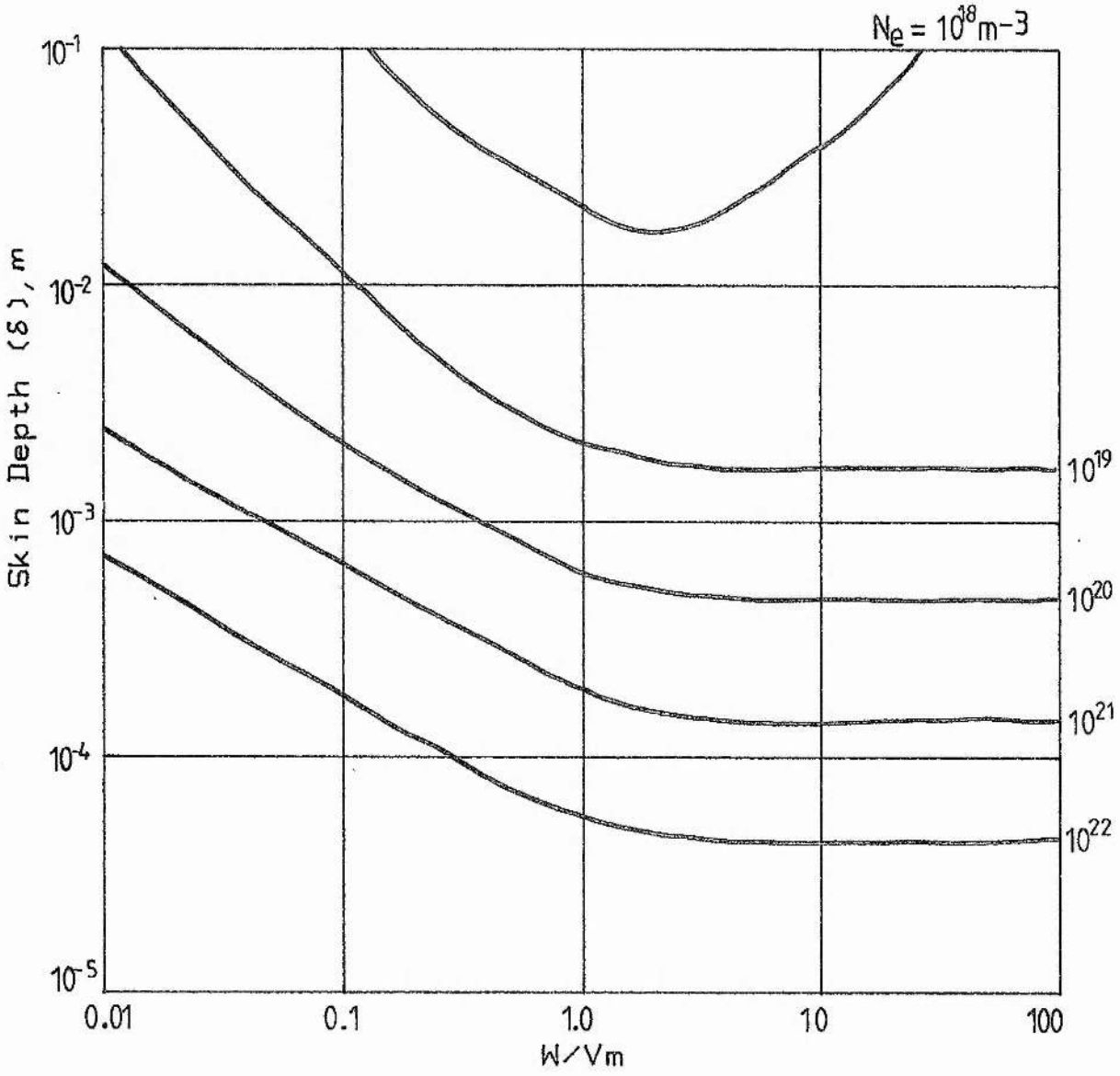


FIGURE 2.3
SKIN DEPTH AGAINST W/Vm
FOR AN IONISED GAS

absorption of a microwave signal propagating in an ionised gas has already been discussed, but what is required here is an indication of how much of the incident power actually gets into the gas discharge.

In order to measure the power which penetrates a free-space/gas-discharge boundary, a plane TEM mode wave will be considered which is incident upon a uniform plane boundary. In the discharge geometries of interest (see chapters 3 and 4), the incident waves and boundaries are never plane. Nevertheless, the case considered here is good to a first approximation and is sufficient to illustrate the principle, and highlight a serious problem associated with the discharge configurations used.

The fields to be examined can be expressed in the form

$$E = E_o' \, e^{-\gamma z}, \tag{2.25}$$

where $E_o'$ is the complex amplitude which incorporates time and phase information as well as the real amplitude. It is given by,

$$E_o' = E_o \exp[i(\omega t + \phi)] \, . \tag{2.26}$$

The fields incident (i) upon the boundary can be written as,

$$\begin{aligned} E_{xi} &= E_{oi}' \, e^{-\gamma_1 z} \\ H_{yi} &= (E_{oi}'/\eta_1) \, e^{-\gamma_1 z} \, . \end{aligned} \tag{2.27}$$

The resulting transmitted (t) and reflected (r) fields now become,

$$\begin{aligned} E_{xt} &= E_{ot}' \, e^{-\gamma_2 z} \\ E_{xr} &= E_{or}' \, e^{\gamma_1 z} \\ H_{yt} &= (E_{ot}'/\eta_2) \, e^{-\gamma_2 z} \\ H_{yr} &= -(E_{or}'/\eta_1) \, e^{\gamma_1 z} \, . \end{aligned} \tag{2.28}$$

Here, the propagation constant $\gamma_n$ can be complex depending upon the nature of the medium n.

There are two specific situations which can be considered, one where the electric field is parallel to the plane of incidence, and the

other where it is perpendicular. The tangential electric and magnetic fields are continuous across the boundary at z = 0, and when the electric field is parallel to the plane of incidence, the boundary conditions are,

$$E'_{oi}\cos\theta_i + E'_{or}\cos\theta_i = E'_{ot}\cos\theta_t$$
$$E'_{oi}/\eta_1 - E'_{or}/\eta_1 = E'_{ot}/\eta_2. \tag{2.29}$$

The angle of incidence or transmission with respect to the normal at the plane boundary is $\theta_{i,t}$. Solving these equations, the amplitudes of the transmitted and reflected electric fields are given by

$$E'_{or} = \frac{(\eta_2/\eta_1)\cos\theta_t - \cos\theta_i}{(\eta_2/\eta_1)\cos\theta_t + \cos\theta_i} E'_{oi}$$
$$E'_{ot} = \frac{2(\eta_2/\eta_1)\cos\theta_i}{(\eta_2/\eta_1)\cos\theta_t + \cos\theta_i} E'_{oi}. \tag{2.30}$$

When the electric field is perpendicular to the plane of incidence, the equations are,

$$E'_{or} = \frac{(\eta_2/\eta_1)\cos\theta_i - \cos\theta_t}{(\eta_2/\eta_1)\cos\theta_i + \cos\theta_t} E'_{oi}$$
$$E'_{ot} = \frac{2(\eta_2/\eta_1)\cos\theta_i}{(\eta_2/\eta_1)\cos\theta_i + \cos\theta_t} E'_{oi}. \tag{2.31}$$

The reflection and transmission coefficients R and T, are used to express the flow of energy across a boundary. They are defined as ratios of the power per unit area across the boundary. The power per unit area is given by the time averaged Poynting vector $\underline{S}_{av}$ which is written as,

$$\underline{S}_{av} = 1/2\ \mathrm{Re}(\underline{E} \times \underline{H}^*). \tag{2.32}$$

Here, Re represents the "real part of", and * denotes the complex conjugate. Assuming that $\underline{E}$ and $\underline{H}$ run along the x and y-axes respectively, $\underline{S}_{av}$ points along the z-axis. From eqs 2.4 and 2.5, $H_y$ is given by,

$$H_y = (\sqrt{\epsilon_r}/377)\ E_x, \tag{2.33}$$

where $\epsilon_r$ is the relative permittivity of the medium. Assuming that the

boundary between two dielectrics lies on the x,y-plane and that the plane of incidence is normal to this, the respective powers per unit area of the incident, reflected and transmitted waves are given by,

$$S_i = 1/2\ (\sqrt{\varepsilon_1}/377)\ (E'_{oi})^2$$
$$S_r = 1/2\ (\sqrt{\varepsilon_1}/377)\ (E'_{or})^2 \qquad (2.34)$$
$$S_t = 1/2\ (\sqrt{\varepsilon_2}/377)\ (E'_{ot})^2.$$

The reflection and transmission coefficients, defined as $|S_r/S_i|$ and $|S_t/S_i|$, respectively, can now be written as,

$$R = \left[ \frac{(\varepsilon_1/\varepsilon_2)^{1/2} - 1}{(\varepsilon_1/\varepsilon_2)^{1/2} + 1} \right]^2$$
$$T = \frac{4(\varepsilon_1/\varepsilon_2)^{1/2}}{[(\varepsilon_1/\varepsilon_2)^{1/2} + 1]^2} \quad . \qquad (2.35)$$

These functions have been graphed on fig 2.4 at a free-space/dielectric boundary. It can be seen that a considerable proportion of the incident power is transmitted across the boundary provided that the difference between $\varepsilon_1$ and $\varepsilon_2$ is not too large.

The same is not always true at a glass/gas-discharge boundary. The relative permittivity of an ionised gas is a complex quantity, as given by eq 2.20. From eq 2.33 it can be seen that $E_x$ and $H_y$ are out of phase and that $E_x/H_y$ is complex. For an ionised gas eq 2.32 can be re-written as,

$$\underline{S}_{av} = 1/2\ \mathrm{Re}[(\underline{E}_{or} + j\underline{E}_{oi})\ X\ (\underline{H}_{or} - j\underline{H}_{oi})]\ , \qquad (2.36)$$

where $\underline{E}_{or}$, $\underline{E}_{oi}$, $\underline{H}_{or}$ and $\underline{H}_{oi}$ are real functions of z as given by eqs 2.24 to 2.26. By assuming that $E_x$ is real, the time averaged Poynting vector can be written as,

$$\underline{S}_{av} = 1/2\ (\varepsilon_o/\mu_o)^{1/2}\ \mathrm{Re}[\sqrt{\varepsilon_r}]\ E_x^2\ . \qquad (2.37)$$

For a glass/gas-discharge boundary, R and T become,

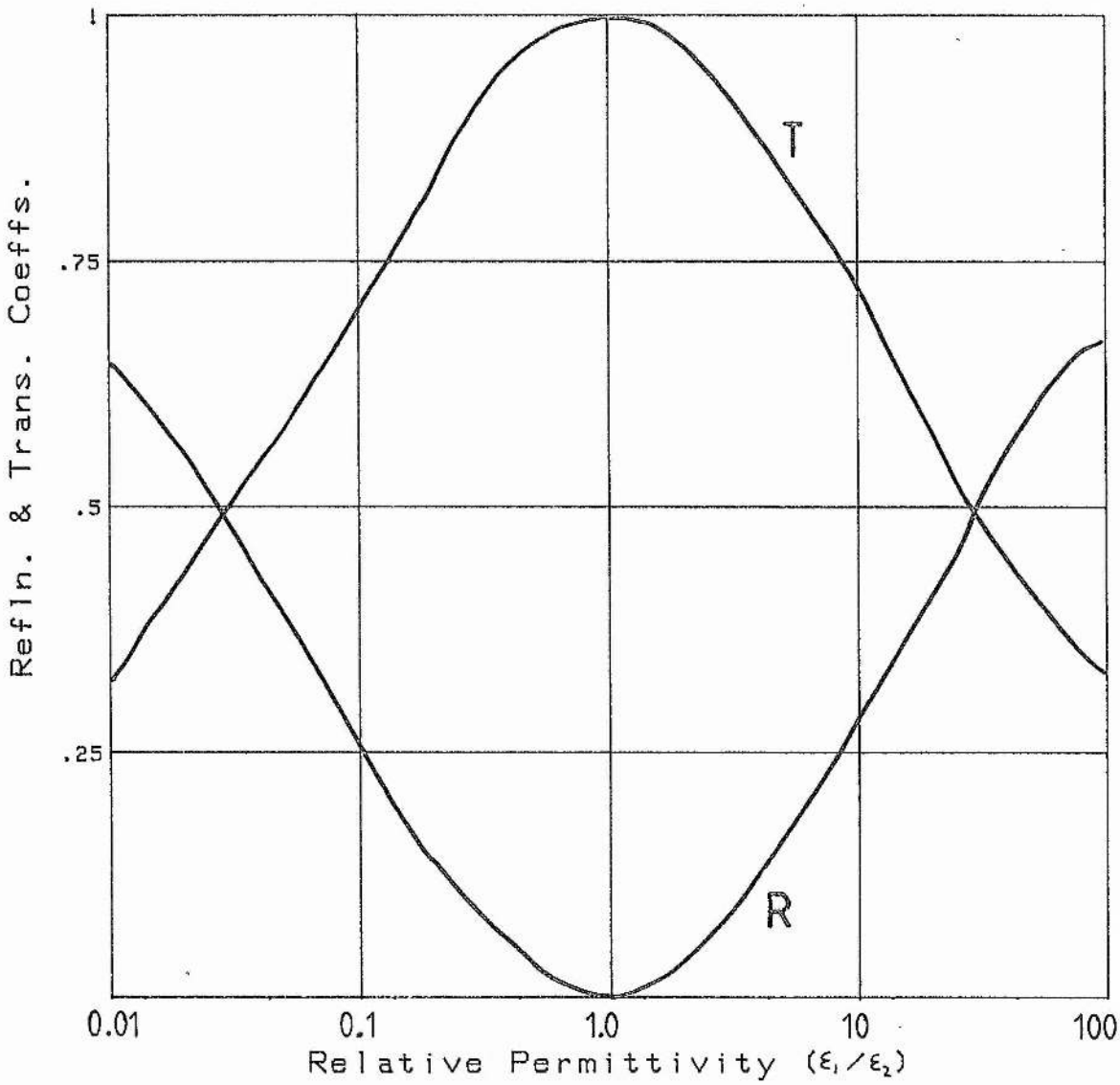


FIGURE 2.4

REFLECTION & TRANSMISSION COEFFICIENTS AT A DIELECTRIC BOUNDARY

$$R = \left[ \frac{\sqrt{\varepsilon_1}/\mathrm{Re}[\sqrt{\varepsilon_r}] - 1}{\sqrt{\varepsilon_1}/\mathrm{Re}[\sqrt{\varepsilon_r}] + 1} \right]^2$$

$$T = \frac{4\sqrt{\varepsilon_1}/\mathrm{Re}[\sqrt{\varepsilon_r}]}{[\sqrt{\varepsilon_1}/\mathrm{Re}[\sqrt{\varepsilon_r}] + 1]^2}, \qquad (2.38)$$

where $\varepsilon_1$ is the relative permittivity of the glass and $\varepsilon_r$ is the complex relative permittivity of the gas discharge. For $\varepsilon_1 = 2$, R and T have been plotted on figs 2.5 and 2.6 as a function of $\omega/\nu_m$ with $N_e$ as a parameter. It can be seen that, under certain conditions, the majority of the incident power is reflected. This effect is used in TR-cells for the protection of radar receivers [2]-[3], and will be considered in more detail later in this chapter. In order to see whether or not this effect prevents microwave power from penetrating the laser discharges reported in this thesis, $\omega/\nu_m$ and $N_e$ must be found. To do this, the kinetics of a microwave discharge will now be considered.

**Motion of electrons in a microwave field**

Almost all the excitation processes that occur in a gas discharge are due to electron-atom or electron-ion collisions. Noble gas ion lasers require large electron densities and a large, high-energy electron population. For these lasers the state of the electron population in the discharge is very important. This section describes how the electron population of a discharge is influenced by the properties of the exciting microwave field.

(i) An oscillating electric field

Under the influence of a DC electric field an electron is accelerated until it collides with a gas particle. After the collision, the electron is once again accelerated by the field. The kinetic energy of the electron increases and decreases depending upon the time between, and the nature of the collisions it undergoes. Since the direction of

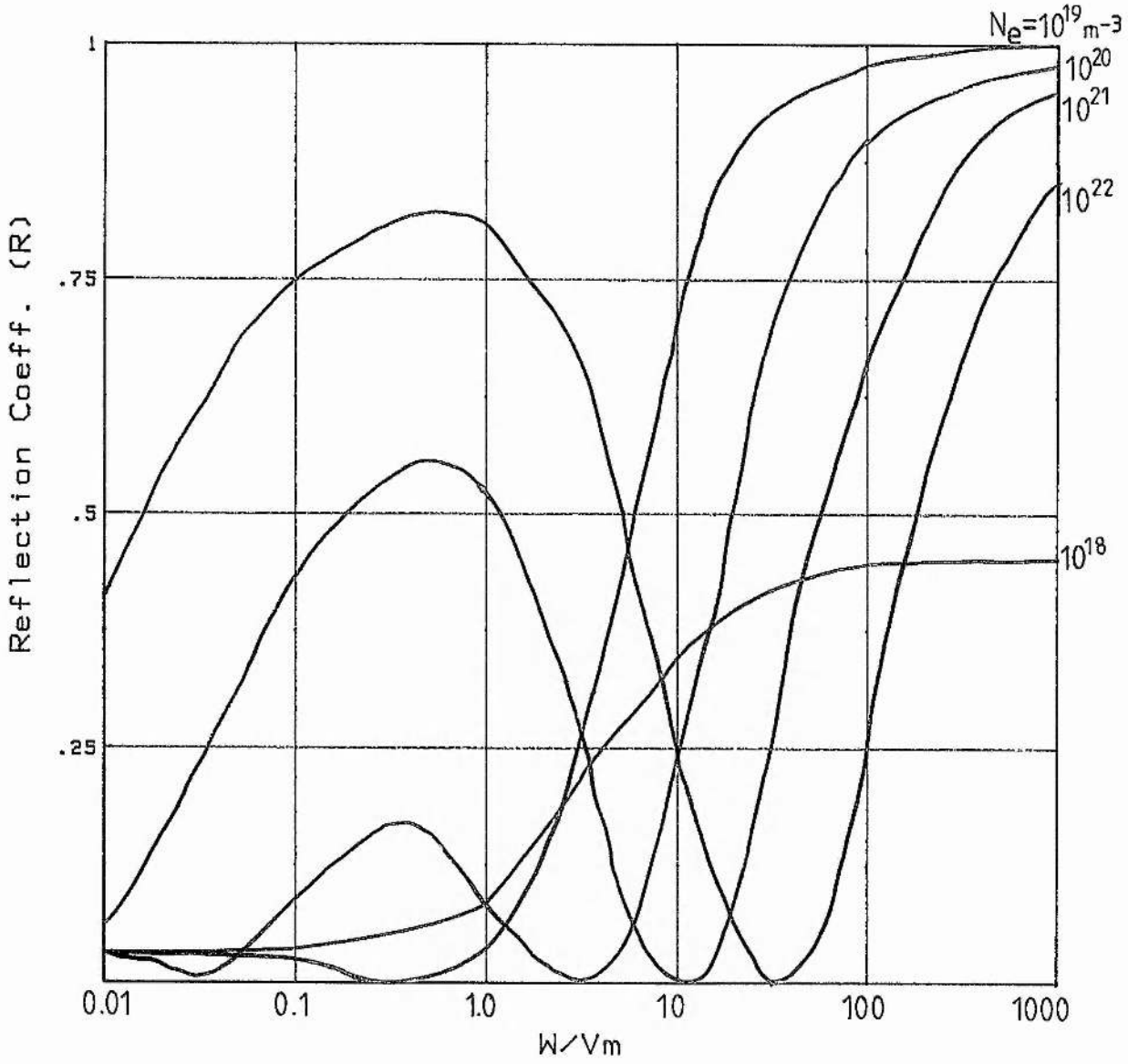


FIGURE 2.5

REFLECTION COEFFICIENT

AT A DIELECTRIC/IONISED-GAS BOUNDARY

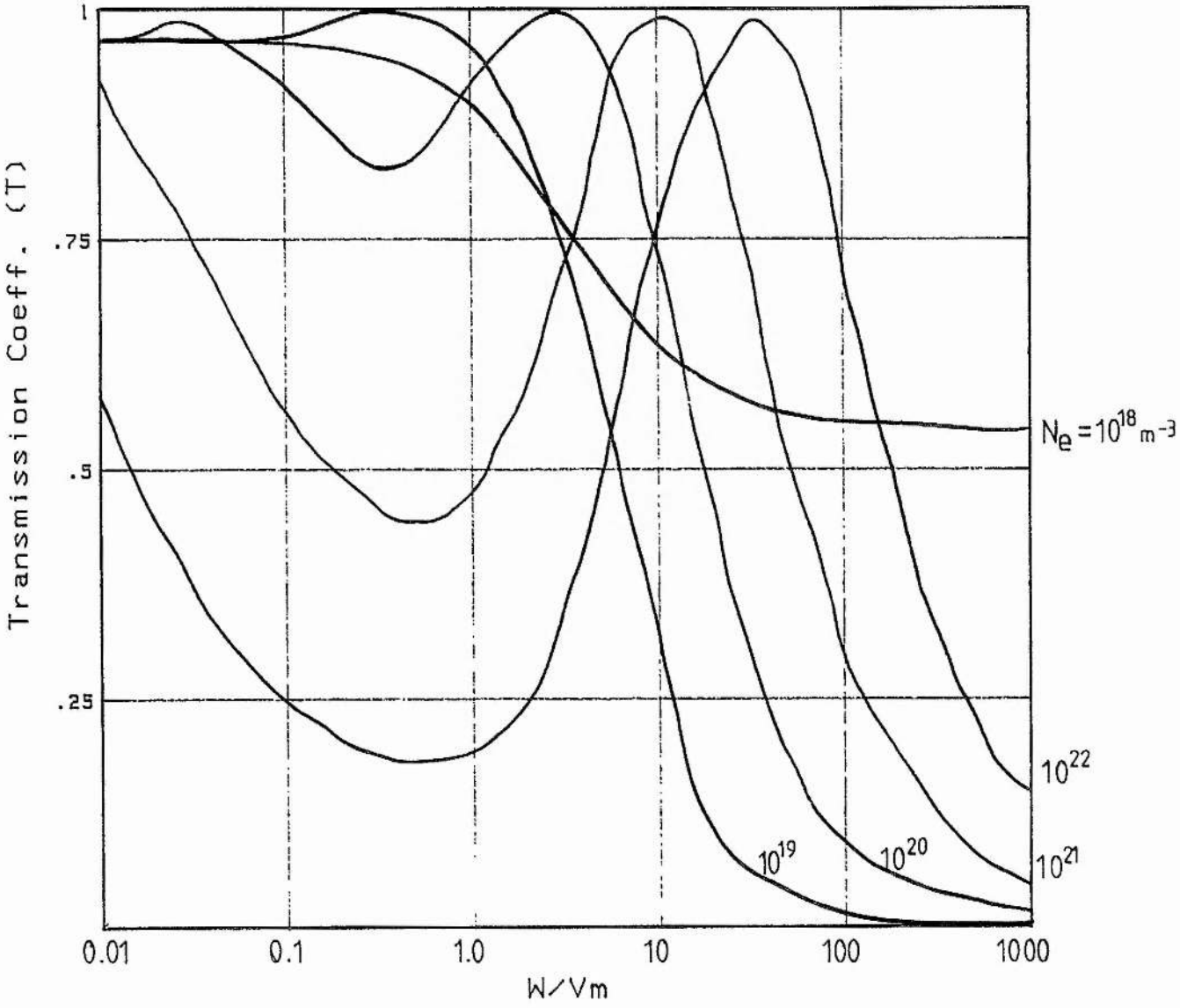


FIGURE 2.6

TRANSMISSION COEFFICIENT

AT A DIELECTRIC/IONISED-GAS BOUNDARY

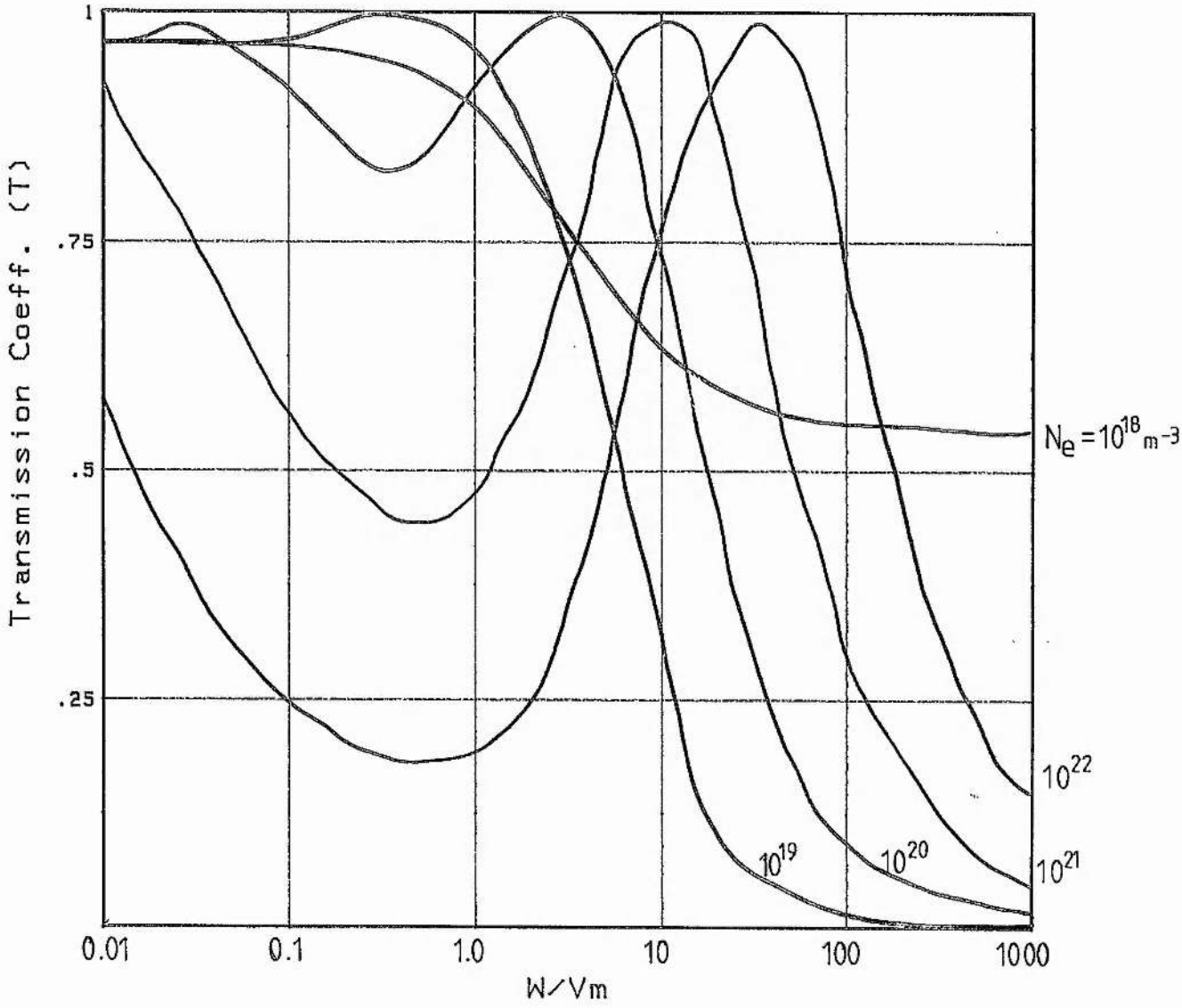


FIGURE 2.6

TRANSMISSION COEFFICIENT

AT A DIELECTRIC/IONISED-GAS BOUNDARY

the accelerating field never changes, the electron will eventually be pulled out of the discharge region. If the energy of the electron is high enough, a subsequent collision with the container walls or electrodes may lead to the production of secondary electrons. The properties of an RF discharge vary only slightly from those of a DC discharge because, on a microscopic scale, the field direction reversals occur much less frequently than collisions. Hence, the two can be treated in a similar fashion.

When microwave frequencies are used, the electric field oscillates so rapidly that the force on an electron changes direction before it can escape from the discharge region. In the absence of collisions, electrons simply oscillate in a microwave field, and the time averaged energy transfer from the field to the electrons is zero. Here, the electrons have their principal velocity components running parallel to the exciting electric field. They also have another component due to their thermal energy but this is relatively small. Collisions disturb the oscillatory motion of electrons allowing them to absorb power from the microwave field. As the kinetic energy of an electron builds up, the collisions it undergoes are all elastic, because at this stage, it has insufficient energy to excite an atom. In an elastic collision an electron loses only a small fraction of its kinetic energy given approximately by $(2m/M)(1-\cos\Psi)$. Here m and M are the electron and atomic masses, and $\Psi$ is the scattering angle through which the electron is deflected. The velocity component in the direction of the electric field is reduced after a collision. The electric field acts backwards and forwards in one direction only and has no effect on the other velocity components. In this way energy is transferred from the microwave field to the electrons in a gas discharge. The efficiency with

which energy is absorbed in this way is a function of the ratio of the frequency of the microwave field to the collision frequency for momentum transfer. Energy is also absorbed from the microwave field when an energetic electron collides with an atom resulting in its excitation or ionisation.

Electron losses in a microwave discharge are due mainly to electron diffusion to the walls of the container. Losses due to recombination and attachment are usually negligible. Since the production of secondary electrons due to wall collisions is unlikely, only electrons produced during collision processes within the discharge region need be considered.

The use of a transverse DC-excited discharge in an Argon ion laser would not be ideal due to the extensive wall interactions which would occur. However, at microwave frequencies transverse excitation is a feasible proposition. At the frequencies under study (3 - 17 GHz), the electrons in the gas discharge are accelerated in one direction for a period of time around $10^{-10}$ s until the field direction reverses. Neglecting collisions, the maximum distance travelled during this time, assuming a negligible initial velocity and a mean electric field strength of 100 kV/m (see chapters 3 and 4), is no more than 1.5 mm. When the effect of collisions is introduced, the mean distance travelled between field reversals becomes even smaller.

The mechanism of breakdown of a gas when microwave power is applied can be considered from a microscopic standpoint. There are always a small number of free electrons in a gas as a result of naturally occurring ionisation phenomena. On application of the field, electrons are accelerated until either a collision occurs or the field direction reverses. Initially, as the energy of an electron starts to

build up, the collisions it has will be elastic resulting in a change in its direction of motion, but little change in its kinetic energy. When the kinetic energy of the electron exceeds the lowest excitation energy of the atoms in a gas, there is a finite chance that an inelastic collision will occur resulting in the excitation of the atom at the expense of the electron's kinetic energy. When the accelerating electric field is high enough, some electrons will gain sufficient energy to ionise an atom on collision. If enough electrons are created in this way, so that the electron production rate exceeds the loss rate, breakdown will occur. The breakdown process for a DC discharge is essentially the same. Generally, microwave breakdown fields are lower because the electron loss processes have less influence at the stages leading up to breakdown.

When using pulsed microwave fields, breakdown can only occur if the electron density can rise to a sufficiently high level before the end of the pulse. There is a delay between the start of the microwave pulse and the discharge. This is due to the finite time taken for the electron population to build up. This delay can be reduced by increasing the pulse power to accelerate the excitation processes. Statistical variations in the delay time can be quite large, particularly in noble gases. The microwave sources reported in this thesis use 1 uS pulses with a repetition rate of 1000 pulses per second. These pulse lengths are long enough to ensure breakdown on every pulse. Moreover, the delay time and statistical variation are both small due to the residual ionisation from the preceding pulses. For a microwave discharge, the breakdown field is generally around 5 times more than the maintenance field. This presents no problems in the pulsed systems reported because of the high peak powers used. However, difficulty in

initiating a discharge was experienced for the CW systems studied.

Once a steady state discharge has been created, electrons in the discharge excite atomic and ionic energy states. Unless the excited states of the recipients are metastable, they will quickly decay with the emission of the characteristic radiation of their respective transitions. By observing the emission spectrum of the gas discharge, a certain amount of insight into the processes which occur can be obtained. Such a study has been carried out for the laser discharges used and the findings are reported in chapter 6.

(ii) Significance of the $\omega/\nu_m$ ratio

It has already been pointed out that collisional processes are necessary for electrons to absorb power from a microwave field. The important factor is the ratio between the frequency of the microwave field, and the collision frequency for momentum transfer. This ratio dictates the number of collisions occurring per oscillation of the electric field, and so, dictates the microwave power absorption efficiency of a discharge.

The Boltzmann equation and an electron conservation equation normally form the starting point for kinetic theory calculations used to find the properties of a gas discharge. The electron conservation equation balances the electron loss processes due to diffusion with the gain processes from ionisation. The Boltzmann equation describes the effect of applied forces and collisions upon the space and velocity distribution of particles in a gas. For noble gases, the solution of this equation is complicated by the fact that the total electron-atom collision frequency $\nu_c$ is a function of electron energy as shown on fig 2.7. Because of its complexity, solution of the Boltzmann equation will not be considered. However, many studies have been carried out [4]-

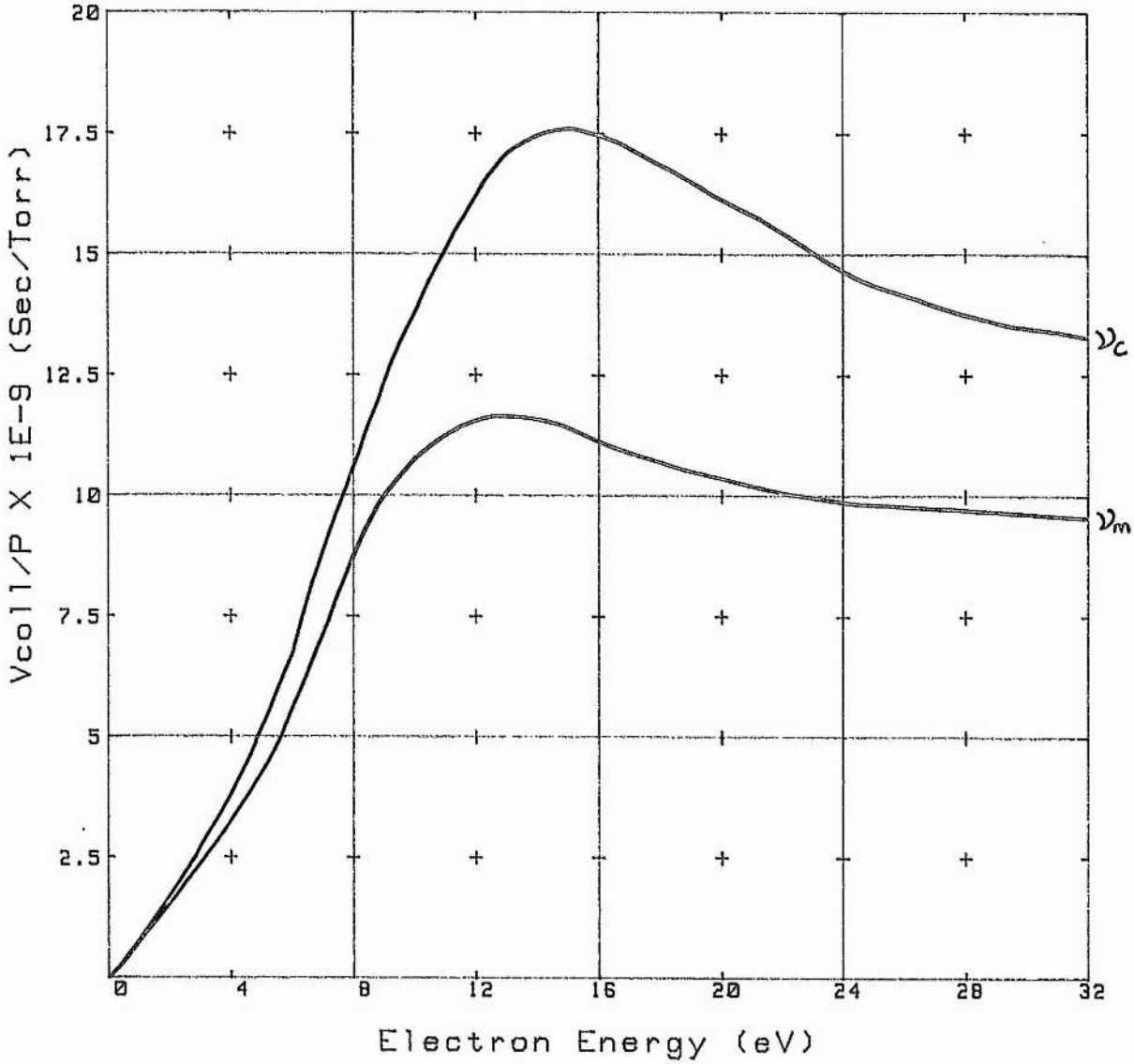


FIGURE 2.7
RATIO OF COLLISION FREQUENCY TO
ARGON PRESSURE (BASED ON [4]).

[11], and these use cross-section data like those given in [12]-[22].

The cross-section for momentum transfer $\nu_m$, is used when considering the energy gained by electrons from the exciting electric field. The mean kinetic energy absorbed by an electron per elastic collision is given by [6],

$$u_c = \frac{e}{2m} \frac{1}{\nu_m^2} \frac{E_p^2}{1 + (\omega/\nu_m)^2} \quad , \tag{2.39}$$

where e/m is the electron charge-to-mass ratio and $E_p$ is the peak value of the electric field. Like the total elastic collision frequency $\nu_c$, $\nu_m$ is a function of electron energy as shown on fig 2.7. The power transfer between the field and an electron, due to momentum transfer collisions, is given by $\nu_m(u)u_c(u)$, where u is the electron energy. By differentiating this it can be seen that the energy transfer is a maximum when $\omega/\nu_m$ equals 1. Also, it can be seen that when $\omega/\nu_m$ is much less than 1, we have

$$u_c \simeq (e/2m)(E_p/\nu_m)^2. \tag{2.40}$$

This is the same as for a DC discharge with $E = E_p/\sqrt{2}$. When $\omega/\nu_m$ is much greater than 1, we have

$$u_c \simeq (e/2m)(E_p/\omega)^2. \tag{2.42}$$

From fig 2.7 it can be seen that $\nu_m(u)$ is an increasing function of electron energy up to 12 eV, and that at energies above this, it is approximately constant. The high energy electrons have a higher collision frequency, and the power transfer is a maximum when $\omega/\nu_m$ equals 1. As $\omega$ is increased up to the maximum value of $\nu_m$ therefore, the high energy tail of the electron energy distribution is enhanced. Once $\omega$ is increased past the maximum value of $\nu_m$, the excitation efficiency decreases but is still highest for electrons in the high energy tail. The high energy tail is important in ion laser discharges and this will be discussed next.

(iii) The electron energy distribution function

The electron energy distribution function (EEDF) describes the kinetic energy distribution of electrons in a gas. Knowledge of this function is required in order to determine the $\omega/\nu_m$ ratio and the degree of excitation in the discharge.

The EEDF can be studied over the range where $\omega/\nu_m$ is much greater than 1 to where $\omega/\nu_m$ is much less than 1. In the case where $\omega/\nu_m$ is much less than 1, the distribution function reduces to that of a DC discharge which is a function only of E/N, where E is the mean applied electric field and N is the gas number density. When $\omega/\nu_m$ is much greater than 1, the distribution function becomes a function of $E/\omega$ only. At intermediate values, it depends upon both E/N and $E/\omega$. This variation in the EEDF is a result of its dependance upon the kinetic energy gain $u_c$ of electrons from a microwave field.

Noble gases have no low-energy excited states, and so the energy required by an electron for ionisation can be built up over several elastic collisions, without losses being incurred in atomic excitation. It is for this reason that ionisation and breakdown are relatively easily achieved despite the high ionisation energy of noble gases. In an exciting or ionising collision, an electron loses a significant proportion of its kinetic energy. This generally causes a steep fall in the distribution function in the vicinity of the lowest excitation threshold. The exact nature of this drop depends upon the conditions in the discharge. The bulk of the electrons in an ion laser discharge have insufficient energy to populate the upper laser levels. It is these electrons which principally dictate the mean electron energy (electron temperature), which for an ion laser discharge, is around 6 eV [23]-[26]. The high energy electrons in the tail of the EEDF are the most active

from an excitation point of view, as can be seen from figs 2.8 and 2.9. Here, the excitation and ionisation frequencies $h_x$ and $h_i$ are given by $P_x/P_c$ and $P_i/P_c$ respectively, where $P_x$, $P_i$ and $P_c$ are the probabilities of excitation, ionisation and collision. It is the high energy electrons which are required for the population of the upper laser levels.

The coupling structures reported in chapters 3 and 4 provide an electric field of up to 400 kV/m at the laser tubes. The principal laser under consideration, the Argon ion laser, operates at pressures P between 0.02 and 0.1 mB, with an operating gas temperature T of 1000-2000 K. The gas atom number density N is given by [4],

$$N(m^{-3}) = 7.24X10^{24}\ P(mB)/T(K). \qquad (2.42)$$

This gives a typical E/N ratio of up to $10^{-15}$ $Vm^2$. The microwave coupling structures operate at frequencies between 3 and 17 GHz making $E/\omega$ of up to $10^{-5}$ Vs/m. Because the E/N ratio is so high, direct (single-step) excitation of the upper laser levels is the process most likely to occur. The electron density is also likely to be high and in such a case the EEDF is Maxwellian in form. Under such circumstances the Boltzmann equation has been solved [11] and the EEDF has been calculated as shown on fig 2.10. The distribution functions have all been calculated for the same mean electron energy of 3.5 eV and $\omega/\nu_{ce}$ has been used as a parameter. Here, $\nu_{ce}$ is a constant equal to the collision frequency for momentum transfer for an electron with a kinetic energy of the same order as the mean electron energy. It can be seen from the figure, that as $\omega$ is increased, the high energy tail is enhanced. This is a result of the increasing energy transfer efficiency, as has already been explained.

It can be seen from fig 2.7 that the collision frequency for momentum transfer for Argon peaks at around 6 X $10^8$ collisions per

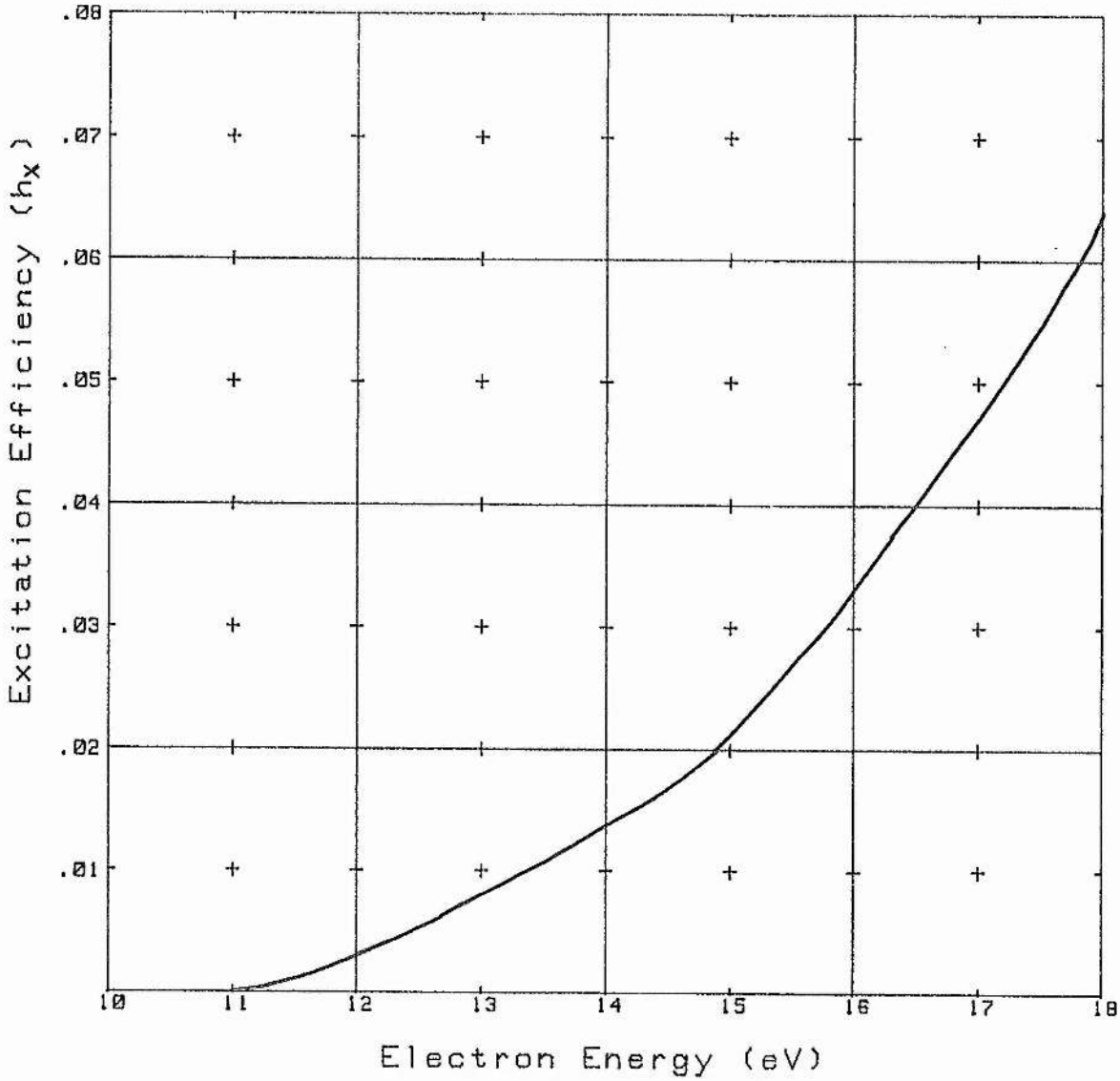


FIGURE 2.8

EFFICIENCY OF EXCITATION FOR ELECTRONS IN ARGON (FROM MacDONALD 1966 [4]).

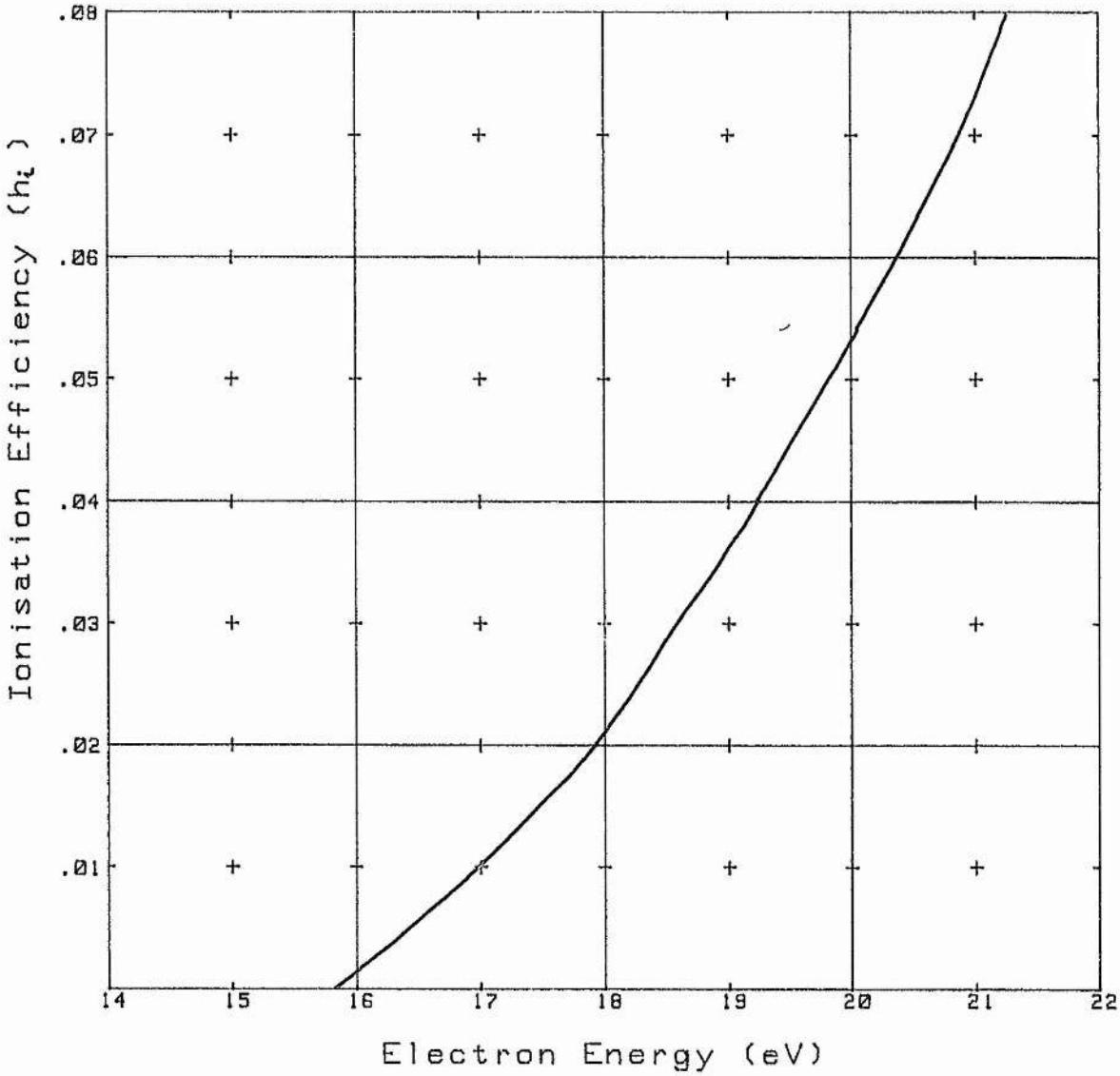


FIGURE 2.9

EFFICIENCY OF IONISATION FOR ELECTRONS IN ARGON (FROM MacDONALD 1966 [4]).

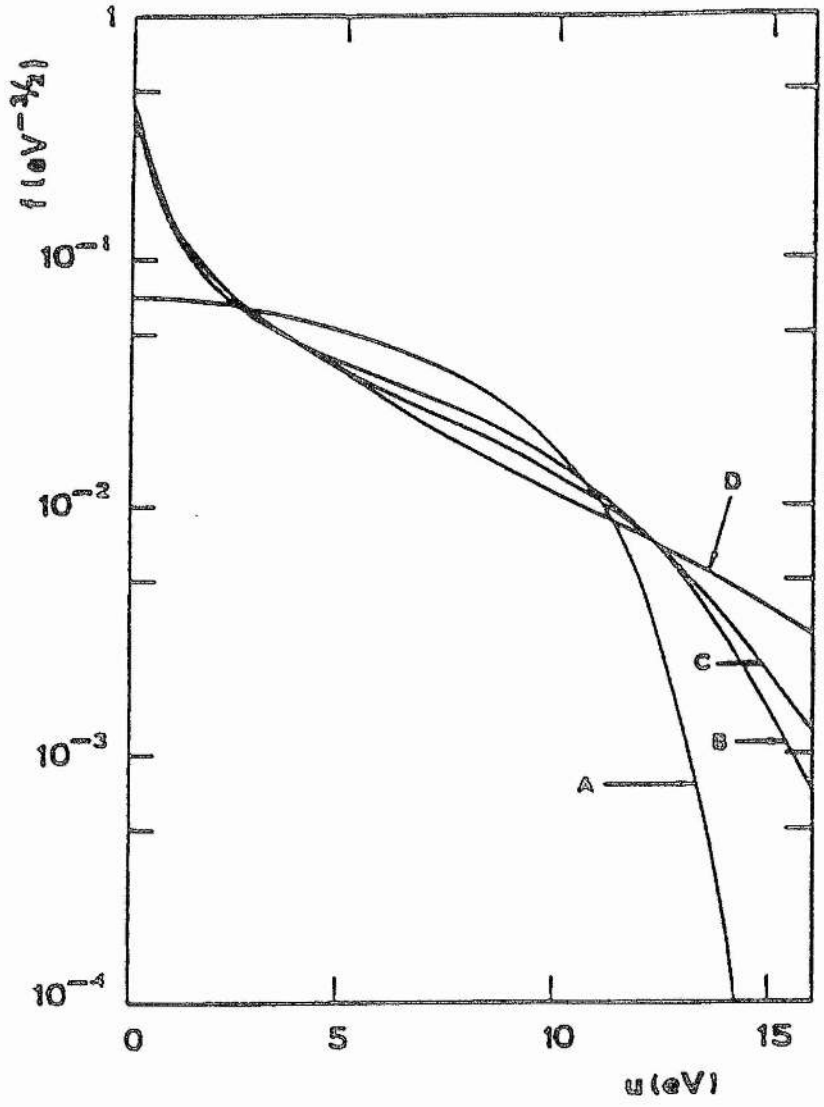


FIGURE 2.10 ELECTRON ENERGY DISTRIBUTION FUNCTIONS IN ARGON WITH THE SAME MEAN ENERGY OF 3.5eV FOR $\omega/\nu_{ce}$= 0(A); 0.5(B); 0.8(C); $\infty$(D). (From C.M.Ferreira et al. 1987 [11]).

second. Because the energy transfer efficiency is highest when $\omega$ equals $\nu_m$, this seems to place an upper limit on the optimum microwave frequency for an Argon ion laser fill, (where $\nu = \nu_{max}$), of approximately 100 MHz. At microwave frequencies above this, the power transfer from the microwave field to the gas by momentum transfer is less efficient. But, at the higher frequencies used here, the high energy electrons are still preferentially excited. Also, this does not include the effects of inelastic collisions resulting in direct excitation of the upper laser levels. These more energetic electrons have a much higher total collision frequency, as shown on fig 2.7, giving an optimum frequency, in this case, of around 1 GHz. Because of the wide range of electron energies involved, the excitation efficiency is only a weak function of microwave frequency, and to a first approximation, can be considered to be negligible.

An estimate of the mean electron energy in the laser discharges of 4 eV can be made by considering the laser performances and discharge spectra (see chapter 6). At this energy fig 2.7 gives a collision frequency for momentum transfer of around 2 X $10^8$ collisions per second for a gas pressure of 0.07 mB. For the microwave frequencies used, this gives an $\omega/\nu_m$ ratio of around 400. Noble gas ion lasers typically operate at electron densities of $10^{19}$-$10^{21}$ $m^{-3}$ [25]-[31]. Using an electron density of $10^{19}$ $m^{-3}$, figs 2.1 to 2.6 can then be used to evaluate the microwave propagation characteristics in the Argon ion and Helium-Krypton laser discharges. It can be seen that microwave power is not propagated, but is exponentially attenuated as it passes through a laser discharge. As a result of this attenuation, the laser discharges have a skin depth of around 1 mm. For the container geometries used this means that a uniform discharge should be obtained, and this is observed

in practice. Reflection of an externally applied microwave field at a glass/gas-discharge boundary can be significant. For the laser discharges used, at least 90% of the incident power is reflected. This could best be avoided by devising a discharge structure which introduces the microwave power directly into the gas discharge avoiding the discharge boundary.

**TR-cell operation using a laser gas fill**

In order to confirm that the majority of the incident microwave power is reflected before entering a laser gas discharge, the performance of a standard TR-cell containing a typical gas fill was examined. A TR-cell is used in radars to protect the sensitive receiver from the powerful magnetron pulses. When high microwave powers are incident upon the TR-cell, the gas inside the cell breaks down and a discharge is set up at the input end of the cell. The gas discharge reflects all the incident power thus protecting the radar receiver which is located behind it. When the magnetron pulse stops, the gas recombines and the low power reflected signals are then able to reach the receiver.

A TR-cell normally has a gas fill comprising Argon (~10 mB) and water vapour (~5 mB). The water vapour is a recovery agent used to extinguish the discharge as quickly as possible, once the microwave pulse has stopped, in order to admit reflected signals. A standard 3-element EEV BS928 TR-cell, containing a 0.07 mB Argon fill was studied. It can be seen that this gas fill differs considerably from that normally used in a TR-cell. The performance parameters of interest are the spike and total leakage. The spike leakage gives an indication of how quickly the gas in the cell breaks down and gives a measure of the energy transmitted before complete breakdown is established. The total leakage

includes spike and flat leakage and is a measure of the total power per pulse which is transmitted through the cell. The BS928 has a maximum spike leakage of 150 nJ/pulse and a total leakage of up to 420 mW/pulse.

The total leakage of the BS928 cell with the Argon ion laser fill is measured to be 82 W/pulse, for 10 kW, 1 uS input pulses at 1000 pulses per second. Although this is high compared with a proper TR-cell fill, this still represents only 0.82% transmission. Moreover, the spike leakage is observed to contribute a considerable fraction of the total leakage power. This is due to the poor breakdown of the gas fill because of the low pressure. Once the discharge becomes established, less than 0.2% of the incident power is transmitted. A Helium-Krypton ion laser fill is observed to give an even smaller total leakage. This is mainly because the spike leakage is less due to the higher gas pressures used.

The arrangement in a TR-cell is very similar to that studied earlier in the chapter where perpendicular incidence upon a plane boundary is considered. In the experimental case here, the incident wave is propagated along a waveguide, which, to a first approximation, can be considered to be a plane wave front. Both this experimental study, and the theoretical study reported earlier, confirm that only a small fraction of the incident microwave power can penetrate a dielectric/gas-discharge boundary.

## References

[1] P.Lorrain & D.Corson
"Electromagnetic Fields and Waves."
W.H.Freeman & Co., 1970.

[2] "Duplexer Preamble."
English Electric Valve Co. Ltd., Lincoln, 1971.

[3] A.D.MacDonald & S.J.Tetenbaum
"High frequency and microwave discharges."
In "Gaseous Electronics", Vol I.
Ed. M.N.Hirsh & H.J.Oskam
Academic Press, 1978.

[4] A.D.MacDonald
"Microwave Breakdown in Gases."
John Wiley & Sons Inc., 1966.

[5] C.M.Ferreira & J.Loureiro
"Electron energy distribution and excitation rates in high-frequency argon discharges."
J. Phys.D: Appl. Phys. 16 2471 1983.

[6] T.Holstein
"Energy distribution of electrons in high frequency gas discharges."
Phys. Rev. 70 367 1946.

[7] L.G.H.Huxley & R.W.Crompton
"Diffusion and drift of electrons in gases."
John Wiley & Sons, 1974.

[8] C.M.Ferreira & J.Loureiro
"Characteristics of high-frequency and direct-current argon discharges at low pressures: a comparative analysis."
J. Phys.D: Appl. Phys. 17 1175 1984.

[9] W.P.Allis & H.A.Haus
"Electron distributions in gas lasers."
J. Appl. Phys. 45 781 1974.

[10] L.R.Megill & J.H.Cahn
"The calculation of electron energy distribution functions in the ionosphere."
J. Geophys. Res. 69 5041 1964.

[11] C.M.Ferreira et al.
"The modelling of high-frequency discharges at low and intermediate pressure."
Invited Papers: 18th Int. Conf. on Phenomena in Ionised Gases, Swansea, Wales.
13-17 July 1987.

[12] C.M.Ferreira & J.Loureiro
"Electron transport parameters & excitation rates in argon."
J. Phys. D: Appl. Phys. 16 1611 1983.

[13] H.N.Kucukarpaci & J.Lucas
"Electron swarm parameters in argon & krypton."
J. Phys. D: Appl. Phys. 14 2001 1981.

[14] W.R.Bennett Jr. et al.
"Direct electron excitation cross sections pertinent to the Argon ion laser."
Phys. Rev. Letts. 17 987 1966.

[15] I.D.Latimer & R.M.St John
"Simultaneous excitation and ionisation of Argon by electrons to the upper laser states of $Ar^+$."
Phys. Rev. A 1 1612 1970.

[16] A.Chutjian & D.C.Cartwright
"Electron-impact excitation of electronic states in argon at incident energies between 16 and 100 eV."
Phys. Rev. A 23 2178 1981.

[17] H.Statz et al.
"Transition probabilities, lifetimes and related considerations in ionised Argon lasers."
J. Appl. Phys. 36 2278 1965.

[18] S.H.Koozekanani
"Excitation cross section of some of the states of NeII, ArII and KrII by electron collision."
IEEE J. of Qu. Elect. QE-2 770 1966.

[19] E.Eggarter
"Comprehensive optical and collision data for radiation action. II. Ar*."
J. Chem. Phys. 62 833 1975.

[20] A.Muller et al.
"An improved crossed-beams technique for the measurement of absolute cross sections for electron impact ionisation of ions and its application to $Ar^+$ ions."
J. Phys. B: At. Mol. Phys. 18 2993 1985.

[21] J.M.Hammer & C.P.Wen
"Measurements of electron impact excitation cross sections of laser states of Argon(II)."
J. Chem. Phys. 46 1225 1967.

[22] D.Rapp P.Englander-Golden
"Total cross sections for ionisation and attachment in gases by electron impact. I. positive ionisation."
J. Chem. Phys. 43 1464 1965.

[23] V.I.Donin
"Output power saturation with a discharge current in powerful continuous Argon lasers."
Sov. Phys. JETP 35 858 1972.

[24] J.Eichler & H.J.Eichler
"Calculation of the optimum electron energy in an $Ar^+$-laser plasma."
Appl. Phys. 9 53 1976.

[25] T.Fujimoto et al.
"Measurement of electron density and temperature in a pulsed Argon ion laser."
Mem. Sac. Eng. -Kyoto Univ. Jap. 32 236 1970.

[26] W.B.Bridges et al.
"Ion laser plasmas."
Proc. IEEE 59 724 1971.

[27] V.F.Kitaeva et al.
"Probe measurements of $Ar^+$-laser plasma parameters."
IEEE J. Qu. Elect. QE-10 803 1974.

[28] C.B.Zarowin
"Electron temperature and density in Argon ion laser discharges."
Appl. Phys. Letts. 15 36 1969.

[29] T.Goto & S.Hattori
"Electron density in high-current pulsed Argon discharges."
J. Appl. Phys. 42 3005 1971.

[30] I.Kato et al.

"Time variation of electron density in a pulsed He-$Kr^+$ ion laser."

J. Appl. Phys. 46 5051 1975.

[31] I.Kato et al.

"Time variation of internal plasma parameters in microwave-pulse-excited He-$Kr^+$ ion laser."

Jap. J. Appl. Phys. 16 597 1977.

# Chapter 3 Microwave Coupler Design Producing A Transverse Electric Field

This is the first of two chapters concerning the devices used to couple microwave power into the active medium of a laser. This chapter considers a microwave coupler design which is used to produce a transverse electric field across the laser tube, and the next chapter describes a helical structure which produces a longitudinal electric field. The coupling structure described efficiently and evenly distributes microwave power along the active length of the laser tube. The structure consists of three 3dB branch-guide couplers connected in series. An outline of the theory used to design a branch-guide coupler is given, followed by a description of the entire coupling structure.

## Transverse electric fields in rectangular waveguide

A waveguide is essentially a hollow metallic tube along which microwaves propagate by reflection at the walls. As waves pass along a waveguide, electric and magnetic fields are set up. The distribution of these fields can be derived from Maxwell's equations whilst using the boundary conditions defined by the waveguide [1],[2]. This analysis leads to a set of general equations defining the electric and magnetic fields at all points in the guide.

Waveguides with circular or rectangular cross-sections are most often used and rectangular waveguides will be concentrated upon here. Assuming propagation in the z-direction, there are three main types of wave that can propagate. These are the TE (transverse electric) wave where $E_z = 0$, the TM (transverse magnetic) wave where $H_z = 0$, and the

TEM wave where $E_z$ and $H_z$ = 0. The TE waves are generally the most important, and it is these which are used in almost all waveguide devices.

The electric and magnetic field distributions along the guide depend upon the modal content of the electromagnetic wave. The dimensions of the guide dictate the standing wave orders which can be set up in both the x and y-directions as shown on fig 3.1. Most microwave devices rely on knowledge of the fields in the guide, and so single mode propagation is desirable. As a result, the dimensions of a waveguide are usually chosen so that only the fundamental mode can propagate. All other higher order modes are attenuated by the guide.

The general field equations for a $TE_{mn}$ wave as derived from Maxwell's equations are given by [1]-[2],

$$\begin{aligned} E_x &= E_{ox} \cos(m\pi x/a) \sin(n\pi y/b) \exp[i(\omega t - \beta z)] \\ E_y &= E_{oy} \sin(m\pi x/a) \cos(n\pi y/b) \exp[i(\omega t - \beta z)] \\ E_z &= 0 \\ H_x &= H_{ox} \sin(m\pi x/a) \cos(n\pi y/b) \exp[i(\omega t - \beta z)] \\ H_y &= H_{oy} \cos(m\pi x/a) \sin(n\pi y/b) \exp[i(\omega t - \beta z)] \\ H_z &= H_{oz} \cos(m\pi x/a) \cos(n\pi y/b) \exp[i(\omega t - \beta z)]. \end{aligned} \tag{3.1}$$

Here, a and b are the broad and narrow dimensions of the waveguide, $E_{ox}$,..$H_{oz}$ are the peak values of the electric and magnetic fields, $E_x$,...$H_z$ are the fields at the point (x,y,z) in the guide, $\beta$ is the phase constant of the wave, and $\omega$ is the angular frequency of the field. The fundamental $TE_{01}$ mode, where m = 0 and n = 1, is then represented by,

$$\begin{aligned} E_x &= E_{ox} \sin(\pi x/a) \exp[i(\omega t - \beta z)] \\ H_y &= (\beta/\omega\mu_o) E_{ox} \sin(\pi x/a) \exp[i(\omega t - \beta z)] \\ H_z &= -j (\pi/\omega\mu_o a) E_{ox} \cos(\pi x/a) \exp[i(\omega t - \beta z)], \end{aligned} \tag{3.2}$$

where $\mu_o$ is the permeability of free space. When these equations are

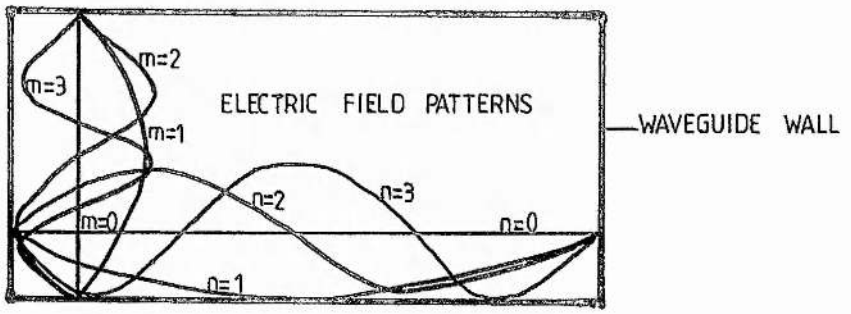


FIGURE 3.1 MODES IN A RECTANGULAR WAVEGUIDE.

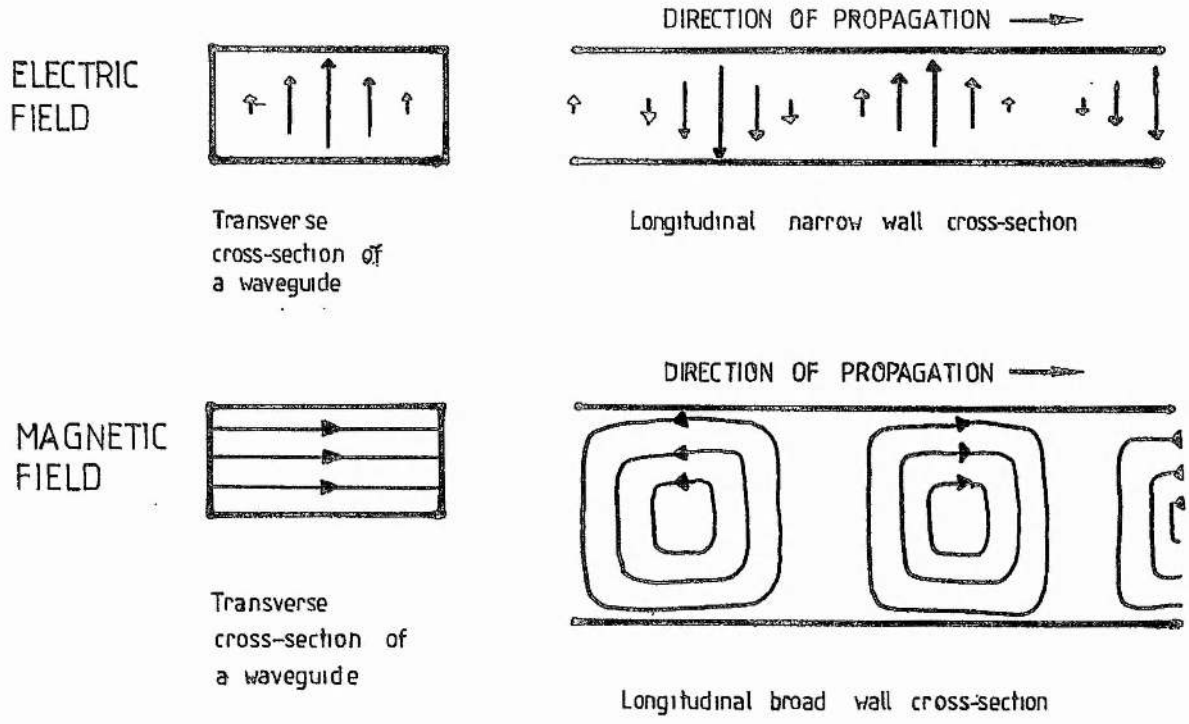


FIGURE 3.2 $TE_{01}$ ELECTRIC AND MAGNETIC FIELD DISTRIBUTIONS IN A WAVEGUIDE.

used to plot the electric and magnetic field strengths, the distribution on fig 3.2 is obtained. Here, the field patterns represent the instantaneous fields present in a waveguide as a $TE_{01}$ mode wave passes along it. The wave as it travels down the guide has a guide wavelength $\lambda_g$ given by [3],

$$\lambda_g = \frac{\lambda_o}{(1-(\lambda_o/2a)^2)} , \tag{3.3}$$

where $\lambda_o$ is the free space wavelength. The $TE_{01}$ mode is assumed to be the only mode present when the microwave coupler design is considered in the next section.

The power transmitted down a waveguide can be calculated by considering the time averaged Poynting vector given by eq 2.32. This equation is equivalent to the product of the average energy density and the phase velocity of the wave in the guide. Applying eqs 3.2 for a wave travelling down the z-axis,

$$\underline{S}_{av} = (\beta/2\omega\mu_o)\ E_{ox}^2 \sin^2(\pi x/a)\ \hat{\underline{z}}, \tag{3.4}$$

where $\hat{\underline{z}}$ is the unit vector in the z-direction. The total average transmitted power W, is obtained by integrating $\underline{S}_{av}$ over the cross-section of the guide to give,

$$W = \frac{ab}{4c\mu_o} E_{ox}^2 \left[ 1 - \left[\frac{\lambda_o}{2a}\right]^2 \right]^{0.5}. \tag{3.5}$$

The average transmitted power can be measured using standard microwave power measuring equipment and so the peak electric field can be determined. At 10 GHz using 100 kW fed into waveguide with dimensions 22.8 mm X 10.2 mm, a peak field of approximately 500 kV/m is achieved. Similar fields are obtained at 3 GHz and 17 GHz using the microwave power sources described in chapter 6. A field of this magnitude produces a voltage of around 3 kV across the outside diameter of the laser tubes used. This field is considerably higher than that normally used in noble

gas ion lasers.

Waveguide directional couplers

A waveguide directional coupler is a device which couples a specified amount of microwave power from a source waveguide into an auxiliary guide. This is done via a collection of slots, holes or branches located either on the broad or the narrow walls between the two waveguides. Such a coupler, as shown on fig 3.3, has directional properties. Ideally, if microwave power is passed along the source guide from port 1 to 2, the coupled power in the auxiliary guide will appear only at port 3; in this case, port 4 is essentially redundant. Similarly, if power is fed from port 2 to 1, the coupled power will appear only at port 4, with port 3 redundant. Since no directional coupler is perfect, a small amount of leakage occurs through the redundant auxiliary waveguide port. This leakage depends upon the directivity of the coupler. The higher the directivity, the smaller the leakage.

A directional coupler is generally specified by its operational bandwidth, VSWR, degree of coupling, and directivity; the latter two being specified by the equations,

$$C(db) = 10 \log_{10}\left(\frac{\text{Power through port 1}}{\text{Power coupled through port 3}}\right)$$
$$D(db) = 10 \log_{10}\left(\frac{\text{Power through port 3}}{\text{Power through port 4}}\right) . \qquad (3.6)$$

(i) The branch guide directional coupler

The branch guide coupler has a number of distinct advantages over other designs of coupler like the short slot, cross and multi-hole couplers. It can handle high microwave powers and is compact along a length of guide. It is best suited as a strong coupling device and is

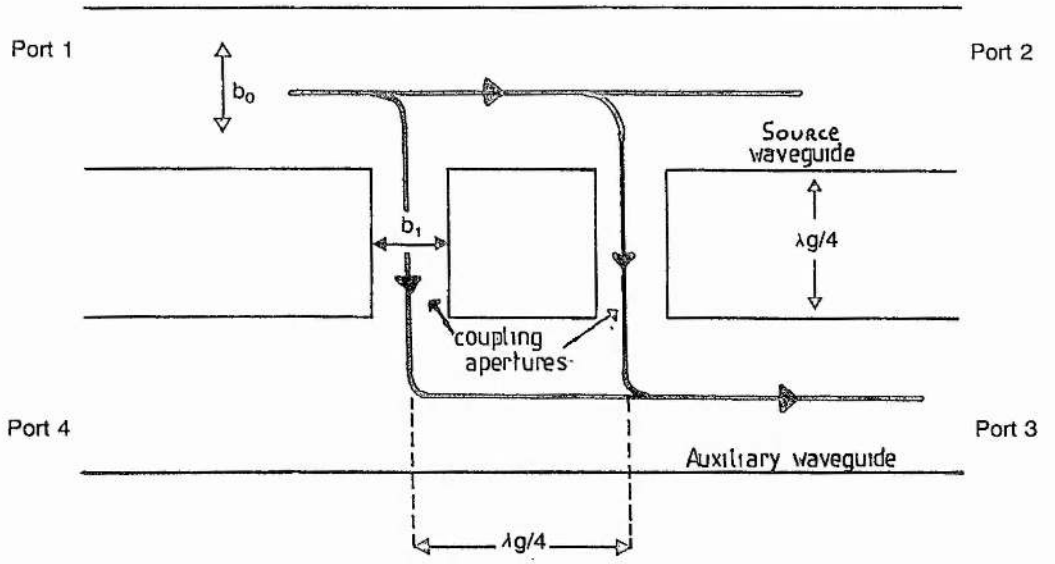


FIGURE 3.3 CROSS-SECTION OF A BRANCH GUIDE COUPLER.

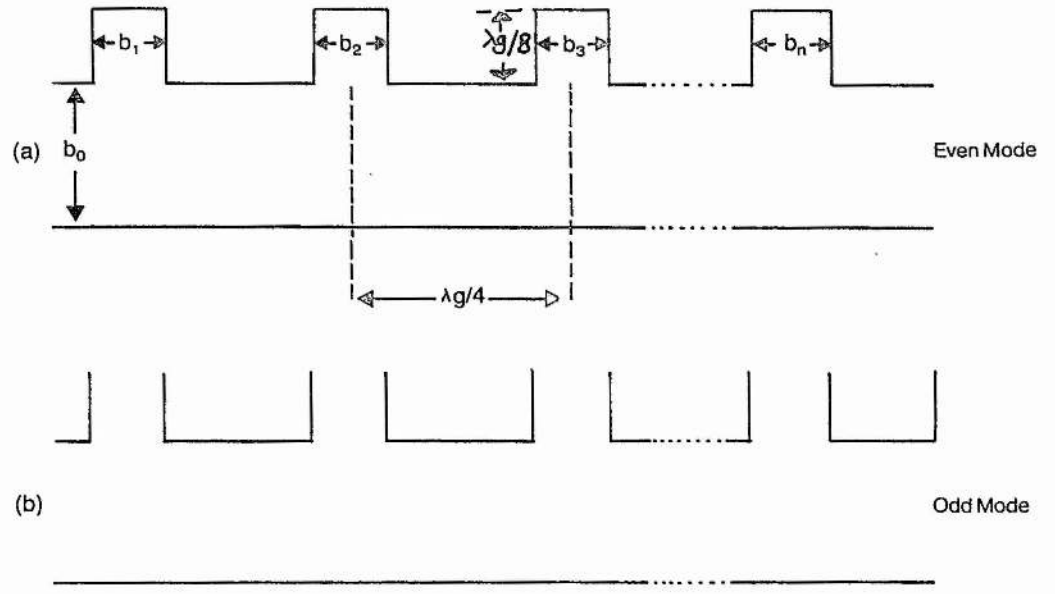


FIGURE 3.4 EVEN/ODD MODE ANALYSIS.

generally straightforward to construct. Also the VSWR, directivity and coupling over large bandwidths compare well with other coupler designs.

In the branch guide coupler, power is coupled between the main and auxiliary guides via a series of branch guides forming T-junctions at the broad walls. The dimensions of the branch guides dictate the degree of coupling between the two main guides. The most basic branch guide coupler, as shown on fig 3.3, consists of two equal branches of length $\lambda_g/4$, separated by $\lambda_g/4$. More advanced variations employ more branches and these can be studied by using ABCD-matrices to describe the coupler performance.

(ii) ABCD-matrix representation

Most microwave devices can be treated analytically by using a matrix representation. The ABCD-, S- and T-matrices are all used to describe n-port devices. Each type of matrix has an application to which it is best suited, although the S-matrix is the most general [4]. The ABCD-matrix has the advantage that, for a 2-port network, the resultant matrix of a series of single network elements can be determined by multiplying their individual ABCD-matrices as shown below,

$$\begin{pmatrix} A_{ntwk} & B_{ntwk} \\ C_{ntwk} & D_{ntwk} \end{pmatrix} = \begin{pmatrix} A_1 & B_1 \\ C_1 & D_1 \end{pmatrix} \begin{pmatrix} A_2 & B_2 \\ C_2 & D_2 \end{pmatrix} \cdots \begin{pmatrix} A_n & B_n \\ C_n & D_n \end{pmatrix} . \qquad (3.7)$$

This is of benefit in coupler analysis because the matrices of individual branches can firstly be found, and then all the component matrices can be combined. The reflection coefficient $\Gamma$ and the transmission coefficient T of a two port network are given by,

$$\Gamma = \frac{A + B - C - D}{A + B + C + D}$$

$$T = \frac{2}{A + B + C + D} , \qquad (3.8)$$

where A, B, C and D are the ABCD-matrix components of the network.

The directional couplers under study here are 4-port devices, but they can be reduced to 2-port networks by using an even/odd mode analysis. An even/odd mode analysis of the coupler on fig 3.3 can be carried out by considering the plane of symmetry between the main and auxiliary guides. The even mode is created by introducing two signals each of amplitude V/2 and equal phase into ports 1 and 4. A potential null then occurs along the plane of symmetry between the two guides. This is equivalent to inserting a short circuit which bisects the branches. The resulting 2-port network shown on fig 3.4a, represents the even mode. Similarly, the odd mode open circuit 2-port network is formed by applying signals which are 180° out of phase at ports 1 and 4. Assuming that all the ports of the coupler are properly matched, the sum or superposition of the even and odd modes gives an incident signal of unit amplitude in port 1 and zero in port 4. The amplitude out of port 2 is the sum of the transmitted amplitudes from the even and odd modes, and at port 3, the output is the difference in transmitted amplitudes. The emergent voltages can be written as,

$$\begin{aligned} V_1 &= (\Gamma_e + \Gamma_o)/2 \\ V2 &= (T_e + T_o)/2 \\ V_3 &= (T_e - T_o)/2 \\ V_4 &= (\Gamma_e - \Gamma_o)/2 , \end{aligned} \qquad (3.9)$$

where $\Gamma_e$ and $T_e$ are the reflection and transmission coefficients for the even mode and $\Gamma_o$ and $T_o$ are those of the odd mode. By using matrix equation 3.7, the ABCD-matrices of the even and odd modes can be

determined by cascading the matrices of their individual components. From fig 3.4, it can be seen that the components are $\lambda_g/8$ short circuit and open circuit stubs for the even and odd modes respectively. Also to be included here are the lengths of waveguide between the stubs.

Having found the ABCD-matrices of the even and odd modes, eqs 3.8 and 3.9 can be applied to eqs 3.6 to find the coupler directivity and coupling ratio. Most branch guide coupler design techniques [4]-[17], follow the basic route outlined so far, but from here the techniques diverge. A combination of these methods which incorporates both simplicity and accuracy is given here.

(iii) Component matrices

In order to calculate the ABCD-matrices of even and odd mode networks, the matrices of the individual network components must be found. For the even mode, the ABCD-matrix of the short circuit series stub of fig 3.4 is given by [5],[18],

$$\begin{pmatrix} 1 & -jZ_n \tan L/\lambda_{gc} \\ 0 & 1 \end{pmatrix}, \tag{3.10}$$

where $Z_n$ is the impedance of the branch guide, L/2 is the length of the stub, and $\lambda_{gc}$ is the guide wavelength at the centre frequency. The equivalent ABCD-matrix for the odd mode open circuit network is formed by substituting $-\cot \pi L/\lambda_{gc}$ for $\tan \pi L/\lambda_{gc}$ in matrix 3.10. Similarly, the ABCD-matrix of a length S of lossless transmission line is given by,

$$\cos \pi S/\lambda_{gc} \begin{pmatrix} 1 & jZ_o \tan \pi S/\lambda_{gc} \\ jY_o \tan \pi S/\lambda_{gc} & 1 \end{pmatrix}, \tag{3.11}$$

where $Z_o$ is the impedance of the main and auxiliary guides, and $Y_o$ is the admittance ($= 1/Z_o$). At the centre frequency where $L = S = \lambda_{gc}/4$, and normalising $Z_n$ with respect to $Z_o$, matrices 3.10 and 3.11 can be simplified to,

$$\begin{pmatrix} 1 & -jz_n \\ 0 & 1 \end{pmatrix} \qquad \text{and} \qquad 1/\sqrt{2}\begin{pmatrix} 1 & j \\ j & 1 \end{pmatrix}. \tag{3.12}$$

Here $z_n$ represents the normalised branch guide impedance ($= Z_n/Z_o$).

A signal entering the branch-guide coupler of fig 3.3 is split between ports 2 and 3. No power is observed at port 4 because the waves from the two branches travelling towards port 4 cancel due to the $\pi$ phase shift between them. Because of small differences in the signals from both branches, complete cancellation does not occur, and so a small amount of power reaches port 4. Additional thinner branches can be added to improve the cancellation and hence the directivity of the coupler. These also have the effect of improving the performance bandwidth. The size variation of the branches can be chosen in several ways. One way to do this is to consider the impedances of the branches. These are already incorporated in matrices 3.12 where $z_n$ is written as $z_1$, $z_2$,....$z_n$. A symmetrical impedance distribution is almost always used where the impedances of the branches are arranged as $z_1$, $z_2$, $z_3$,....$z_2$, $z_1$. In this way the performance of the coupler is independent of the input port used.

As an example, the ABCD-matrix of a 5-branch even mode network is found by cascading the individual component matrices 3.12. The resulting network matrix elements are given by,

$$\begin{aligned} A &= (z_1z_2 - 1)(z_2z_3 - 2) - 1 \\ B &= j(z_1z_2 - 1)(2z_1 + z_3 - z_1z_2z_3) \\ C &= jz_2(z_2z_3 - 2) \\ D &= (z_1z_2 - 1)(z_2z_3 - 2) - 1 \ . \end{aligned} \tag{3.13}$$

In order to completely evaluate these matrix elements, $z_1$, $z_2$ and $z_3$ must be known. The relative sizes of the impedances are found by choosing an impedance taper, and their absolute values are dictated by

the required coupling factor.

(iv) The Chebyshev impedance taper

Along the course of analysis being followed, four types of impedance taper can be considered. These are the Sine [7], Binomial [9], Chebyshev [10] and Butterworth [12] impedance tapers. The Chebyshev polynomial design generally gives the best performance over large bandwidths [11]. The recurrence relation for a Chebyshev polynomial of the first kind is given by,

$$T_{n+1}(x) = 2xT_n(x) - T_{n-1}(x) \ , \tag{3.14}$$

where we have $T_0(x) = 1$ and $T_1(x) = x$. Some of the polynomials in this series are shown on figs 3.5 and 3.6. It can be seen that over a specified bandwidth, the functions remain within tight limits and that, as the degree of the polynomial increases, the "tightness" of the distribution is improved. This is the main reason why the performance of a coupler improves as the number of elements is increased.

For many applications the directivity of a coupler is the most important parameter [19], and most designs try to maximise this over as large a bandwidth as possible. Considering the 5-branch coupler shown on fig 3.7, if power is fed into port 1, the scattered wave at port 4 which dictates the directivity is given by,

$$\begin{aligned} \underline{V_4} = {} & a_1\exp(-j\phi_c) + a_2\exp(-j3\phi_c) + a_3(-j5\phi_c) \\ & + a_1\exp(-j9\phi_c) + a_2\exp(-j7\phi_c), \end{aligned} \tag{3.15}$$

where $a_1$, $a_2$ and $a_3$ are voltage coupling coefficients and $\phi_c$ is the electrical length of a branch at $\lambda_{gc}$. The expression can be simplified to,

$$|\underline{V_4}| = |2a_1\cos4\phi_c + 2a_2\cos2\phi_c + a_3| . \tag{3.16}$$

The impedance taper is defined by setting $|\underline{V_4}|$ equal to a Chebyshev polynomial as follows,

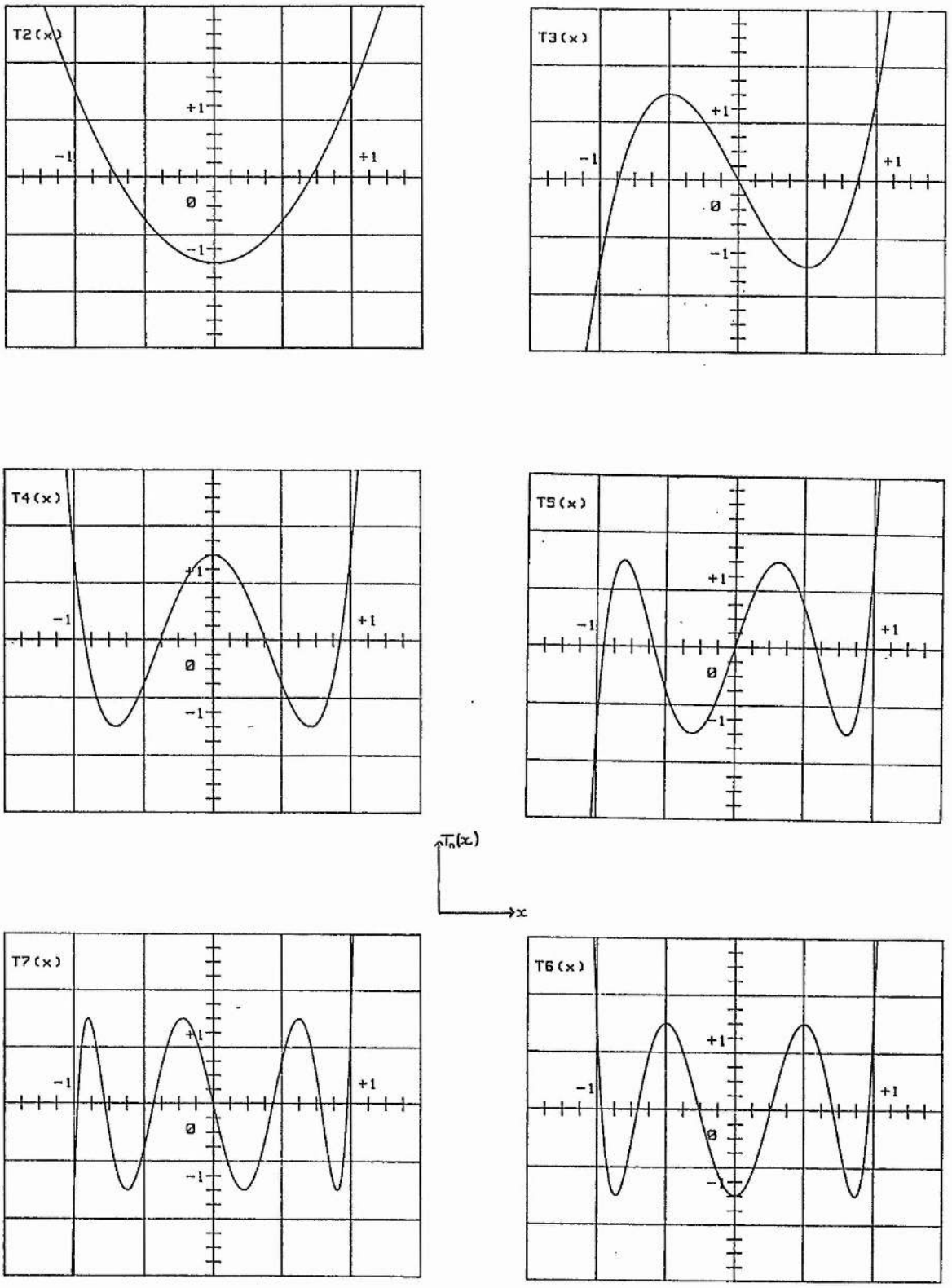


FIGURE 3.5
THE CHEBYSHEV POLYNOMIAL

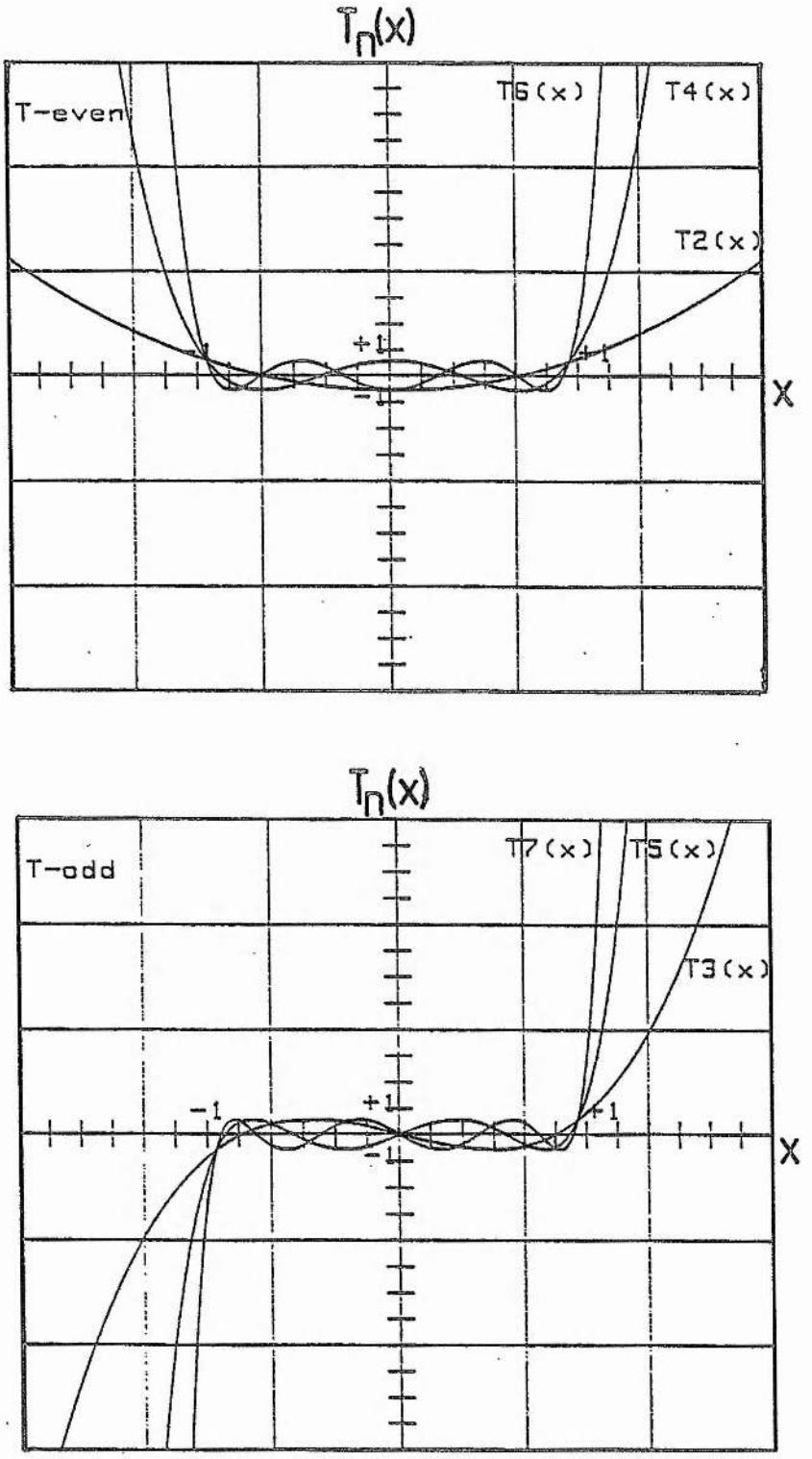


FIGURE 3.6

THE CHEBYSHEV POLYNOMIAL

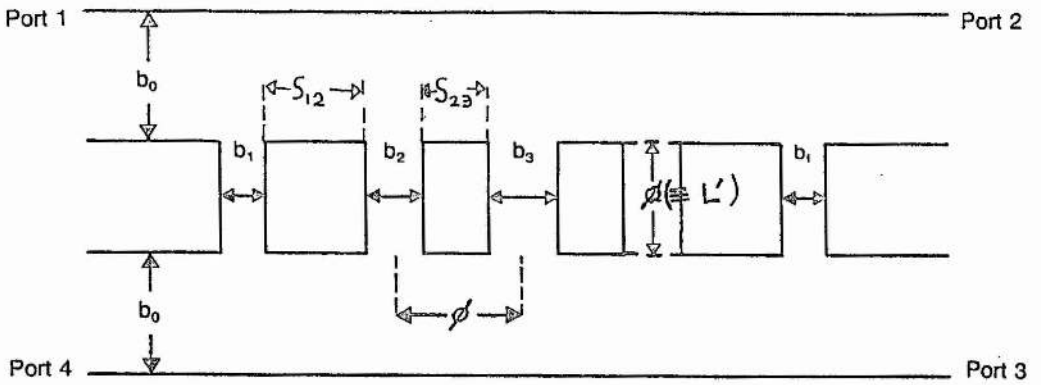


FIGURE 3.7 CROSS-SECTION OF A 5-ELEMENT BRANCH GUIDE COUPLER.

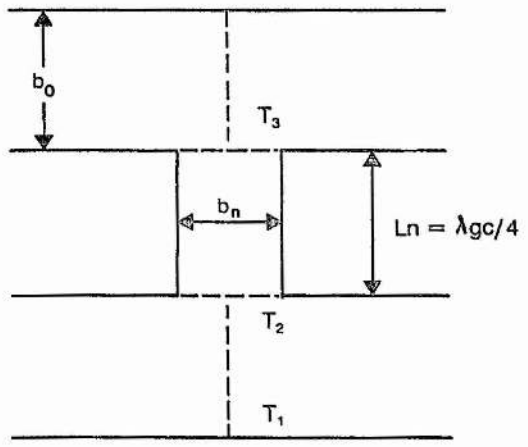


(a) A pure T-junction

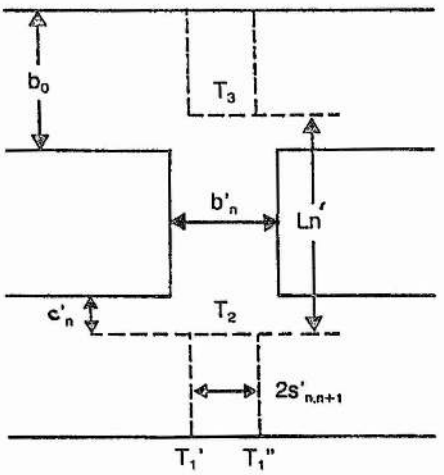


(b) A T-junction incorporating discontinuity effects.

FIGURE 3.8 USE OF REFERENCE PLANES TO COMPENSATE FOR T-JUNCTION DISCONTINUITY EFFECTS.

$$| 2a_1\cos 4\phi_c + 2a_2\cos 2\phi_c + a_3 | = \gamma T_4(tx). \qquad (3.17)$$

Here $T_4(x)$ is a Chebyshev polynomial in x of degree 4, where t is a scaling factor determining the operational bandwidth and $\gamma$ dictates the worst permitted directivity at the band edges. In this way the directivity of the coupler is given a Chebyshev form. Setting $x=\cos\phi_c$, the coefficients of $a_1$, $a_2$ and $a_3$ are equated and then normalised with respect to $a_1$. This gives,

$$\begin{aligned} a_1 &= 1 \\ a_2 &= 4(1 - 1/t^2) \qquad (3.18) \\ a_3 &= 2(3 - 4/t^2 + 1/t^4). \end{aligned}$$

In order to determine t, the directivity function at the band edges is considered. Here, we have $|\underline{V_4}| = \gamma$, and this implies that $tx = \pm 1$ giving,

$$t = \pm 1/\cos\phi. \qquad (3.19)$$

Using the equation

$$\phi = 2\pi L/\lambda_g, \qquad (3.20)$$

t can then be found for a specified bandwidth dictated by $\lambda_g$. The worst directivity in the band is given by,

$$D_{min} = 20 \log_{10}[T_4(t)]. \qquad (3.21)$$

Small values of t are indicative of large operational bandwidths but poor directivities. A compromise has to be reached between the two so that reasonable bandwidth and directional properties are achieved.

Having found t, eqs 3.18 can be applied to give the required relative voltage coupling coefficients, and hence the relative branch guide impedances. In order to determine the branch guide impedances explicitly, eqs 3.8 and 3.9 are combined to give,

$$| V_3/V_2 | = | (B+C)/(A+D) | . \qquad (3.22)$$

On specifying the required coupling ratio of the directional coupler,

this equation can be solved. In the case of the 5-branch coupler of fig 3.7, eqs 3.13 can be used to yield a polynomial in, for example $z_1$, and this can be iteratively solved using the Newton-Raphson method. Equations 3.18 can then be used to explicitly determine $z_2$ and $z_3$. Equations 3.13 and 3.18 can be modified for systems with a different number of branches and the rest of the procedure is the same.

Having calculated the impedance of each branch, its dimensions can be found using the equation,

$$z_n = b_n/b_o. \qquad (3.23)$$

However, the values thus obtained are only correct to a first approximation because matrices 3.10 and 3.11 were derived whilst neglecting discontinuity effects at the branch-guide junctions. These effects will now be considered.

(v) T-junction discontinuities

The earliest branch-guide coupler design models [5],[6] and [9], neglected discontinuity effects. A more complete analysis must include the perturbing effect of the T-junctions on the electric field distribution in the main and auxiliary waveguides. This results in the required modification of the previously calculated branch thicknesses, lengths and separations.

At a discontinuity, a large number of non-propagating modes are excited. The non-propagating nature of these modes restricts their influence to the immediate vicinity of the discontinuity and their effects can be regarded as localised. The electrical perturbations which a discontinuity causes, can be represented by equivalent circuits. Studies of such discontinuities have been carried out by [15] and [20]. Reference planes, as shown on fig 3.8, are used to represent the required alterations to the branch-guide dimensions and separations. By

considering these reference planes, and by comparing the transfer matrix of an ideal branch-guide with that of a real branch-guide, the modified coupler dimensions can be calculated [7], [15]. The correction equations are found to be,

$$b_n/b_o = n_o^2 \, (b_n'/b_o) \left[ 1 + \left( \frac{X_o/Z_o}{n_o^2 \, b_n'/b_o} \right)^2 \right]^{0.5} \tag{3.24}$$

$$L_n' = (\lambda_{gc}/2\pi) \cot^{-1} \left[ \frac{X_o/Z_o}{n_o^2 \, b_n'/b_o} \right] - 2c_n' \tag{3.25}$$

$$S'_{n,n+1} = \lambda_{gc}/4 + s_n' + s_{n+1}'. \tag{3.26}$$

Here, $b_n'$, $L_n'$ and $S_n'$ are the corrected branch-guide thicknesses, lengths and spacings of fig 3.7, and $X_o/Z_o$, $n_o^2$, $c_n'$ and $s_n'$ are complicated functions of $b_n'$ as shown on fig 3.9.

Bearing in mind that both $n_o^2$ and $X_o/Z_o$ are functions of $b_n'/b_o$, eq 3.24 is used to plot a graph of $b_n/b_o$ against $b_n'/b_o$ as shown on fig 3.10. Once the initial branch-guide thicknesses have been found from the procedure outlined earlier, fig 3.10 can be used to give the corrected values when the T-junction discontinuity effects are included. Once $b_n'$ is known, $L_n'$ and $S'_{n,n+1}$ can be found using eqs 3.25 and 3.26, and the graphs on fig 3.9.

It can be seen from fig 3.8 and eqs 3.24 to 3.26 that the branch dimensions have to be slightly decreased, and the branch spacings lengthened to allow for the T-junction discontinuity effects. In order to simplify construction, a power weighted mean branch length can be used, defined as

$$L' = \Sigma_n(z_n^2 \, L_n') \; / \; \Sigma_n(z_n^2) \; . \tag{3.27}$$

In the design procedure reported here, only the branch-guide impedances are tapered, whilst the main line impedances remain constant. A design procedure using a quarter-wave transformer prototype can be used [8], where the main line impedance is allowed to vary. However, that

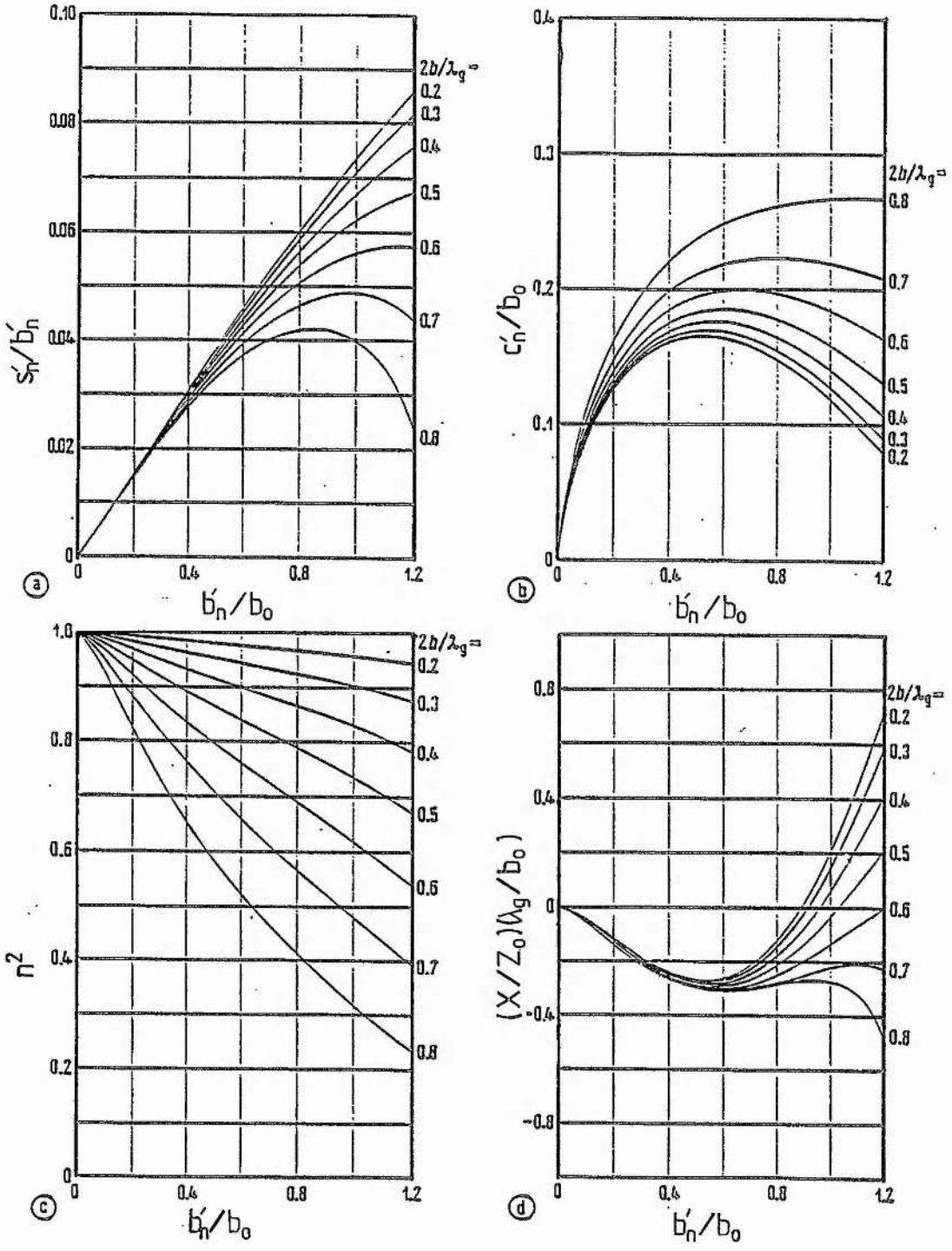


FIGURE 3.9

T-JUNCTION DISCONTINUITY CORRECTIONS

(From E.Kuhn 1974 [16])

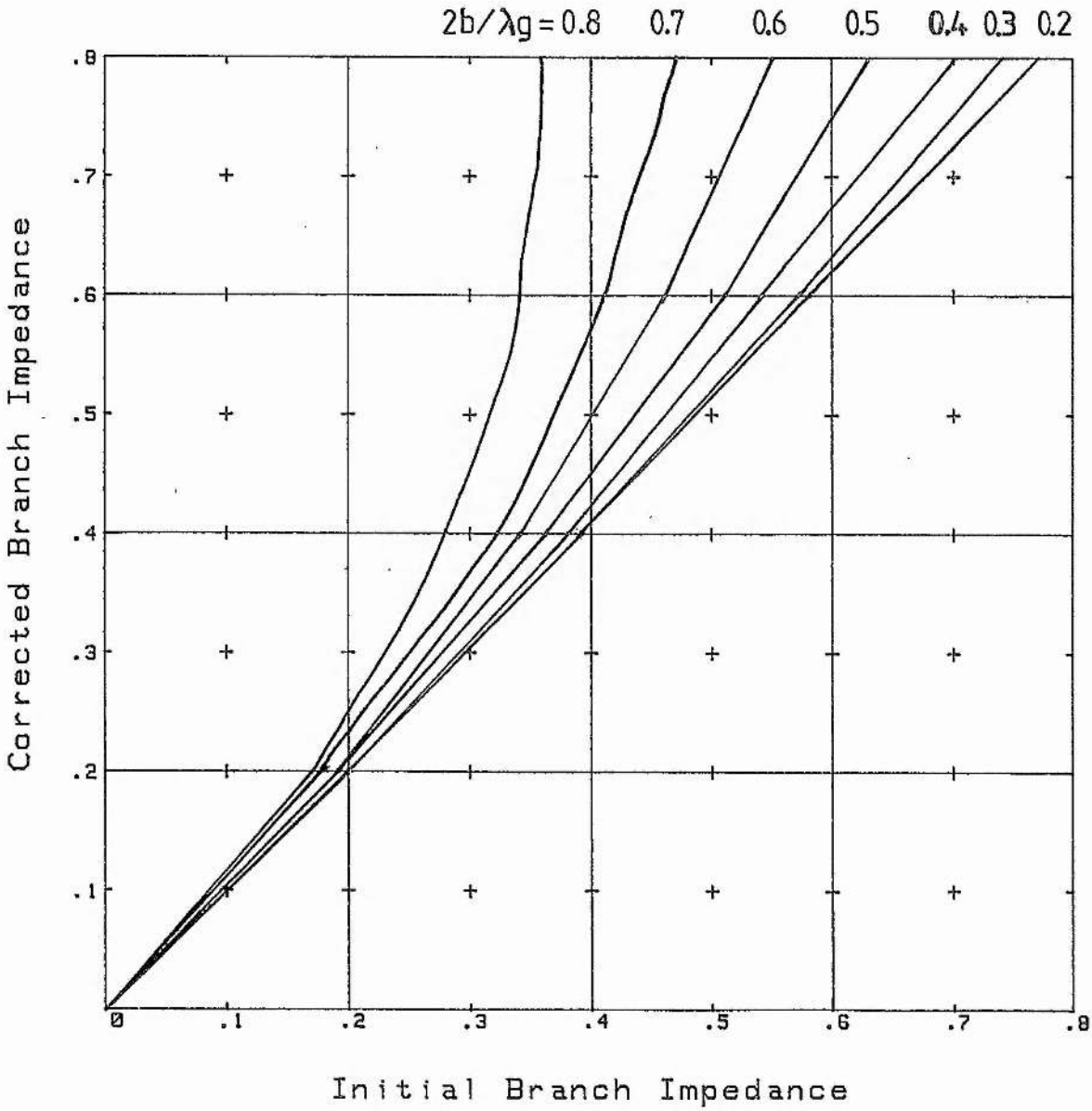


FIGURE 3.10
T-JUNCTION DISCONTINUITY CORRECTIONS
FOR BRANCH-GUIDE THICKNESS

technique is no better than the one reported here. Another design procedure based on Zolotarev functions can be used [14], but this technique is mathematically complicated, and does not give a major improvement in performance.

(vi) Frequency sensitivity of coupler performance

For certain applications it is desirable to know how a coupler behaves when operating over a specified bandwidth. So far, the design of a branch-guide coupler operating at the centre frequency $f_o = c/\lambda_{gc}$ has been considered. The lengths of the branches and their spacings were originally fixed at $\lambda_{gc}/4$ and the discontinuity analysis led to the optimisation of these dimensions for operation at $f_o$. Calculation of the branch thicknesses was based on the simplified component matrices 3.12 of the even and odd mode networks which apply at $f_o$. Some provision has been made for operation over a specified frequency band when choosing the impedance taper. Apart from this, no information about the frequency sensitivity of the coupler performance has been considered. In order to investigate this further it is necessary to return to matrices 3.10 and 3.11.

Previously, matrices 3.10 and 3.11 were simplified to matrices 3.12 which are valid only at $f_o$. The simplified component matrices were cascaded to give the ABCD-matrices of the even and odd mode networks. The impedance taper and specified coupling factor were then used to calculate the thicknesses of the branch-guides and the Chebyshev impedance taper was chosen to give the best possible directivity for a specified operational bandwidth. In order to calculate the behaviour of the coupler VSWR, coupling factor and directivity over that bandwidth, the ABCD-matrices 3.10 and 3.11 must be re-calculated in increments of wavelength within the band. The T-junction discontinuity corrections

also depend on $\lambda_g$ [16], and the effect of this must also be included for a complete analysis.

(vii) Directional coupler dimensions

Branch-guide couplers with five elements are the most commonly used because they have a good performance-to-size ratio. On this basis 5-element couplers were chosen for use in the laser coupling structures. As has already been stated, there are a number of techniques which can be used to calculate the dimensions of a branch-guide coupler. An outline has been given of one particular route which some of the more commonly used design techniques follow. The dimensions of a 5-element 3dB branch-guide coupler using a route similar to the one reported here are tabulated on fig 3.11 [11]. These dimensions were incorporated in the laser coupling structures to be described next.

**The Laser coupling structure**

The branch-guide coupler design as described above was used in the laser coupling structures. Although fringe effects at the T-junctions in these couplers distort the electric field pattern, the field can be considered, to a first approximation, to be transverse within the coupler region.

The coupler designs of figs 3.7 and 3.11 are in fact, 3dB-hybrid couplers. When microwave power is fed into port 1 of a such a coupler, the power emerges split equally between ports 2 and 3. Because of the quarter wavelength spacing between the main and auxiliary guides, the signal emerging out of port 3 is $\pi/2$ out of phase with that from port 2. Now, if two such 3db-hybrid couplers are connected in series, this phase property results in the combination acting as a 0-db coupler, (that is, all the power emerges from port 3). This is shown schematically on fig

| Operating Frequency | $b_1$ | $b_2$ | $b_3$ | L' | $S_{12}$ | $S_{23}$ |
|---|---|---|---|---|---|---|
| 16 GHz | 1.4 | 3.6 | 4.4 | 5.3 | 5.1 | 3.7 |
| 10 GHz | 1.8 | 4.6 | 5.7 | 6.9 | 6.6 | 4.8 |
| 3 GHz | 5.8 | 15.4 | 19.0 | 22.8 | 22.0 | 16.1 |

Dimensions in mm.

FIGURE 3.11 DIMENSIONS USED FOR THE 3dB BRANCH-GUIDE COUPLERS OF THE LASER COUPLING STRUCTURE (See Figs. 3.7 & 3.8 ). (From R.Levy 1966 [11]).

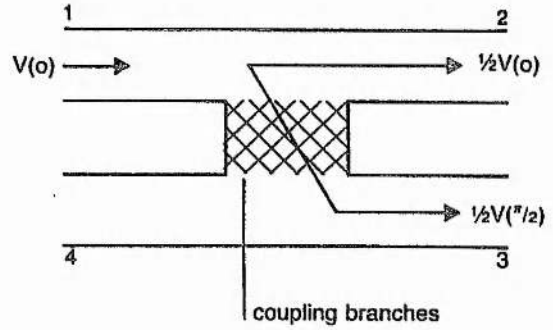


(a) A single 3dB hybrid coupler

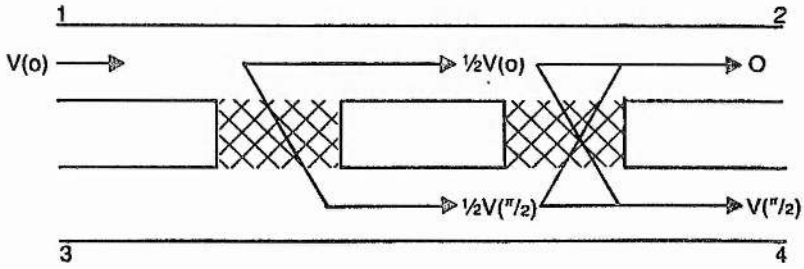


(b) Two 3dB hybrid couplers in series.

FIGURE 3.12 SCHEMATIC OF THE 3dB-HYBRID COUPLER.

3.12. No power emerges from port 2 of the combination because of the phase change which occurs when a signal crosses into the auxiliary guide via the first coupler, and then back again into the main guide via the second coupler. This property has been used in the design of the laser coupling structure.

The laser coupling structure reported here makes use of three 3db-hybrid couplers connected in series, separated by a distance approximately equal to the guide wavelength $\lambda_g$ as given by eq 3.3. The laser tube is placed along the centre of the auxiliary guide and variable short circuits are placed at the three output ports. The short circuits in the auxiliary guide have holes in their centres to accommodate the laser tube. Figure 3.13 illustrates the fields which are set up in the absence of the laser tube. It can be seen that power will be distributed fairly evenly along the length of the auxiliary guide whilst avoiding most of the nulls which are set up by standing waves. Furthermore, power is cycled twice through the coupler before leaving at port 1. This analysis assumes perfect 3db-hybrid couplers, the correct positioning of the short circuits and a lossless system. However, it neglects the presence of the laser tube.

The laser tube and associated gas discharge introduce a significant perturbation to the electric field distribution in the coupler. Tuning facilities at the three variable short circuits enable the device to be tuned for maximum efficiency. Using this technique it is possible to tune the device so that the reflected power is 20db down on the input. However, this does not necessarily indicate that the remainder of the power is absorbed by the gas discharge. If the discharge acts as an efficient microwave load, this will be the case, otherwise, the power will oscillate in the device and will gradually be

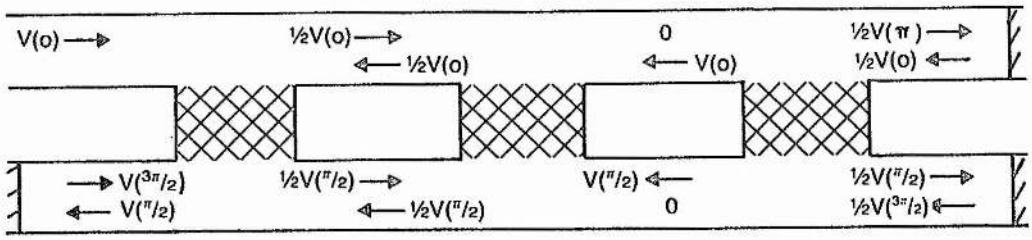


FIGURE 3.13 SCHEMATIC OF THE LASER COUPLING STRUCTURE.

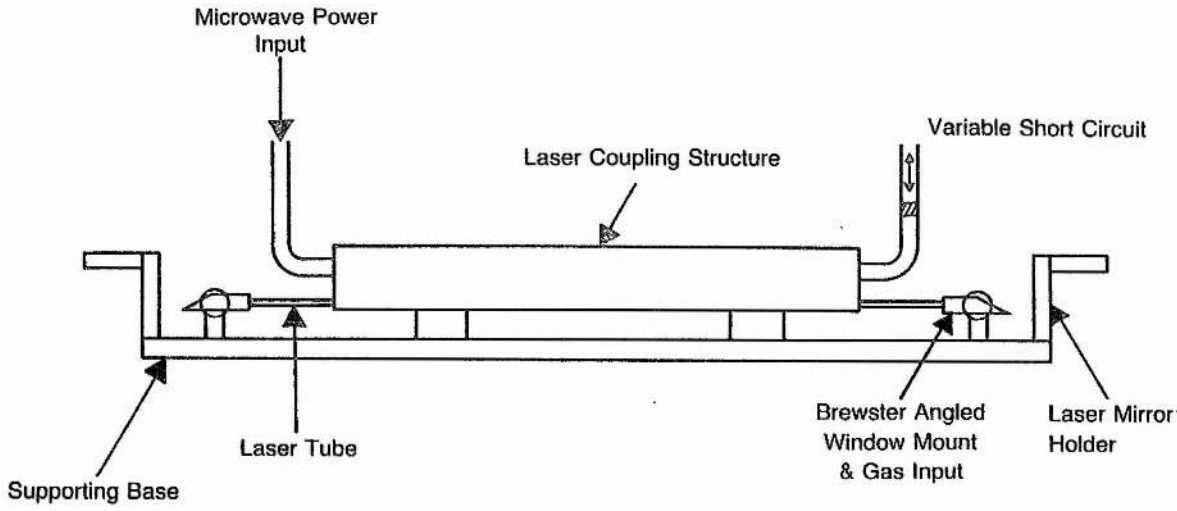


FIGURE 3.14 SCHEMATIC OF THE COMPLETE LASER STRUCTURE.

absorbed by the walls. As has been explained in chapter 2, the gas discharge used here does not act as a good load and the majority of the incident power is dissipated in the coupling structure itself.

In order to measure the uniformity of the electric field being applied to the laser tube, a small probe was inserted into holes placed in the broad wall of the auxiliary guide. The probe consisted of a small length of wire which, when inserted into the guide, ran parallel to the electric field. The probe wire was connected to a crystal detector which converts microwave frequencies into a DC voltage which is proportional to the electric field strength. A fairly uniform electric field distribution was recorded along the length of the laser tube. This is desirable for even excitation of the laser medium.

Coupling structures were constructed for operation at 10 GHz and 17 GHz based on the dimensions tabulated on fig 3.11. The couplers were constructed out of aluminium alloy HE30 and then coated with a Chromate passivation layer to protect the aluminium from the corrosive effects of high microwave powers. A computer numerically controlled machine (CNC) was used to mill out the structures in two halves where a plane bisects the broad walls of the main and auxiliary guides. These two halves were then joined together by screws and mounted onto a solid base plate which was also used to support the laser mirror holders and the Brewster angled window holders and gas ports (see chapter 6). A schematic of the complete laser structure is shown on fig 3.14, and photographs of the 10 GHz and 17 GHz devices are given on figs 3.15 and 3.16. A branch-guide coupler for operation at 3 GHz was not used due to its large size and a smaller commercial multi-hole 3dB-coupler was used instead. This coupler also produces a transverse electric field. In this case, a small platform was attached at each end of the coupler to support the optics

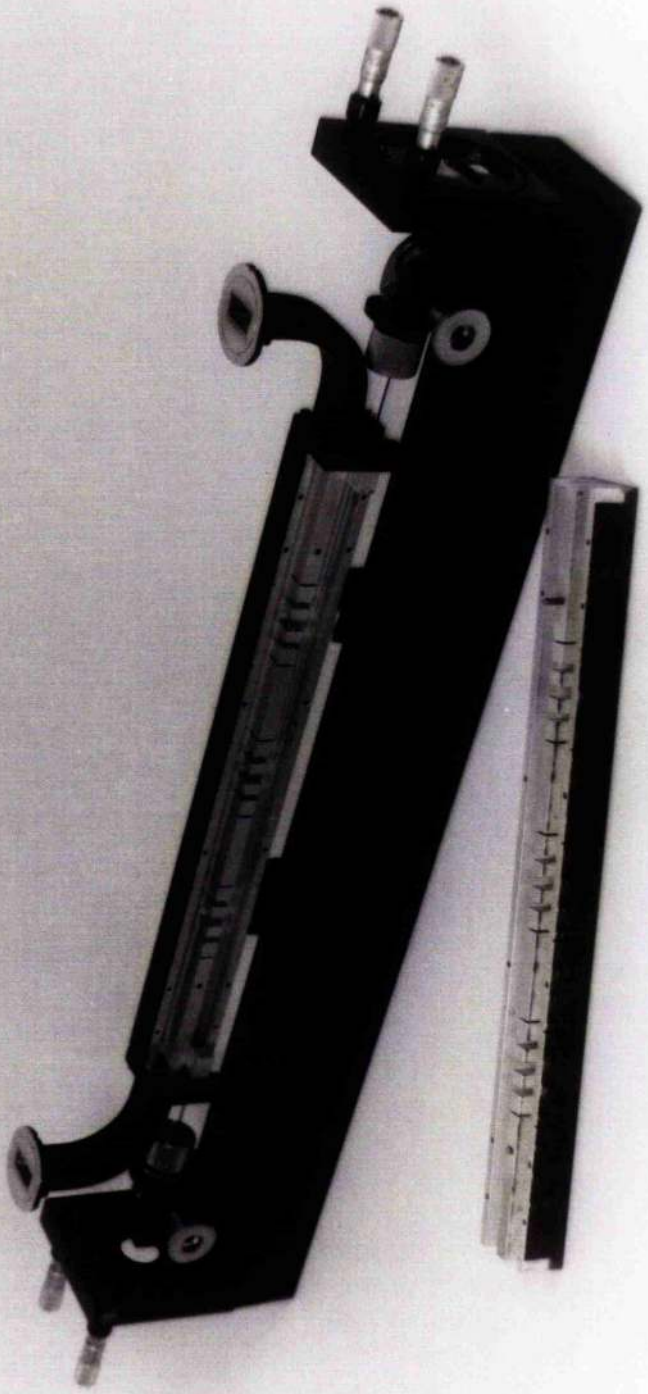

FIGURE 3.15 THE COMPLETE WAVEGUIDE 10 GHz LASER COUPLING STRUCTURE.

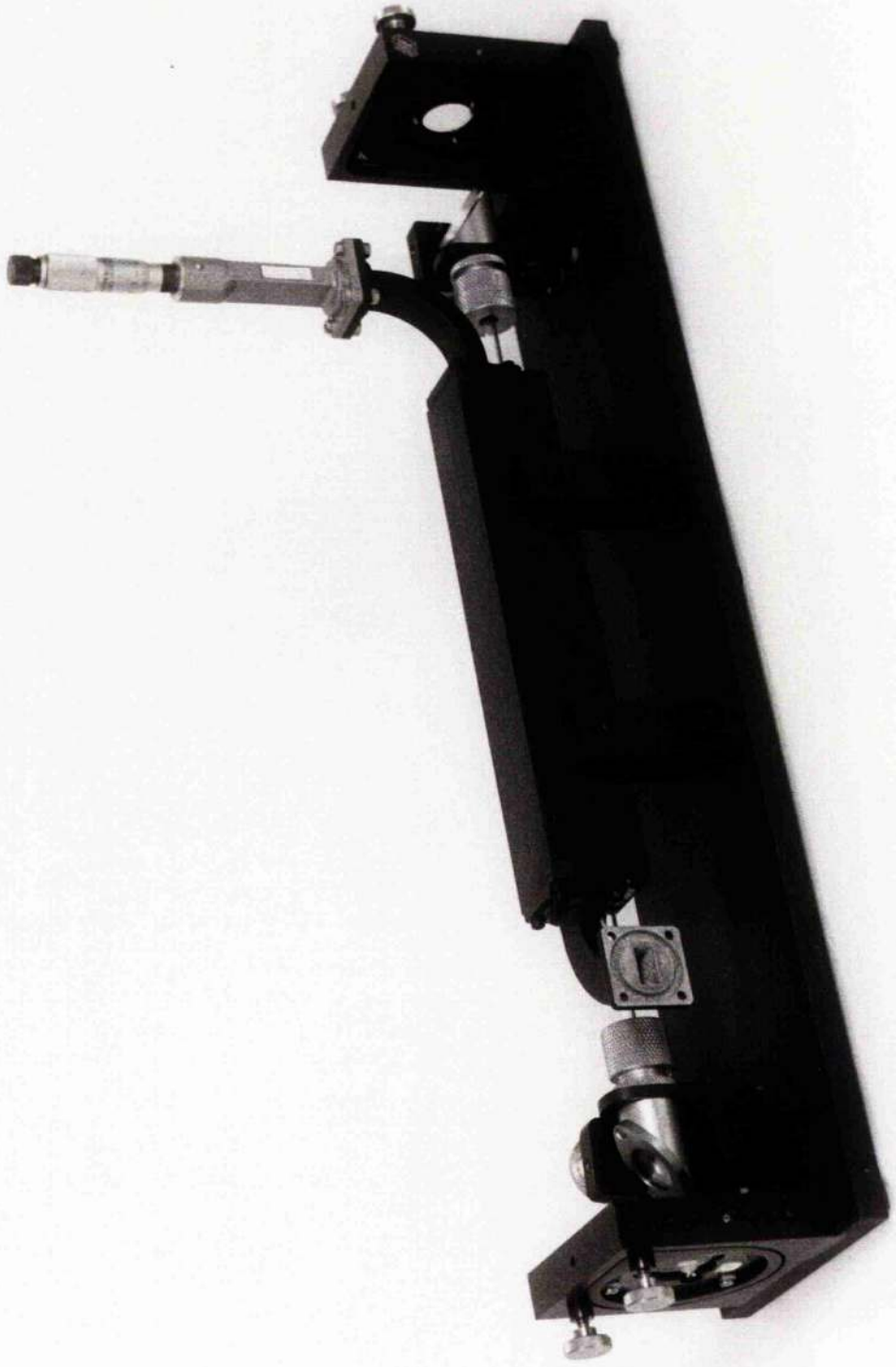

FIGURE 3.16 THE COMPLETE WAVEGUIDE 17 GHz LASER COUPLING STRUCTURE.

and gas ports.

References

[1] P.Lorrain & D.R.Corson
"Electromagnetic Fields and Waves."
W.H.Freeman & Co., 1970.

[2] H.R.L.Lamont
"Waveguides."
Methuen & Co. Ltd., 1950.

[3] A.W.Cross
"Experimental Microwaves."
Marconi Inst. Ltd. (Sanders Div.), 1977.

[4] J.Helszajn
"Passive & Active Microwave Circuits."
J.Wiley & Sons, 1978.

[5] J.Reed & G.J.Wheeler
"A method of analysis of symmetrical four-port networks."
IRE Trans. on Microwave Th. & Tech. MTT-4 246 1956.

[6] J.Reed
"The multiple branch waveguide coupler."
IRE Trans. on Microwave Th. & Tech. MTT-6 398 1958.

[7] K.G.Patterson
"A method for accurate design of a broad-band multibranch waveguide coupler."
IRE Trans. on Microwave Th. & Tech. MTT-7 466 1959.

[8] L.Young

"Synchronous branch guide directional couplers for low and high power applications."

IRE Trans. on Microwave Th. & Tech. MTT-10 459 1962.

[9] P.D.Lomer & J.W.Crompton

"A new form of hybrid junction for microwave frequencies."

Proc. IEE (pt.B) 104 261 1957.

[10] R.Levy

"A guide to the practical application of Chebyshev functions to the design of microwave components."

Proc. IEE (pt.C) 106 193 1959.

[11] R.Levy

"Directional couplers."

From "Advances in Microwaves."

Ed. L.Young

Academic Press Inc., 1966.

[12] R.Levy & L.F.Lind

"Synthesis of symmetrical branch-guide directional couplers."

IEEE Trans. on Microwave Th. & Tech. MTT-16 80 1968.

[13] H.J.Riblet

"Comment on 'Synthesis of symmetrical branch-guide directional couplers.' "

IEEE Trans. on Microwave Th. & Tech. MTT-18 47 1970.

[14] R.Levy

"Zolotarev branch-guide couplers."

IEEE Trans. on Microwave Th. & Tech. MTT-21 95 1973.

[15] E.Kuhn
"Exact calculation and some applications of the equivalent networks of open E-plane T-junctions."
Proc. of 5th Coll. on Microwave Communications IV PPMT 43/363-72 1974.

[16] E.Kuhn
"Improved design and resulting performance of multiple branch-waveguide directional couplers."
AEU 28 206 1974.

[17] S.B.Cohn & R.Levy
"History of microwave passive components with particular attention to directional couplers."
IEEE Trans. on Microwave Th. & Tech. MTT-32 1046 1984.

[18] K.C.Gupta, R.Garg & R.Chadha
"CAD of Microwave Circuits."
Artech House Inc., 1981.

[19] "Microwave Datamate."
Marconi Inst. Ltd., 1984.

[20] N.Marcuvitz (ed.)
"The Waveguide Handbook (Electromagnetic Wave Theory)."
IEEE, 1986.

## Chapter 4 Helix Design Producing A Longitudinal Electric Field

This is the second of two chapters concerning the structures used to couple microwave power into the active medium of a laser. A helical slow wave structure is examined which produces a large axial electric field, when microwave power is propagated along it. The nature of the electric field distribution around a free-standing helix, and its impedance, are investigated as a function of the helix parameters. The theory is then extended to describe the field distribution around the helix when it is incorporated in the laser coupling structure. The helix parameters which yield the highest axial electric field in the coupling structure are calculated. These are then compared with the optimum experimentally determined values.

### The travelling wave tube helix

Helices are used mainly in travelling wave tubes (TWTs) as slow wave structures. Consequently most helix design theory is biased towards the criteria required for optimum TWT operation. This section examines the principles behind the operation of a TWT and discusses the differences between TWT and laser helix requirements.

A TWT uses a slow-wave structure to retard the motion of a microwave field in order to optimise its interaction with a slower moving electron beam. Although there is a multitude of slow wave structures which can be used in a TWT, the two most common are the helix and the coupled cavity. The helix is used in most cases, except in high power applications where the coupled cavity is favoured for its superior

power handling ability.

The basic TWT produces an electron beam which is passed along the axis of the helix. A small microwave field is then fed into the helix producing an electric field along the axis. The pitch of the helix is chosen so that the microwave field progresses along the length of the helix with almost the same velocity as the electron beam. The electron beam interacts with the axial electric field and energy is transferred from the beam to the microwave field travelling along the helix. In this way the microwave field is amplified. Commercially available TWTs can have gains exceeding 50 dB.

The interaction between the electron beam and the axial electric field has been studied by [1]-[3]. Qualitatively, the axial electric field can be found by considering a length of conductor carrying a microwave signal. At a particular instant, the electric field distribution has the form shown on fig 4.1. This field pattern moves along the conductor at a velocity close to that of light. If this wire is now wound into a helix with, for example, four turns per wavelength, the field distribution becomes that shown on fig 4.2. This field pattern moves along the helix with a velocity which is reduced by the pitch of the helix to approximately that of the electron beam. Electrons passing along the axis of the helix experience an accelerating or retarding force depending upon their position with respect to the electric field. Bunches of electrons are then formed at points A on figs 4.2 and 4.3. The fields produced by the bunched electrons enhance the field in the helix which then increases the bunching still further. The amplified field is obtained in the helix at the expense of the kinetic energy of the electron beam. The helix is wound so that the field velocity along the axis is slightly less than that of the electron beam. Hence, more

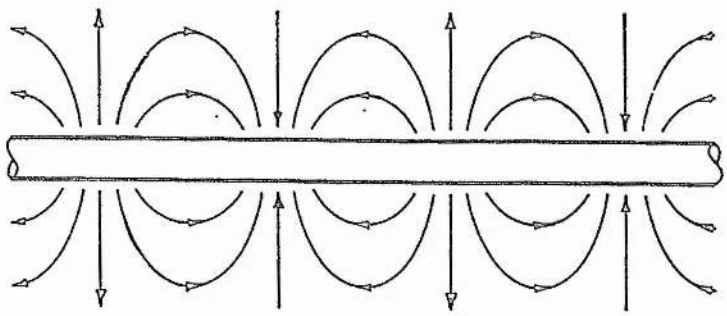

FIGURE 4.1 ELECTRIC FIELD PATTERN FOR A SINGLE-WIRE TRANSMISSION LINE.
(From A.S.Gilmour (Jr.) 1986 [3]).

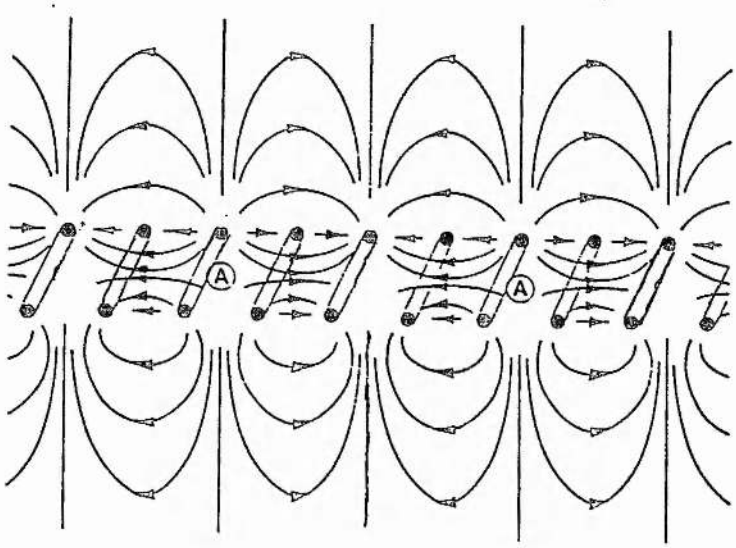


FIGURE 4.2 ELECTRIC FIELD PATTERN FOR A HELIX WITH 4 TURNS/WAVELENGTH.
(From A.S.Gilmour (Jr.) 1986 [3]).

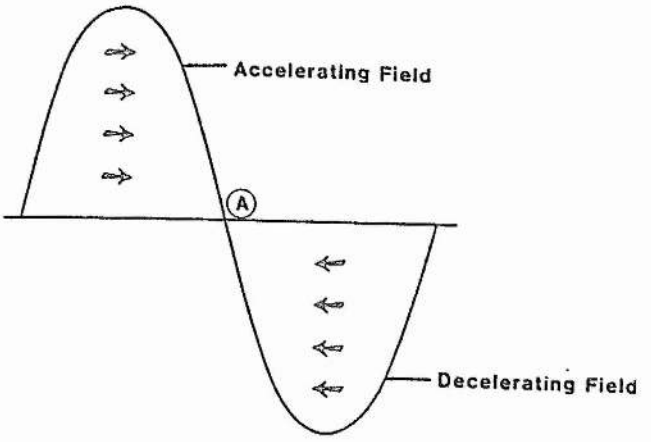


FIGURE 4.3 AXIAL FIELD THAT CREATES BUNCHING OF THE ELECTRON BEAM IN A TWT.
(From A.S.Gilmour (Jr.) 1986 [3]).

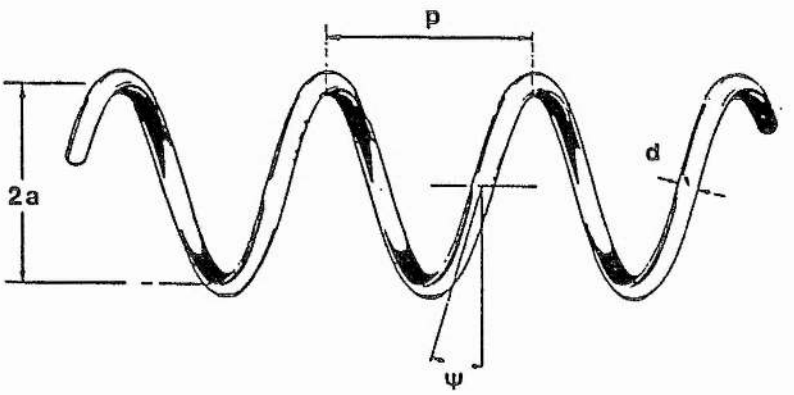


FIGURE 4.4 THE GEOMETRY OF A HELIX.
(From J.F.Gittins 1964 [2]).

electrons are in the retarding field than in the accelerating field, and as the beam passes along the helix the bunches become more and more compact. The microwave field is amplified exponentially until saturation effects set in. These are due to electron bunch instabilities and the gradual deceleration of the electron beam.

The requirements for efficiently exciting a gas discharge along the axis of a helix are less stringent than those for a TWT helix. The velocity of the microwave field as a result of the helix pitch is no longer important because the collisional nature of a gas discharge prevents the formation of electron bunches. For the laser helix it is important to create the largest possible axial electric field. The free electrons in the gas discharge do not behave as an electron beam, but absorb energy from the field, as described in chapter 2. In some respects, the laser helix can be considered to operate as a TWT in reverse.

**Electric field distribution around a helix**

As has already been explained, for a helical laser coupling structure, the helix parameters shown on fig 4.4 should be chosen to maximise the axial electric field. Two cases will be considered here; an unsupported helix in free space, and a helix wound round a glass tube and contained in a metallic cylinder.

The fundamental field equations from the solution of the wave equation for a plane wave propagating in the z-direction are [4],

$$
\begin{aligned}
E_{zn} &= [A_n\, I_0(\gamma_n r) + B_n\, K_0(\gamma_n r)]\, \exp[i(\omega t-\beta z)] \\
H_{zn} &= [C_n\, I_0(\gamma_n r) + D_n\, K_0(\gamma_n r)]\, \exp[i(\omega t-\beta z)] \\
E_{\phi n} &= -(i\omega\mu_n/\gamma_n)\, [C_n\, I_1(\gamma_n r) - D_n\, K_1(\gamma_n r)]\, \exp[i(\omega t-\beta z)] \\
H_{\phi n} &= (i\omega\mu_n/\gamma_n)\, [A_n\, I_1(\gamma_n r) - B_n\, K_1(\gamma_n r)]\, \exp[i(\omega t-\beta z)] \,.
\end{aligned}
\qquad (4.1)
$$

The wave propagates with velocity $v = \omega/\beta$ and the radial propagation coefficient in region n is defined by $\gamma_n^2 = \beta^2 - \omega^2\varepsilon_n\mu_n$, where $\beta$ is the axial phase constant, $\omega$ is the angular frequency of the field, and $\varepsilon_n$ and $\mu_n$ are the permittivity and permeability. Because the fields are finite on the axis and vanish at infinity, $B_1 = D_1 = A_4 = C_4 = 0$. The rest of the constants $A_n$ to $D_n$ are found by applying the boundary conditions for the case being studied. The equations for the radial fields $E_{rn}$ and $H_{rn}$, are similar to those of eqs 4.1.

(i) A free-standing helix

Propagation along a helix is difficult to study but the situation can be simplified by approximating a helix to a helically conducting cylindrical sheet. The cylindrical sheet, as shown on fig 4.5, is assumed to be perfectly conducting in the helical direction, and non-conducting in directions normal to this. For a free-standing helix with no surrounding objects to distort the field distribution, the electric fields of eqs 4.1 become [1];

Inside helix:

$$E_z(r) = B\, I_0(\gamma r)\, \exp[i(\omega t-\beta z)]$$

$$E_r(r) = i\, B\, (\beta/\gamma)\, I_1(\gamma r)\, \exp[i(\omega t-\beta z)]$$

$$E_\phi(r) = -\, B\, [I_0(\gamma a) / I_1(\gamma a)]\, \tan\psi\, I_1(\gamma r)\, \exp[i(\omega t-\beta z)]$$

Outside helix: (4.2)

$$E_z(r) = B\, [I_0(\gamma a) / K_0(\gamma a)]\, K_0(\gamma r)\, \exp[i(\omega t-\beta z)]$$

$$E_r(r) = -i\, B\, (\beta/\gamma)\, [I_0(\gamma a) / K_0(\gamma a)]\, K_1(\gamma r)\, \exp[i(\omega t-\beta z)]$$

$$E_\phi(r) = -\, B\, [I_0(\gamma a) / K_1(\gamma a)]\, \tan\psi\, K_1(\gamma r)\, \exp[i(\omega t-\beta z)].$$

The constant B is to be determined, and the modified Bessel functions $I_0$, $I_1$, $K_0$ and $K_1$ of argument $\gamma r$, are given in appendix A at the end of the chapter. The helix pitch angle $\psi$ is given by,

$$\tan\psi = p/2\pi a, \qquad (4.3)$$

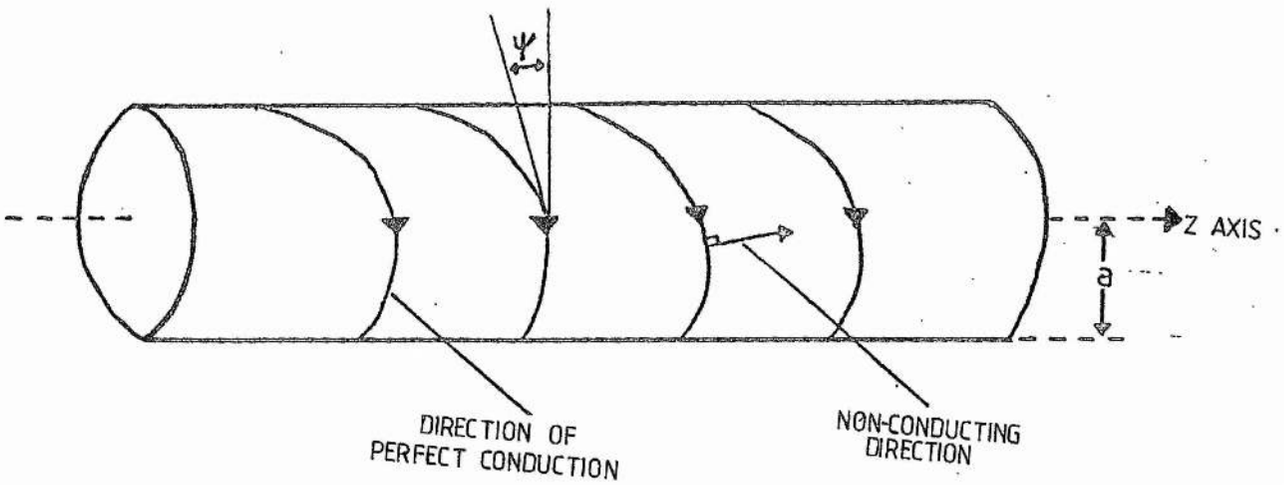


FIGURE 4.5 HELICALLY CONDUCTING CYLINDRICAL SHEET.

where p and a are the helix pitch and radius respectively, as shown on fig 4.4.

The radial propagation constant $\gamma$ is found from an expression derived from the boundary conditions at the helix surface. For a free-standing helix, the tangential electric field must be perpendicular to the helix direction and continuous across the cylindrical sheet, and the tangential magnetic field must be parallel to the helix direction. Writing the free-space phase constant $\beta_o$ as $\omega/c$, this gives [1],

$$(\gamma a)^2 \frac{I_0(\gamma a)\, K_0(\gamma a)}{I_1(\gamma a)\, K_1(\gamma a)} = (\beta_o a \cot\psi)^2 \ . \tag{4.4}$$

This is called the dispersion relation. It gives the variation of the speed of a microwave signal, of a particular frequency, as it passes along a helix, and can be used to calculate the operational bandwidth of a TWT helix. This function is graphed on figs 4.6a and 4.6b, and it can be seen that when $\gamma a$ is large, it is approximately equal to $\beta_o a \cot\psi$. This gives,

$$\beta = \sqrt{\gamma^2 + \beta_o^2} \simeq \beta_o / \sin\psi, \tag{4.5}$$

and

$$v_p = \omega/\beta \simeq c \sin\psi. \tag{4.6}$$

The phase velocity $v_p$ represents the axial speed of the microwave field.

A parameter called the coupling impedance K, which has units of ohms, is defined as,

$$K = |E_z(0)|^2 \ / \ (2\beta^2 P). \tag{4.7}$$

It can be used to describe the magnitude of the axial electric field $E_z(0)$ for a given transmitted power P. This parameter can be used to define the efficiency of a helix at providing an axial electric field. The power carried by a helix can be derived by integrating the Poynting vector given by eq 2.32 over the plane perpendicular to the helix direction. This becomes,

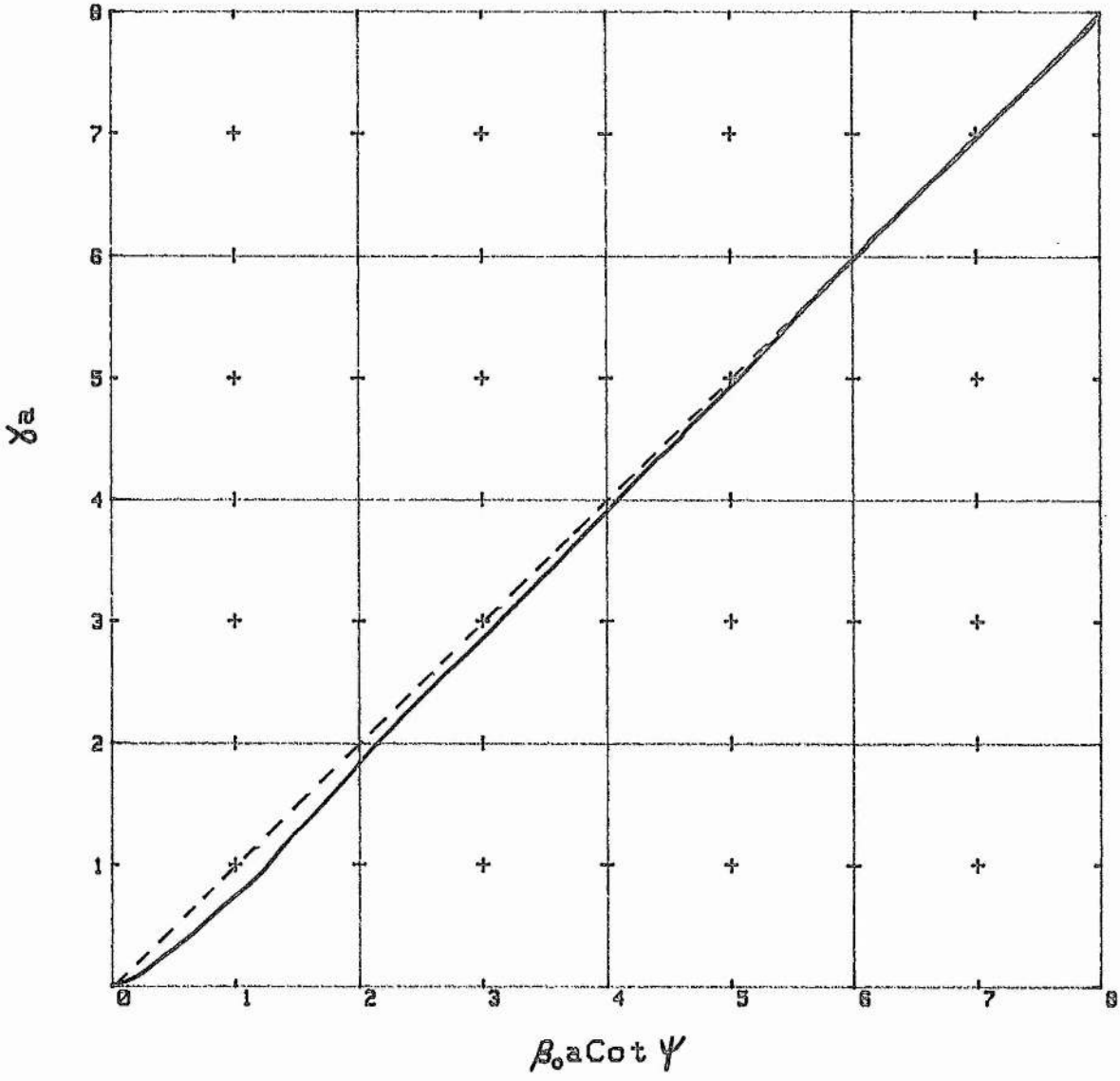


FIGURE 6.6a
VARIATION OF γa FOR AN UNSUPPORTED
HELICALLY CONDUCTING CYLINDER

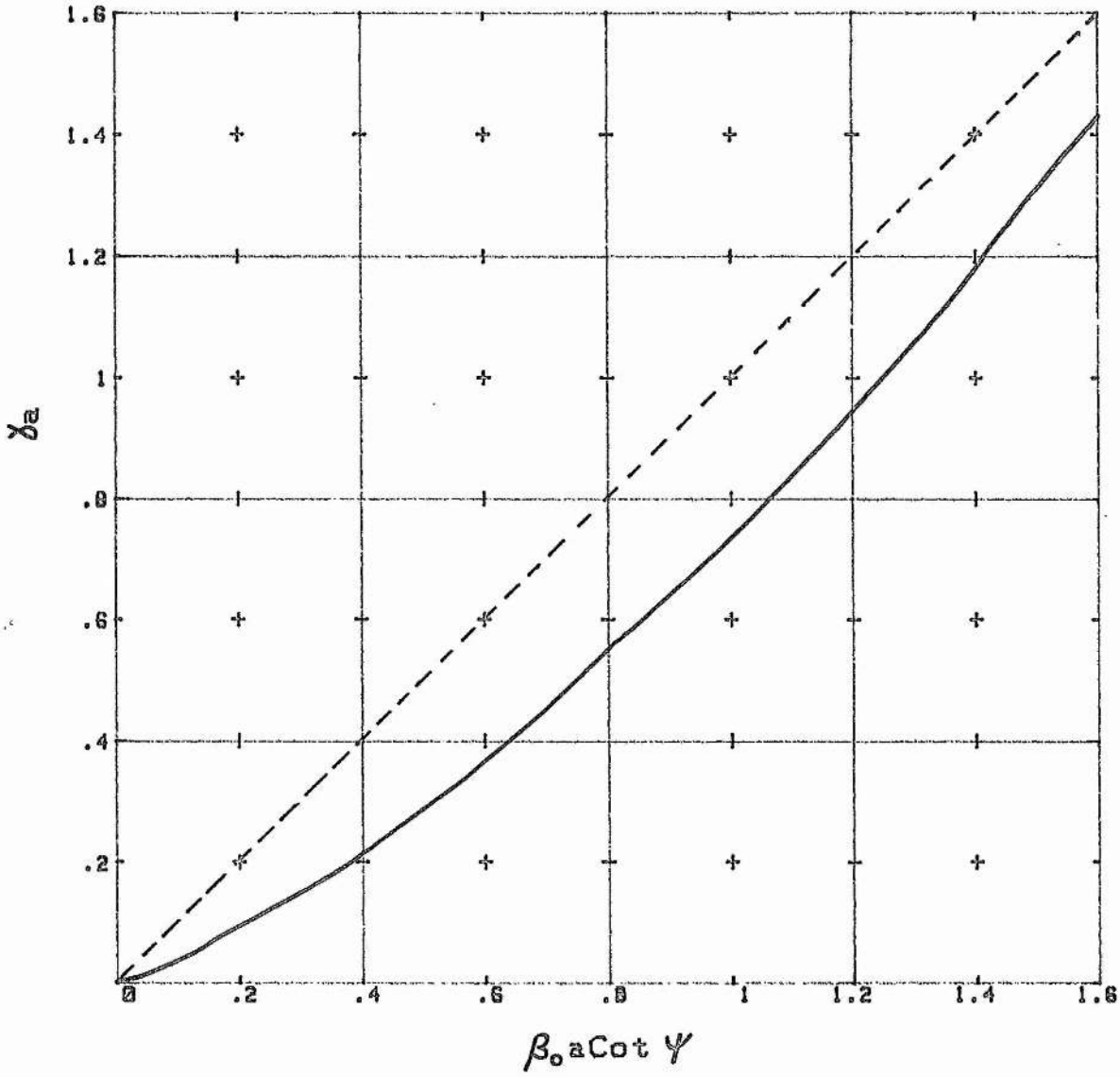


FIGURE 4.6b
VARIATION OF $\gamma_a$ FOR AN UNSUPPORTED HELICALLY CONDUCTING CYLINDER

$$P = \pi \mathrm{Re}\left[\int_o^a (E_{r1}H^*_{\phi 1} - E_{\phi 1}H^*_{r1})\, r\, dr + \int_a^\infty (E_{r2}H^*_{\phi 2} - E_{\phi 2}H^*_{r2})\, r\, dr\right], \qquad (4.8)$$

where the integral is applied across the plane normal to the propagation direction. The magnetic field equations required for the solution of eq 4.8 are found by following the same procedure used to derive eqs 4.2. Substitution of the solution of eq 4.8 into 4.7 gives [1],

$$|E_z(0)|^2 / (2\beta^2 P) = 1/2\ (\beta/\beta_o)\ (\gamma/\beta)^4\ F^3(\gamma a), \qquad (4.9)$$

with

$$F(\gamma a) = \left(\frac{\gamma a}{240}\frac{I_0}{K_0}\left[\left(\frac{I_1}{I_0} - \frac{I_0}{I_1}\right) + \left(\frac{K_0}{K_1} - \frac{K_1}{K_0}\right) + \frac{4}{\gamma a}\right]\right)^{-1/3}, \qquad (4.10)$$

where $I_{0,1}$ and $K_{0,1}$ have arguments $\gamma a$. The axial electric field can then be calculated using,

$$|E_z(0)| = [(\gamma^4/\beta\beta_o)\ F^3(\gamma a)\ P]^{1/3}. \qquad (4.11)$$

Equation 4.11 can be used to find the constant B in eqs 4.2 using the fact that $I_0(0) = 1$, (see appendix A). The magnitude of the longitudinal component of the field inside the helix at a distance r from the axis is then given by,

$$E_z(r) = I_0(\gamma r)\ E_z(0). \qquad (4.12)$$

Expressions for the other field components of eq 4.2 can then also be determined explicitly.

The approximation of using a helically conducting sheet neglects the effect of wire thickness and the interaction between adjacent turns on an actual helix. Essentially the model does not consider the "wire component" of a helix, but only its shape. When the effect of the wire is taken into account, it is found that the coupling impedance is reduced [1]. As shown on fig 4.7, the degree to which this occurs depends upon the ratio between the diameter of the wire and the helix pitch d/p, and the number of turns per wavelength.

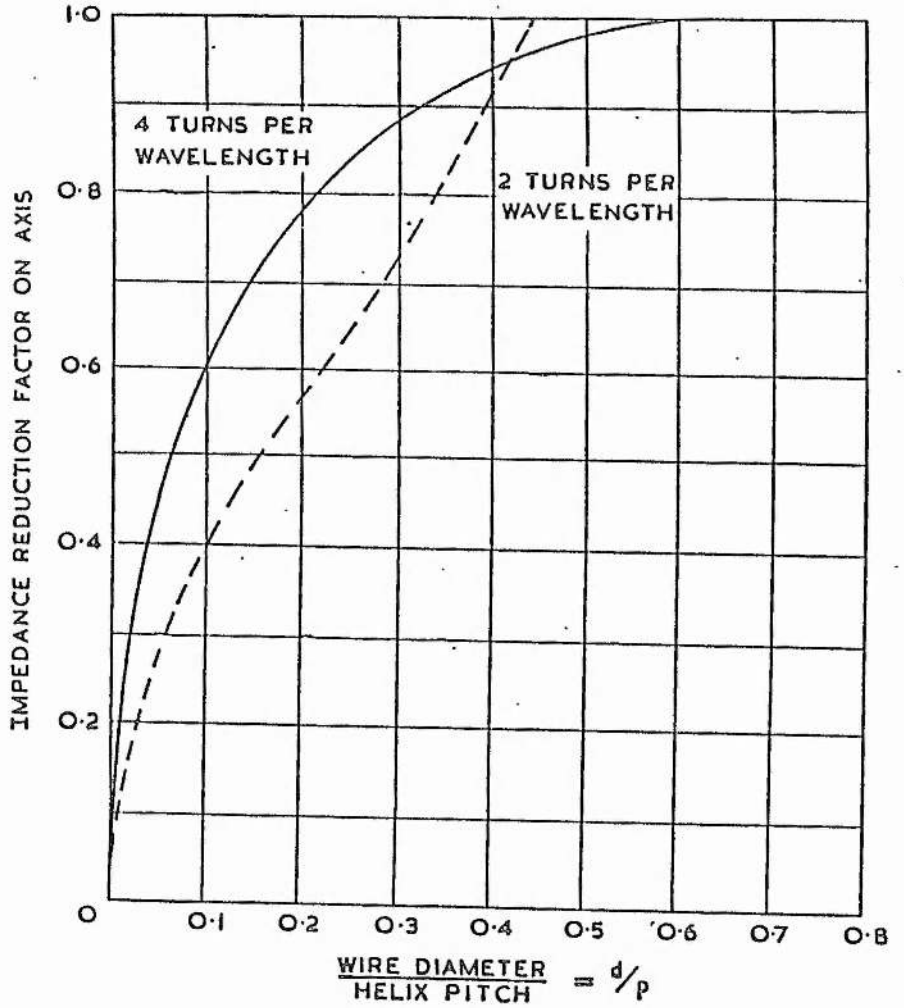


FIGURE 4.7 EFFECT OF WIRE SIZE ON COUPLING IMPEDANCE.
(From J.R.Pierce 1950 [1] ).

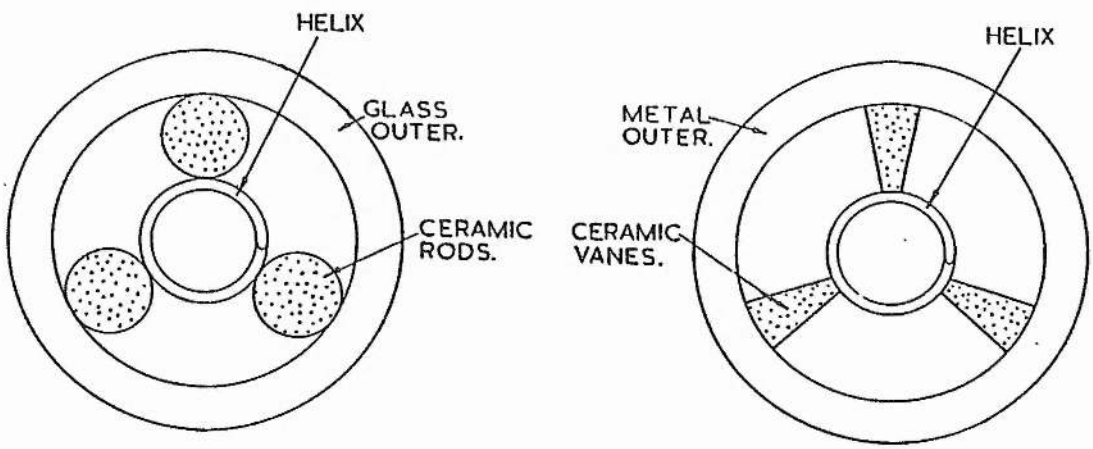


FIGURE 4.8 EXAMPLES OF HELIX SUPPORTING STRUCTURES.
(From J.F.Gittins 1964 [2]).

(ii) A supported helix in a metallic cylinder

In practice, helices are often contained in dielectric or metallic tubes for support, or to prevent the leakage of microwave radiation. They are also sometimes supported in these tubes by rods or vanes, and some typical arrangements used in TWTs are shown on fig 4.8. The presence of these structures can have a detrimental effect on the coupling impedance, and the closer they are to a helix, the greater will be their effect. The dielectric properties of the supporting and containing structures impose new boundary conditions on the solution of eq 4.1. This results in a perturbation of the fields of eq 4.2 of the free-standing helix.

The presence of objects surrounding a helix considerably complicates the mathematical analysis of the system. The equations and algebraic simplifications are lengthy and are too involved to be included here. Nevertheless, the field distribution inside the helix is of interest, and in view of this, the analytical procedure will be outlined with the appropriate references. The procedure is essentially the same as that already outlined for a free-standing helix except that the boundary conditions are more complicated.

The configuration used was chosen for practical reasons associated with the development of the laser coupling structure, and this will be discussed later. Here, as shown on figs 4.9a and b, a helix is wound round a glass tube containing the gas fill, and is contained in a metallic cylindrical tube to prevent microwave leakage. Although this arrangement is not the most efficient which could have been used, the principles which follow can be applied to a wider range of circumstances.

The field equations 4.1 are solved for the configuration of fig

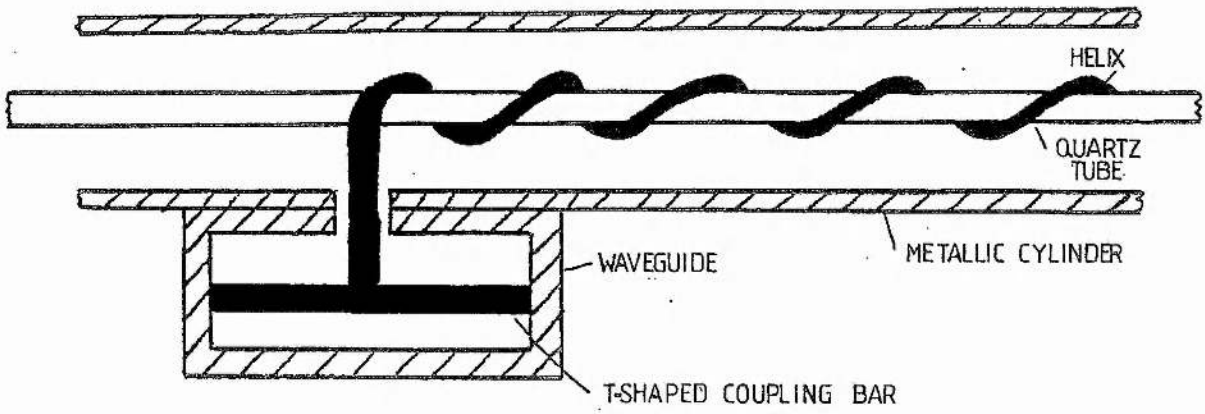


FIGURE 4.9a THE WAVEGUIDE-TO-HELIX TRANSITION WITH THE HELIX WRAPPED ROUND A GLASS TUBE WHICH CONTAINS THE GAS FILL.

FIGURE 4.9b THE COMPLETE HELICAL LASER COUPLING STRUCTURE.

4.9a by applying the appropriate boundary conditions [1],[4]. At the metallic cylinder, the electric field components $E_z$ and $E_\phi$ must be zero, and across the helix/glass-tube and glass-tube/free-space interfaces, the electric and magnetic field components $E_z$, $E_\phi$, $H_z$, and $H_\phi$ must be continuous. The remaining conditions are the same as those for a free-standing helix.

Using the formulated boundary equations, a set of simultaneous equations can be constructed to calculate, in parametric form, the unknown field components [6]-[7]. For these equations to have a non-trivial solution, a determinant equation must be solved [4]. The solution of this gives the dispersion equation which is equivalent to eq 4.4 for a free-standing helix. This equation can be used to calculate $\gamma$, and for the configuration here, is the dispersion equation given in equation 1 in [6].

In order to solve the field equations explicitly, the coupling impedance must be considered in the same manner as was done for the unsupported helix. Here the coupling impedance of eq 4.9 becomes [5],

$$|E_z(0)|^2 / (2\beta^2 P) = 1/2 \, (\beta/\beta_o) \, (\gamma/\beta)^4 \, f^3(\gamma a), \qquad (4.13)$$

with

$$f(\gamma a) = (a_C/a_L)^{-1/6} \, \gamma a \, F(\gamma a). \qquad (4.14)$$

Here, $a_C$ and $a_L$ represent the ratio of the capacitance and inductance per unit length of supported and free-standing helices [5],[8].

The correction factor resulting from the introduction of the metallic cylinder and glass tube to a free-standing helix is found from eq 4.14. From this new coupling impedance all the field components can be explicitly evaluated. By applying different boundary conditions, a whole range of configurations can be analysed [8]-[12]. The accuracy of this procedure is limited principally by the helically conducting

cylindrical sheet approximation.

A good intuitive feel for the behaviour of the electric field distribution around a supported helix can be obtained by adopting a qualitative approach. This is done by considering the perturbing effect of the supporting and shielding structures upon the field distribution of a free-standing helix. In the case being studied, the field pattern is not changed, but the field concentration in specific areas is. The presence of the metallic cylinder and glass tube both have an adverse effect upon the coupling impedance of the helix. The outer metallic cylinder forces the power to concentrate in the region contained by the cylinder. This manifests itself in an increased radial electric field and a reduced axial field. This is most pronounced at low frequencies (small $\gamma a$), and is negligible for large $\gamma a$ [5],[12]. The effect of the cylinder can be reduced by increasing its radius. The inner dielectric tube tends to concentrate the electric field between its inner surface and the helix, once again reducing the axial electric field. This effect is most pronounced at high frequencies [5], and can be minimised by using a thin tube made of a material with a low dielectric constant. The magnitude of the drop in the axial field due to the structures surrounding the helix can only be found by carrying out the analysis outlined earlier. However, associated with any drop in axial field, is an increase in the radial component which is by no means useless when powering a laser discharge at microwave frequencies. (Also, whilst the supporting and containing structures impair the axial electric field of a helix, they can still improve the dispersive qualities which is of benefit to TWT helices).

A computer program to calculate the electric fields around an unsupported helix is listed in appendix B. This program is used to plot

the longitudinal electric field distribution as a function of microwave frequency, helix pitch and radius. It can be seen from figs 4.10 to 4.12 that the longitudinal electric field drops off away from the helix and that the rate of decline depends upon the operating parameters. Figures 4.13 and 4.14 show that the longitudinal electric field component is dominant inside the helix and that, at the axis, the electric field is purely longitudinal. These trends are in agreement with [13].

To a first approximation, the field distributions of figs 4.10 to 4.14 also apply for the supported helix used in the laser coupling structure of fig 4.9. As has already been explained, the supporting structures have a perturbing effect on the fields, but the trends are still the same.

The laser coupling structure was designed to operate at 10 GHz. The helix radius is also constricted, to a value of around 3 mm (as measured from the centre of the glass tube, to the centre of the helix wire with thickness 1 mm). This is because a noble gas ion laser discharge tube has an optimum internal diameter of around 3 mm, and because the glass tubes used have a wall thickness of 1 mm. It can be seen from fig 4.10 that, for an unsupported helix of radius 0.003 m, and pitch 0.01 m, the axial electric field has a value of 400 kV/m. Also, the electric field is fairly uniform across the diameter of the helix. The internal glass tube introduces a steeper drop in the field in the glass, but inside the tube, the field is once again almost uniform. From chapter 2 on the microwave discharge, it can be seen that only up to 10% of the incident microwave power penetrates the glass-tube/gas-discharge boundary. This gives an axial field of less than 20 kV/m inside the laser tube.

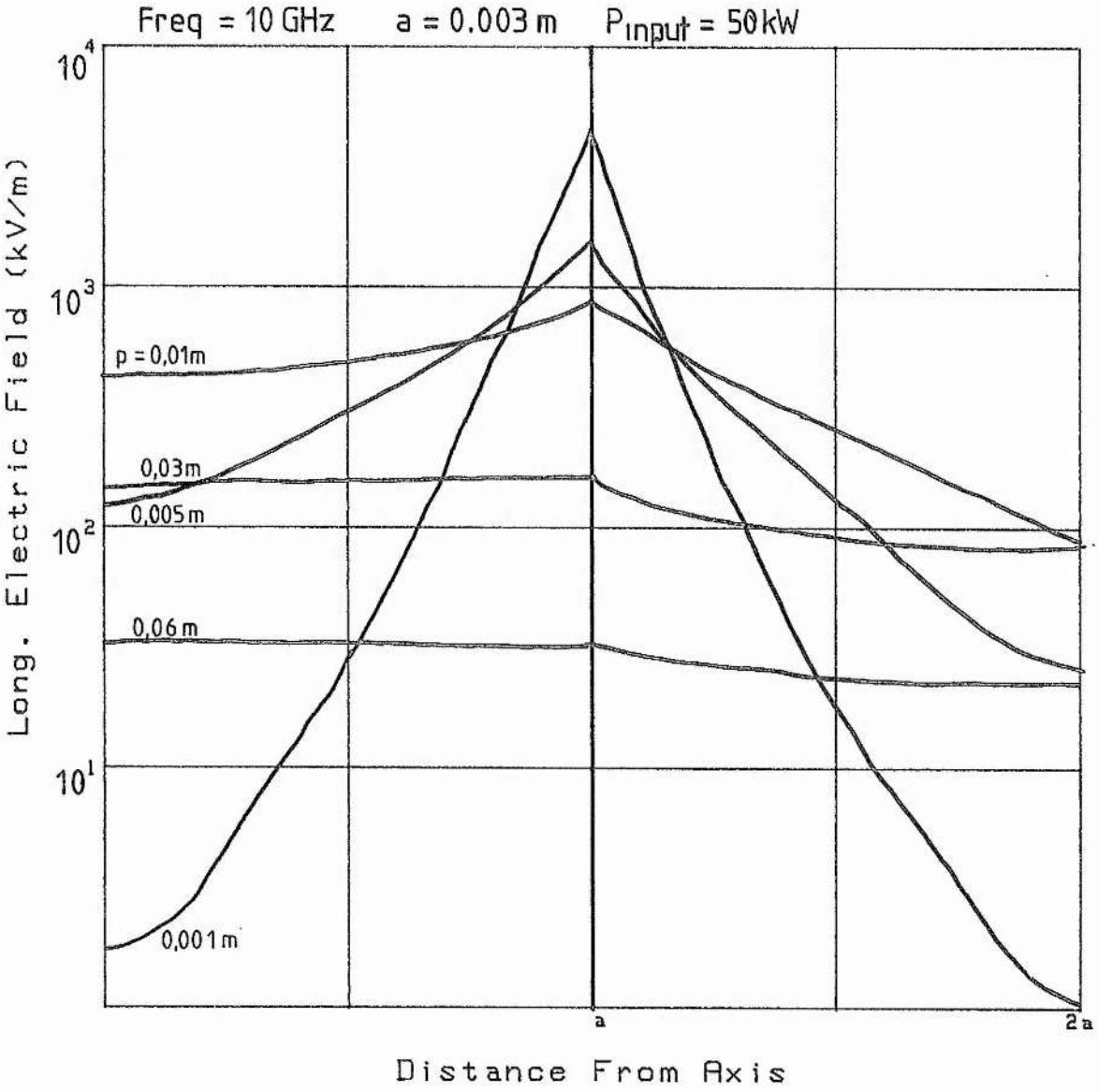


FIGURE 4.10

EFFECT OF HELIX PITCH UPON THE LONGITUDINAL FIELD DISTRIBUTION

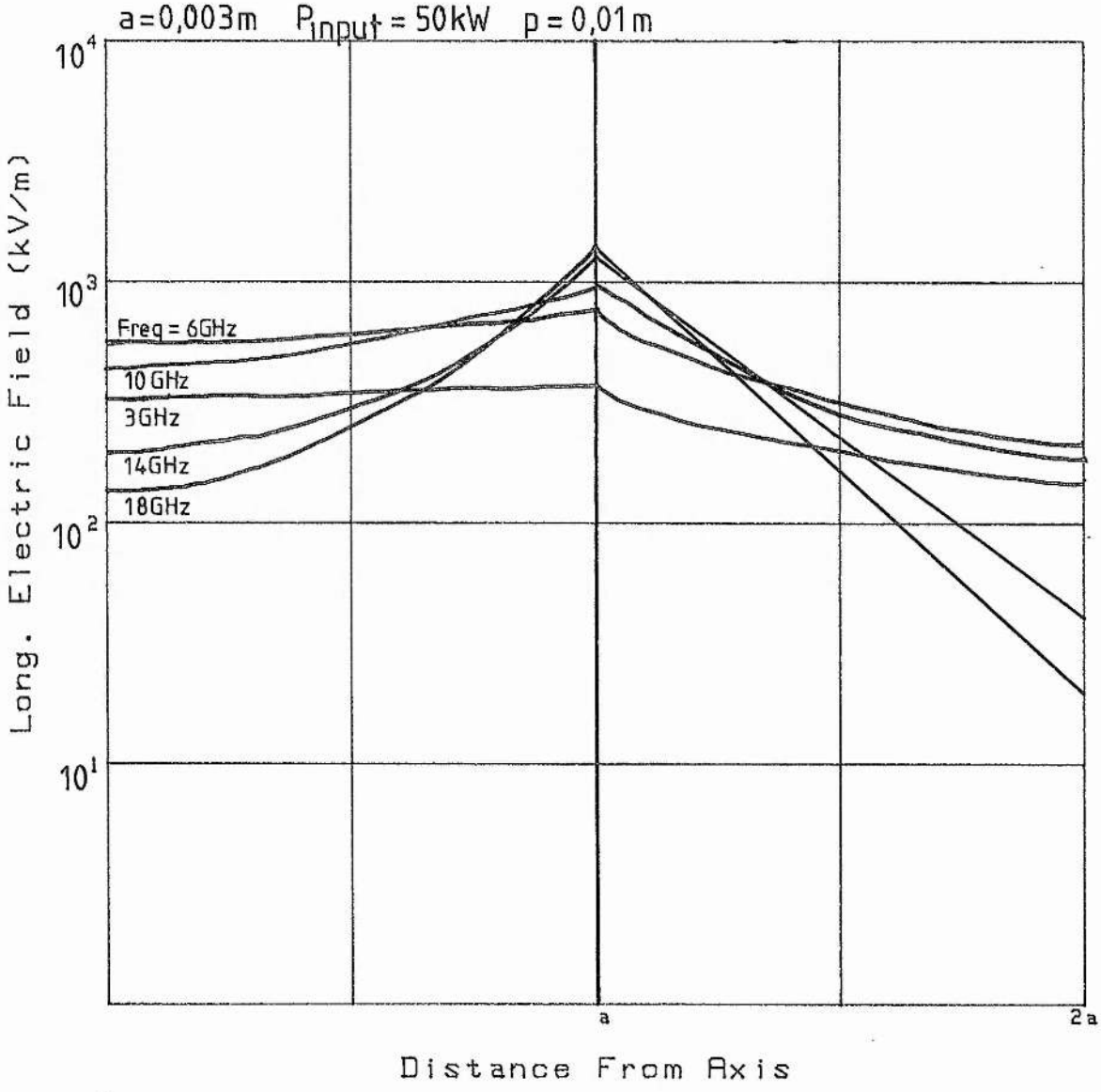


FIGURE 4.11

EFFECT OF MICROWAVE FREQUENCY UPON THE LONGITUDINAL FIELD DISTRIBUTION

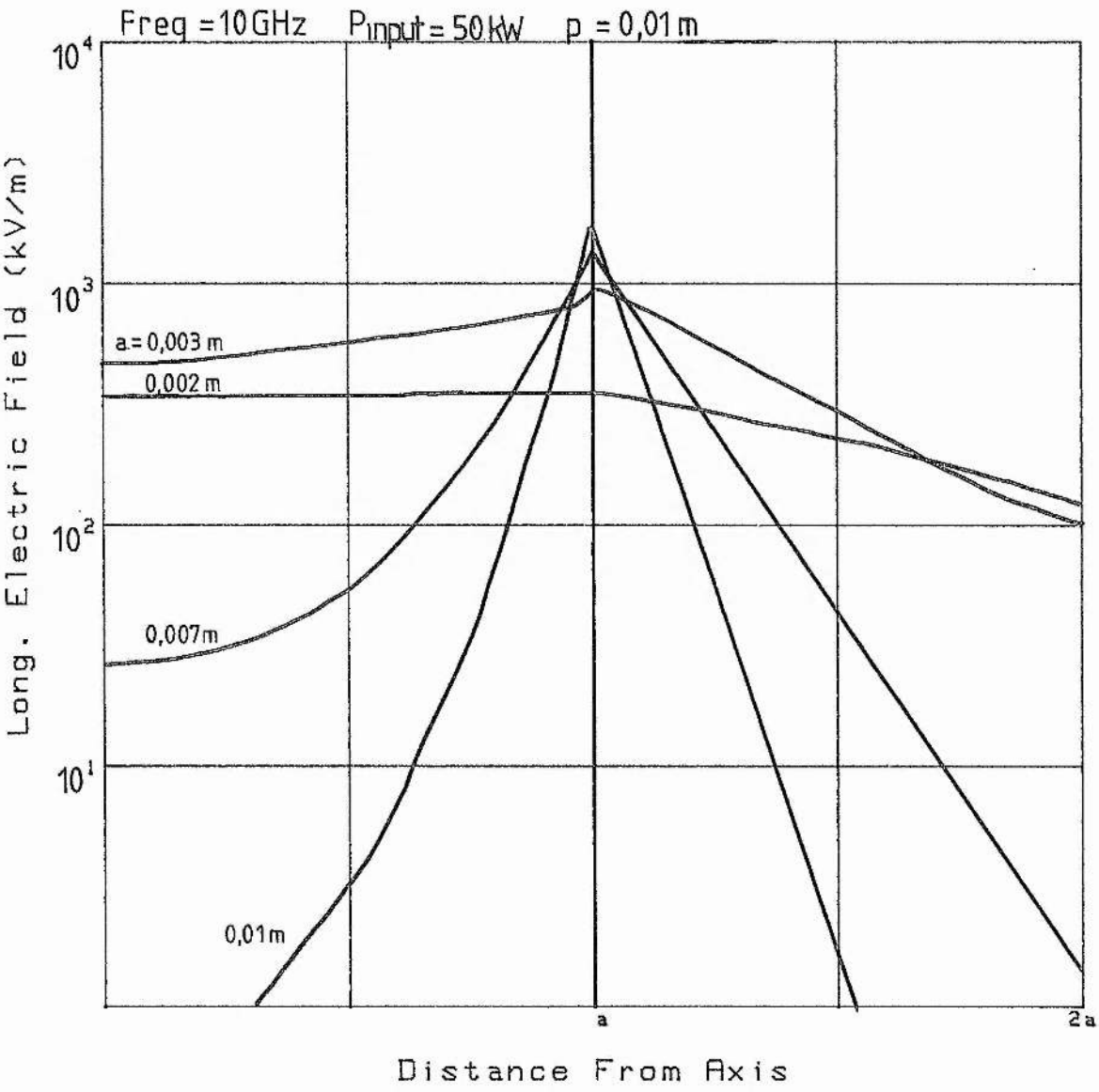


FIGURE 4.12

EFFECT OF HELIX RADIUS UPON THE LONGITUDINAL FIELD DISTRIBUTION

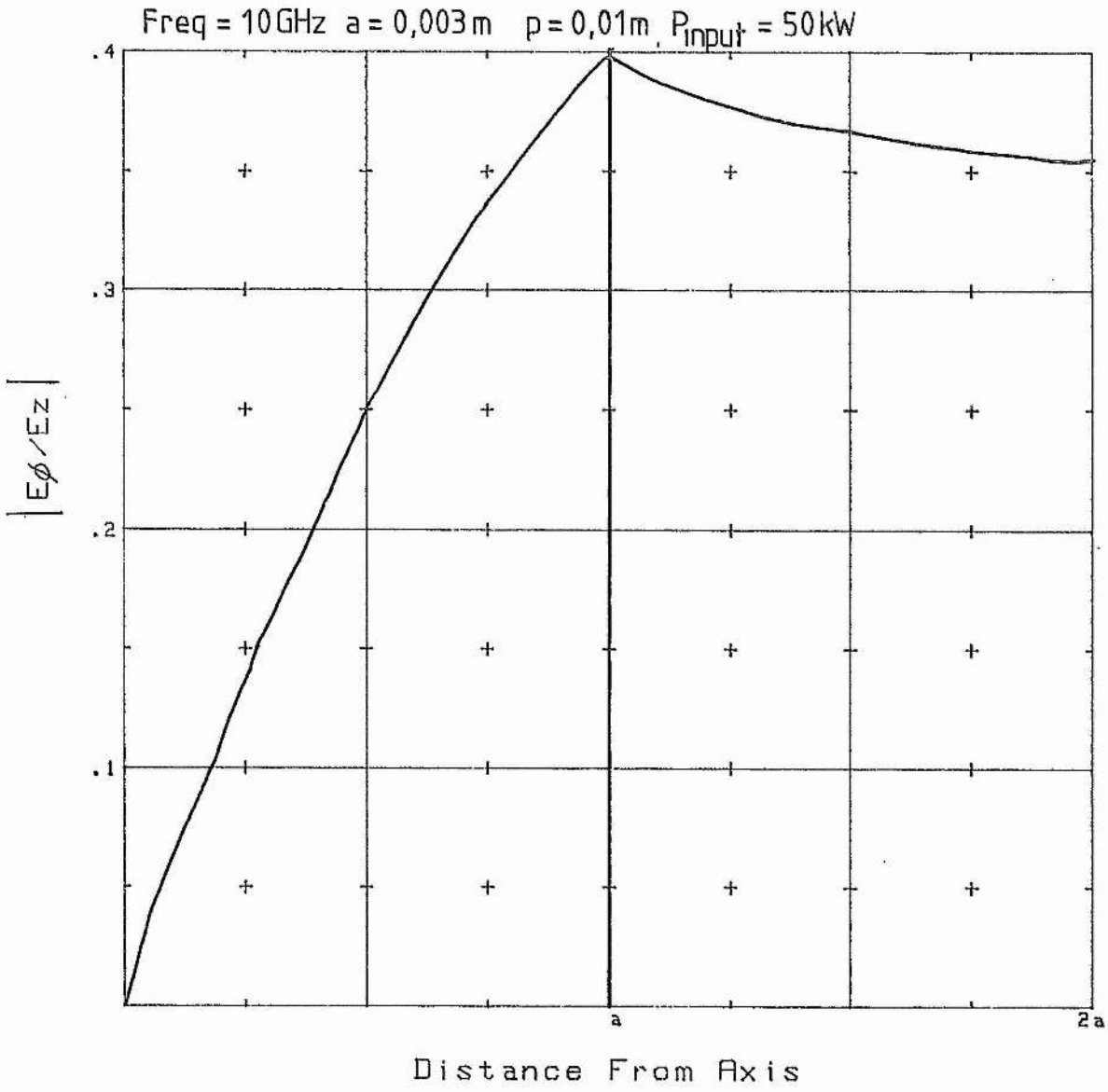


FIGURE 4.13

DISTRIBUTION OF THE RATIO BETWEEN THE ANGULAR & LONGITUDINAL ELECTRIC FIELDS

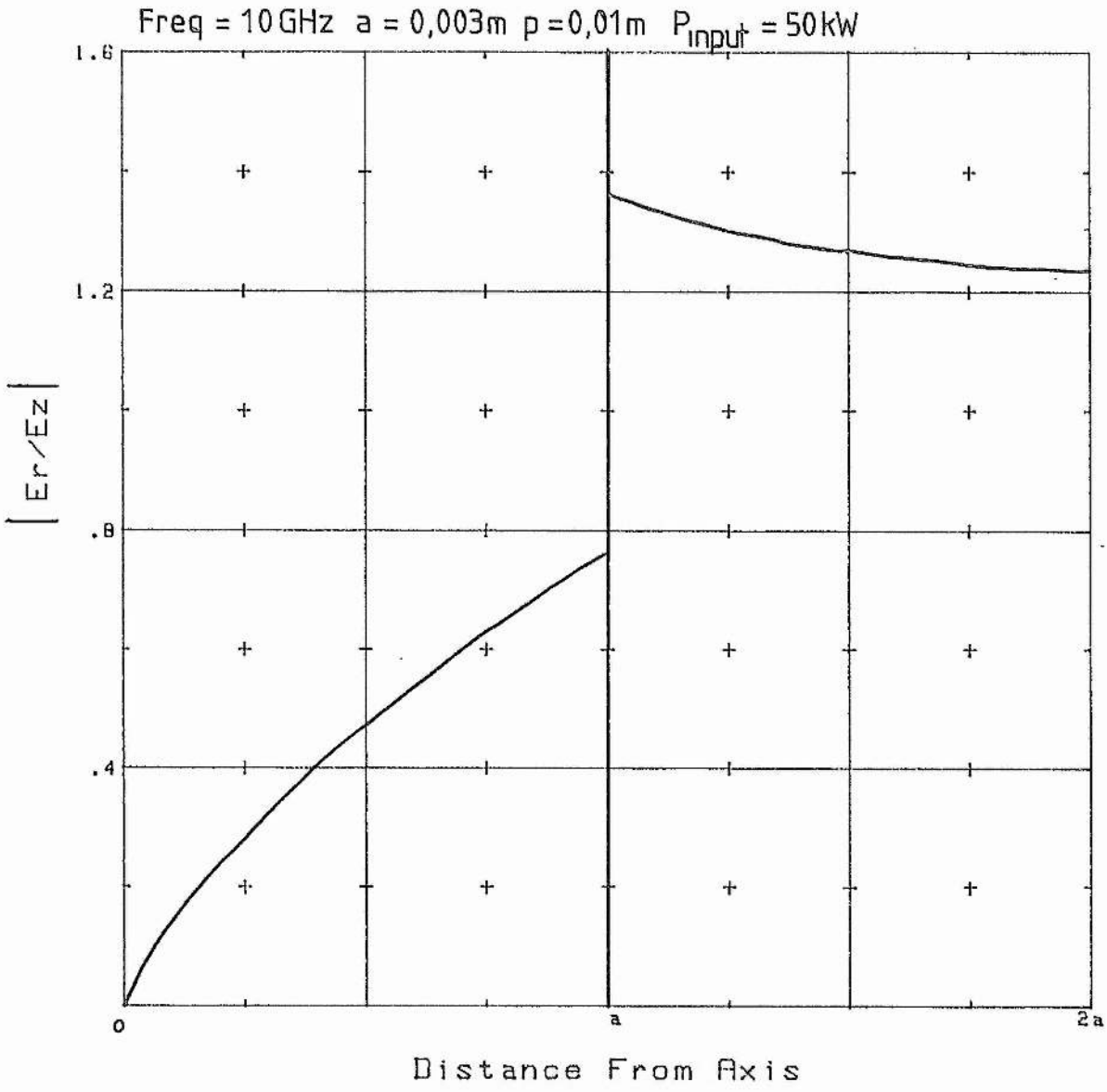


FIGURE 4.14

DISTRIBUTION OF THE RATIO BETWEEN THE RADIAL & LONGITUDINAL ELECTRIC FIELDS

Helix impedance

For the helical coupling structures to operate efficiently, there must be a smooth impedance transition between the waveguide supplying the microwave power, with an impedance of around 500Ω, and the helix with a much lower impedance ($\sim 50\,\Omega$). This is achieved by using a T-shaped coupling bar, as shown on fig 4.9a, in conjunction with a waveguide short circuit placed a distance $\lambda_g/4$ behind the bar. This arrangement acts as a coaxial line to waveguide impedance transformer giving an effectively smooth impedance transition. In the case under study here, the wire passing through the waveguide and metallic cylinder forms the coaxial line. For maximum power transfer to the helix, the impedance of the helix must equal that of the coaxial line.

The helix parameters are chosen to maximise the axial electric field. However, the corresponding matching impedance of the helix does not necessarily equal that of the coaxial line. The matching impedance of a helix can be changed by varying the geometry of the helix and any surrounding structures. The matching impedance of a free-standing helix is a function of helix pitch and diameter. For the supported helix used in the laser coupling structure, the impedance also depends upon the diameter of the surrounding metallic shield and the thickness and dielectric constant of the dielectric tube.

The matching impedance of a helix can be defined by considering the current flow in a helically conducting sheet [12]. Here, the current flow depends upon the discontinuity between the angular magnetic fields across the sheet surface. Defining the matching impedance as,

$$Z_o = 2P/II^*, \qquad (4.15)$$

where P is the power flowing in the sheet and I is the current, (where * denotes the complex conjugate), the matching impedance can be written as,

$$Z_o = P/[2\pi^2 a^2 (H_{\phi 2} - H_{\phi 1})^2]. \qquad (4.16)$$

The angular component of the magnetic field just outside the sheet surface is $H_{\phi 2}$, and $H_{\phi 1}$ is the field just inside. For an unsupported helix, both components have a similar form to those given in eqs 4.2 [1]. The accuracy of this is limited by the approximation of using a helically conducting sheet to represent the helix. Impedance calculations based on this approximation have been found to agree well with the measured values of actual helices [12].

The matching impedances of a number of free-standing helices with different pitches and diameters have been calculated using the computer program listed in appendix B. As can be seen from fig 4.15, the matching impedance is a sensitive function of helix pitch and diameter. For a smooth impedance transfer, the impedance of the helix at the input end must equal that of the coaxial line which is given by,

$$Z_c = \frac{60 \ln (b/a)}{\sqrt{\varepsilon_r/\mu_r}} , \qquad (4.17)$$

where a and b are the diameter of the wire and hole respectively. The relative permittivity $\varepsilon_r$, and permeability $\mu_r$, apply to the dielectric material between the inner and outer conductors. In this case they are both equal to 1. The coaxial line in the laser coupling structure has an impedance of approximately 60 $\Omega$. From fig 4.15, it can be seen that a free-standing helix of radius 0.003 m, and pitch 0.02 m, also has this impedance. Therefore, a smooth impedance transition, from the coaxial line to the helix, is achieved when the helix has a pitch of 0.02 m. From fig 4.10, it can be seen that the maximum axial electric field is achieved for a helix pitch of 0.01 m. If a high axial field is required therefore, the helix pitch must be tapered from 0.02 m at the input end, to 0.01 m for the rest of the helix.

In TWT design, an impedance transformation is usually required to

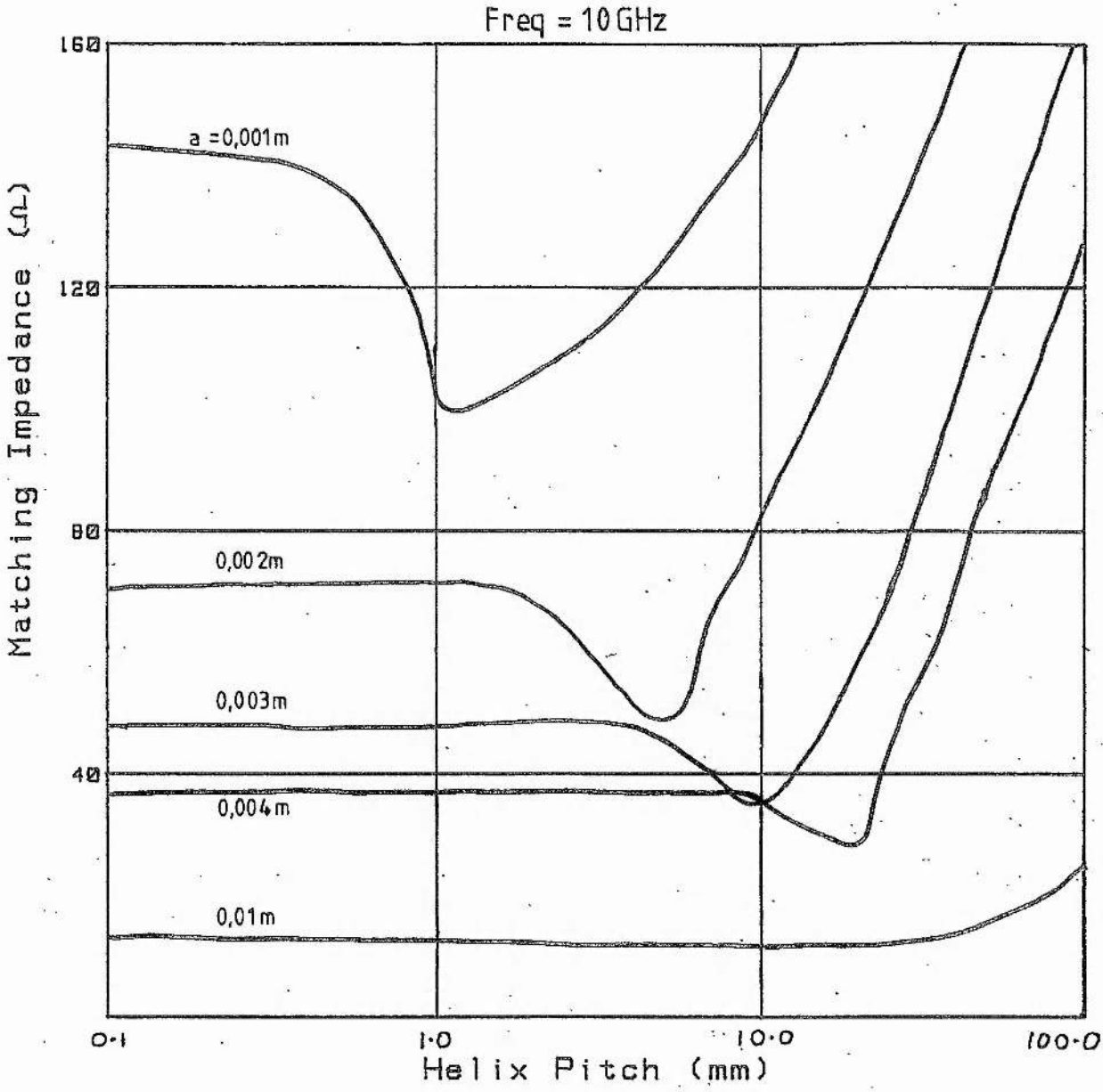


FIGURE 4.15

EFFECT OF HELIX PITCH AND RADIUS UPON HELIX MATCHING IMPEDANCE

convert between the waveguide or coaxial line input and outputs, and the helix. When calculating the impedance of the helix, a dielectric loss factor can be used to incorporate the impedance change caused by the surrounding structures. The dielectric loss factor can be determined experimentally, or derived from eq 4.16 using the appropriate magnetic fields. The loss factor has the effect of reducing the matching impedance of a helix, and for the TWT configurations of fig 3.8, has a value of approximately 0.7. For the laser coupling structure under consideration here, the helix is wrapped round a glass tube and so the contact area is much greater than in the case of fig 3.8. This larger contact area reduces the loss factor and an estimate of 0.5 is a good first approximation.

By applying the loss factor to the data on fig 4.15, it can be seen that a helix pitch of approximately 0.05 m is required to match with the coaxial line. It can be seen from fig 4.10 that the axial field for a helix with a pitch of 0.05 m is low. Therefore, it is important to taper the pitch quickly from the matching pitch to the best axial field pitch. It should be noted that no account has been taken of the gas discharge in the laser tube, either here, when calculating the impedance, or in the previous section concerning the field distribution.

**Experimental helix designs**

In conjunction with the theoretical study of helix design, a series of prototype helices were constructed. These were used to support the results of the theory already outlined, and ultimately to find the most effective helix dimensions.

The theory already outlined only gives an indication of how the field distribution around the laser helix varies as the helix parameters

are changed. The effects of the supporting tube and metallic cylinder are only partly considered and the presence of the gas discharge down the middle of the tube is completely neglected. The theory gives the approximate performance of the helix used in the coupling structure, but it cannot completely predict the optimum helix dimensions because of the presence of the laser discharge. The prototype helices were used to find the best conditions for excitation of the laser discharge and these will be described in this section.

(i) Performance of the helical laser prototypes

As has already been pointed out there are two important helix pitches; one with an impedance equal to that of the coaxial interface, and one for the helix giving the largest axial electric field. An experiment was carried out which should have found these two pitches and it will be described shortly. However, the experiment assumed that the gas discharge acted as a good microwave load, but as it turned out this is not the case.

The gas discharge along the centre of a helix has a complex dielectric constant as detailed in chapter 2. This influences the field distribution, propagation and impedance characteristics of the helix. These effects depend upon the dielectric constant of the discharge which is a function of the discharge parameters as given by eq 2.20. The gas discharge should act as a load, so that microwave energy is attenuated as it passes down the surrounding helix. Hence, microwave power fed into the helix should be absorbed with an efficiency being dictated by the pitch. Unfortunately however, the discharge absorbs only a small fraction of the incident power because in excess of 90% of the incident power is reflected at the glass-tube/gas-discharge boundary (see chapter 2).

A number of helices were constructed with pitches between 2 and 40 mm. They were all wrapped round a glass tube with an outside diameter of 5 mm, and all had a length of approximately 50 cm. One end of each helix was soldered to the coaxial pin and the other end was left unattached. The complete helical coupling device was then connected to the microwave apparatus of fig 4.16. The absorbed microwave power $P_{abs}$, given by,

$$P_{abs} = P_{inc} - P_{ref}, \qquad (4.18)$$

was found for each of the helices over a range of microwave frequencies, where $P_{inc}$ and $P_{ref}$ are the incident and reflected microwave powers. In each case, measurements were made firstly with a discharge in the tube at an Argon pressure of 0.07 mB, and then without a discharge with the tube under vacuum. In this way a distinction could be made between the power absorbed by the gas discharge and that absorbed by resonances in the coupling structure. It should be noted here that the matching impedance of the helix is changed when the discharge is present, and that differences between $P_{abs}$ with and without a discharge also include this effect.

The results obtained indicate that the power absorbed by the gas is small. For all the helices, there is only a small difference between the power absorbed with and without a gas discharge. This means that the majority of the absorbed power is expended in oscillations set up in the coupling structure. This is further substantiated by the fact that no pronounced frequency dependance of the absorbed power is observed. The absorbed microwave power was measured as a function of the frequency of the input over the range 8.7 - 9.6 GHz. If large amounts of microwave power were absorbed by the gas, the absorbed power would be observed to be a function of microwave frequency, with a maximum centred at a

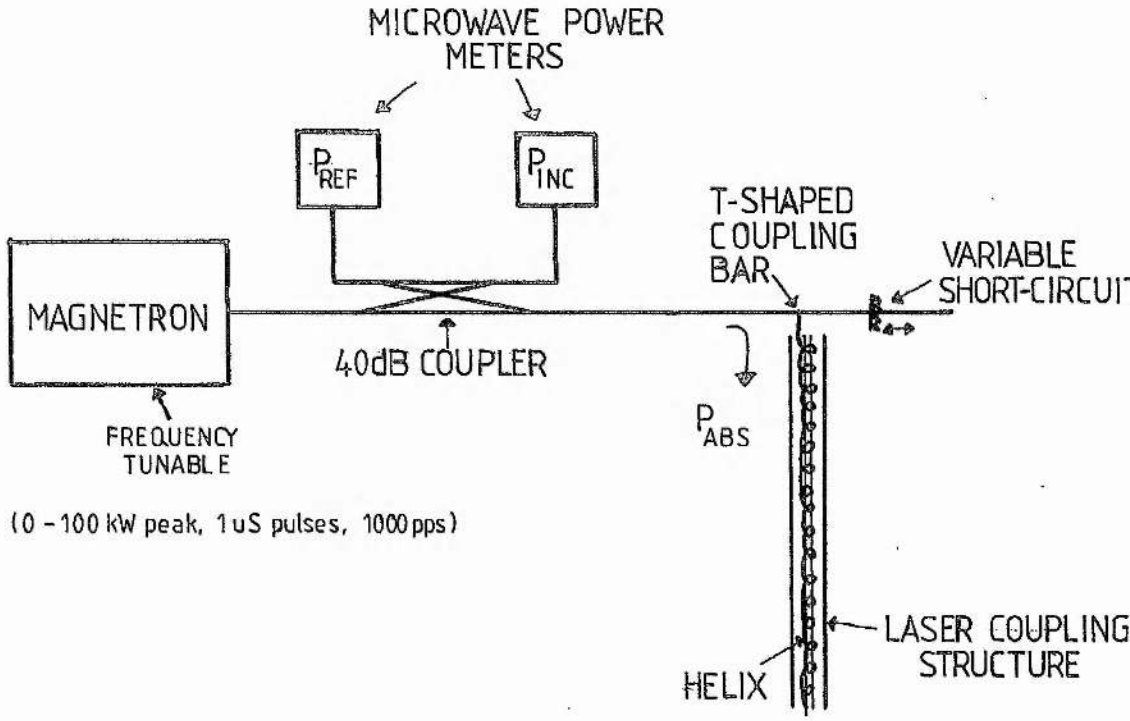


FIGURE 4.16 MICROWAVE APPARATUS USED TO MEASURE THE POWER ABSORBED BY THE LASER COUPLING STRUCTURE.

specific frequency. The frequency at which this maximum occurs would be expected to vary with helix pitch. Instead, the frequency distribution observed is that characteristic of oscillations set up in a non-resonant device.

The discharge is found to be brightest for the 2.5 and 32 mm pitch helices. From fig 4.15, the peak in the absorbed power at a pitch of 32 mm could correspond to the best pitch for impedance matching between the coaxial line and the helix. A good match here is required if the power is to enter the coupling structure at all. This pitch is fairly close to the value of 0.05 m predicted by the theory. The peak at 2.5 mm is harder to interpret and a more precise study is required. However, it should be noted that the discharges for both these helices were noticeably brighter than the others and that these results give the dimensions of the best helices for the configuration used here. A helix with a constant pitch of 2.5 mm was chosen for use in the helical laser coupling structure. Some tapered helices were studied, but their performances were found to be no better than the helix with the 2.5 mm constant pitch.

The theoretical analysis presented earlier in this chapter took no account of the gas discharge. The discharge could significantly affect the properties of the helix, leading to the observed difference in the theoretical and measured optimum pitches. In order to include the effect of a discharge, the analysis would have to be extended to include a medium, contained in the laser tube, with the complex permittivity given by eq 2.20.

(ii) Other helix configurations

The experimental arrangement already described, although easy to set up and optimise, had two disadvantages. Firstly, as the theory has

already described, the axial field intensity is reduced due to the presence of the glass tube and outer metallic shield. Secondly, due to the nature of the discharge, microwave power can have great difficulty penetrating the glass-tube/gas-discharge boundary.

A number of other configurations can be used to avoid these problems, and two were briefly examined. Both were based on the arrangements used in TWTs. The first used a helix which was held in a glass tube by three supporting rods as shown on fig 4.8. In this tube, microwave power was coupled to and from the helix via cylindrical antennas connected to the ends of the helix. Normally in a TWT, the tube is under vacuum, but for the laser, a low pressure Argon fill was introduced. The arrangement failed because the gas between the tube and the antennas ionised, thus preventing the power from reaching the helix. As a result, a glow discharge was observed in the vicinity of the input end, but with no propagation of microwave power down the helix.

The second configuration used a helix with a similar pitch, but smaller radius than the helix reported earlier. This helix was contained inside a glass tube. At the input end, the helix was fed out through a gas-tight seal to the coaxial line, and then onto the T-shaped coupling bar in the waveguide. The results from this looked more promising. The discharge was observed to travel down the centre of the helix occasionally, but severe arcing at the input end prevented the proper operation of the device. At high powers this arcing could not be stopped despite the use of high pressure air, and this is a technical difficulty which has yet to be overcome. The helix was made of copper and this was passed out of the tube inside a small length of Kovar tubing [14], as shown on fig 4.17. The gas tight seal was made between the Kovar tube and the glass. Kovar was chosen because it has approximately the same

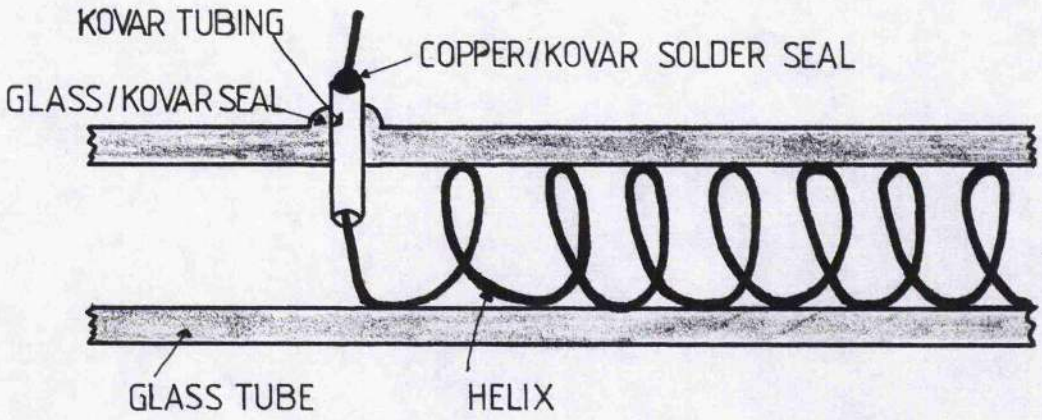


FIGURE 4.17 SEALING TECHNIQUE USED TO INTRODUCE MICROWAVE POWER INTO A HELIX.

thermal expansion coefficient as the glass used. The copper wire of the helix was passed out through the Kovar tube and a solder seal was made at the end. Difficulty was found in making a successful seal at this joint. The wire also became very hot at the input end creating unwanted thermal stress.

The above two experiments were carried out in an attempt to introduce the microwave field directly into the gas discharge so that the field did not have to cross the glass-tube/gas-discharge boundary. These configurations should also have given a larger axial electric field since the helices were in direct contact with the gas. The second arrangement with the helix wrapped around the inside of the tube looked most promising, although there are still some technical difficulties to overcome before it can reach its full potential. Travelling wave tube engineering has reached a high degree of sophistication and some of the technology used here could perhaps be adapted to suit the requirements for powering a laser gas discharge.

**References**

[1] J.R.Pierce
"Traveling Wave Tubes."
Van Nostrand, 1950.

[2] J.F.Gittins
"Power Travelling-Wave Tubes."
English Univ. Press Ltd., 1964.

[3] A.S.Gilmour (Jr)
"Microwave Tubes."
Artech House, 1986.

[4] D.T.Swift-Hook

"Dispersion curves for a helix in a glass tube."

Proc. IEE 105 747 1958.

[5] M.P.Sinha

"Operational characteristics of helical structure over dielectric tube in a metal casing."

J. Inst. Electronics & Telecom. Engrs. 29 554 1983.

[6] K.Tsutaki et al.

"Numerical analysis and design for high-performance helix traveling-wave tubes."

IEEE Trans. on Elect. Devices ED-32 1842 1985.

[7] G.W.Buckley & J.Gunson

"Theory and behaviour of helix structures for a high-power pulsed travelling-wave tube."

Proc. IEE 106B 478 1959.

[8] S.F.Paik

"Design formulas for helix dispersion shaping."

IEEE Trans. on Elect. Dev. ED-16 1010 1969.

[9] P.K.Tien

"Traveling-wave tube helix impedance."

Proc. IRE 41 1617 1953.

[10] B.N.Basu

"Equivalent circuit analysis of a dielectric-supported helix in a metal shell."

Int. J. Elect. 47 311 1979.

[11] B.N.Basu et al.

"Optimum design of potentially dispersion-free helical slow-wave circuit of a broad-band TWT."

IEEE Trans. on Microwave Th. & Tech. 32 461 1984.

[12] G.W.C.Mathers & G.S.Kino

"Some properties of a sheath helix with a centre conductor or external shield."

Elect. Res. Lab., Stanford Univ., Stanford, Calif.

Tech. Rep. No.65, June 1953.

[13] I.Park

"Annular microwave discharges."

Unpublished report, Univ. of St.Andrews, Scotland 1985.

[14] J.A.King

"Materials Handbook for Hybrid Electronics."

Artech House, 1988.

## Appendix A

Modified Bessel functions

For $X < 1.4$

$$I_0(X) \simeq 1 + 0.25\,X^2 + 0.015625\,X^4 + \ldots$$

For $X > 1.4$

$$I_0(X) \simeq \frac{e^X}{(2\pi X)^{0.5}} \left[ 1 + \frac{0.125}{X} + \frac{0.0703125}{X^2} + \frac{0.073242}{X^3} + \ldots \right].$$

For $X < 1.4$

$$I_1(X) \simeq 0.5\,X + 0.0625\,X^3 + 0.002604\,X^5 + \ldots$$

For $X > 1.4$

$$I_1(X) \simeq \frac{e^X}{(2\pi X)^{0.5}} \left[ 1 - \frac{0.375}{X} - \frac{0.1171875}{X^2} - \frac{0.102539}{X^3} - \ldots \right].$$

For $X < 0.6$

$$K_0(X) \simeq -[0.5772 + \mathrm{Ln}(X/2)]I_0(X) + 0.25\,X^2 + (3/128)\,X^4 + \ldots$$

For $X > 0.6$

$$K_0(X) \simeq \left[\frac{\pi}{2X}\right]^{0.5} e^{-X} \left[ 1 - \frac{0.125}{X} + \frac{0.0703125}{X^2} - \frac{0.073242}{X^3} + \ldots \right].$$

For $X < 0.8$

$$K_1(X) \simeq [0.5772 + \mathrm{Ln}(X/2)]I_1(X) + 1/X - 0.25\,X - (5/64)\,X^3 + \ldots$$

For $X > 0.8$

$$K_1(X) \simeq \left[\frac{\pi}{2X}\right]^{0.5} e^{-X} \left[ 1 + \frac{0.375}{X} - \frac{0.1171875}{X^2} + \frac{0.102539}{X^3} - \ldots \right].$$

Appendix B

Computer Program to Calculate the Electric Field
Distribution and Impedance of a Free-Standing Helix.

```
10    ! PROGRAM HELIX
20    ! PAUL J. DOBIE.....JUNE 1988.
30    !
40      CLEAR SCREEN
50      PRINT "    PROGRAM TO EVALUATE THE ELECTRIC FIELD"
60      PRINT "DISTRIBUTION AROUND A HELIX AND ITS IMPEDANCE"
70      PRINT ""
80      PRINT ""
90      PRINT "INPUT OPERATING PARAMETERS"
100     INPUT "FREQ = ?",Freq
110     INPUT "A = ?",A
120     INPUT "P = ?",P
130     INPUT "PIN = ?",Pin
140   !
150     Psi=ATN(P/(2*PI*A))
160     W=2*PI*Freq
170     C=3.E+8
180     B0=W/C
190     Ga=B0*A/TAN(Psi)
200     IF Ga>6 THEN GOTO 230
210     PRINT "B0*a*cotPSI =",Ga
220     INPUT "USE GRAPH ON FIG 4.6: Ga = ?",Ga
230     G=Ga/A
240     B=SQR(G^2+B0^2)
250     PRINTER IS 701
260     Freq=Freq/1.E+9
270     PRINT ""
280     PRINT "MICROWAVE FREQUENCY = ";Freq;"GHz."
290     PRINT "HELIX RADIUS = ";A;"M"
300     PRINT "HELIX PITCH = ";P;"M"
310     PRINT "INPUT POWER = ";Pin;"W"
320   !
330   ! CALC. OF AXIAL E-FIELD & CONSTANT
340     Gr=Ga
350     GOSUB I0
360     GOSUB I1
370     GOSUB K0
380     GOSUB K1
390     Fga=(I0/K0)^(-1/3)*((Ga/240)*(I1/I0-I0/I1+K0/K1-K1/K0+4/Ga))^(-1/3)
400     Ez0=SQR((G^4/(8*B0))*Fga^3*Pin)
410     Const=Ez0
420   !
430   ! FIELD COMPONENTS INSIDE HELIX
440     REAL R(0:8)
450     REAL Ez(0:8)
460     REAL Er(0:8)
470     REAL Epsi(0:8)
480   ! CALC. I,K(Ga)
490     Gr=Ga
500     GOSUB I0
510     GOSUB I1
```

```
520     GOSUB K0
530     GOSUB K1
540     I0ga=I0
550     I1ga=I1
560     K0ga=K0
570     K1ga=K1
580   !
590     X=0
600     FOR Rad=0 TO A STEP A/8
610     R(X)=Rad
620     Gr=G*R(X)
630     GOSUB I0
640     GOSUB I1
650     Ez(X)=Const*I0
660     Er(X)=Const*(B/G)*I1
670     Epsi(X)=Const*(I0ga/I1ga)*TAN(Psi)*I1
680     Ez(X)=OROUND(Ez(X)/1.E+3,3)
690     Er(X)=OROUND(Er(X)/1.E+3,3)
700     Epsi(X)=OROUND(Epsi(X)/1.E+3,3)
710     X=X+1
720     NEXT Rad
730     PRINT ""
740     PRINT "  R(X)      Ez(R)      Er/Ez      Epsi/Ez      (kV/m)  :FIELDS INSIDE
750     FOR X=0 TO 8 STEP 1
751     Erex=Er(X)/Ez(X)
752     Erex=OROUND(Erex,3)
753     Epsiez=Epsi(X)/Ez(X)
754     Epsiez=OROUND(Epsiez,3)
760     PRINT R(X),Ez(X),Erex,Epsiez
770     NEXT X
780   !
790   ! FIELD COMPONENTS OUTSIDE HELIX
800     REAL Ezo(0:8)
810     REAL Ero(0:8)
820     REAL Epsio(0:8)
830     X=0
840     FOR Rad=A TO Z=A+A/50 STEP A/8
850     R(X)=Rad
860     Gr=G*R(X)
870     GOSUB I0
880     GOSUB I1
890     GOSUB K0
900     GOSUB K1
910     Ezo(X)=Const*(I0ga/K0ga)*K0
920     Ero(X)=Const*(B/G)*(I0ga/K0ga)*K1
930     Epsio(X)=Const*(I0ga/K1ga)*TAN(Psi)*K1
940     Ezo(X)=OROUND(Ezo(X)/1.E+3,3)
950     Ero(X)=OROUND(Ero(X)/1.E+3,3)
960     Epsio(X)=OROUND(Epsio(X)/1.E+3,3)
970     X=X+1
980     NEXT Rad
990     PRINT ""
1000    PRINT "  R(X)      Ezo(R)     Ero/Ezo    Epsio/Ezo    (kV/m)  :FIELDS OUTSID
1010    FOR X=0 TO 8 STEP 1
1011    Eroezo=Ero(X)/Ezo(X)
1012    Eroezo=OROUND(Eroezo,3)
1013    Epsioezo=Epsio(X)/Ezo(X)
1014    Epsioezo=OROUND(Epsioezo,3)
1020    PRINT R(X),Ezo(X),Eroezo,Epsioezo
1030    NEXT X
1040  !
1050  ! HELIX IMPEDANCE
```

```
1060     Gr=Ga
1070     GOSUB I1
1080     Hpsi=Const*B0/(12Ø*PI*G)*I1
1090     GOSUB K1
1100     Hpsio=-Const*B0/(12Ø*PI*G)*(I0ga/K0ga)*K1
1110     Z=Pin/(2*PI^2*A^2*(Hpsio-Hpsi)^2)
1120     Z=ORGUND(Z,3)
1130     PRINT ""
1140     PRINT "HELIX IMPEDANCE =";Z;"ohms"
1150     PRINT ""
1160     PRINT "**********************************************************************"
1170     PRINTER IS 1
1180     BEEP 2000,.1
1190     STOP
1200        !SUBROUTINES FOR BESSEL FUNCTIONS
1210 I0:    !
1220        IF Gr>1.4 THEN GOTO 1250
1230        I0=1+.25*Gr^2+.015625*Gr^4
1240        RETURN
1250        I0=EXP(Gr)/(SQR(2*PI*Gr))*(1+.125/Gr+.0703125/Gr^2+.073242/Gr^3)
1260        RETURN
1270        !
1280 I1:    !
1290        IF Gr>1.4 THEN GOTO 1320
1300        I1=.5*Gr+.0625*Gr^3+.002604*Gr^5
1310        RETURN
1320        I1=EXP(Gr)/(SQR(2*PI*Gr))*(1-.375/Gr-.1171875/Gr^2-.102539/Gr^3)
1330        RETURN
1340        !
1350 K0:    !
1360        IF Gr>.6 THEN GOTO 1400
1370        GOSUB I0
1380        K0=-(.5772+LOG(Gr/2))*I0+.25*Gr^2+3/128*Gr^4
1390        RETURN
1400        K0=SQR(PI/(2*Gr))*EXP(-Gr)*(1-.125/Gr+.0703125/Gr^2-.073242/Gr^3)
1410        RETURN
1420        !
1430 K1:    !
1440        IF Gr>.8 THEN GOTO 1480
1450        GOSUB I1
1460        K1=(.5772+LOG(Gr/2))*I1+1/Gr-.25*Gr-5/64*Gr^3
1470        RETURN
1480        K1=SQR(PI/(2*Gr))*EXP(-Gr)*(1+.375/Gr-.1171875/Gr^2+.102539/Gr^3)
1490        RETURN
1500        END
```

## Chapter 5 Noble Gas Ion Lasers

This chapter describes the general properties of noble gas ion lasers. The information reported is based on research carried out by various workers and these are referenced where appropriate. The chapter commences with an outline of the development history and applications of noble gas lasers. The properties of the Argon ion and Helium-Krypton ion laser systems are then described.

### History of noble gas ion lasers

The foundation for the invention of the laser was laid in 1917 when Einstein formulated definitions for the rates of absorption, spontaneous emission and stimulated emission of radiation by an atom. In 1955 the first maser was reported [1]. This is similar to a laser but has an output in the microwave region. Three years later a design for a device which would work as a laser was published [2], and in 1960 laser action was observed for the first time from an optically pumped Ruby rod [3]. The first laser using a gas discharge as an active medium followed shortly afterwards with a Helium and Neon gas mixture [4]. This initiated an intensive research effort which quickly led to the discovery of hundreds of laser lines in many gas mixtures. The Argon ion laser was first discovered in 1964 almost simultaneously by [5] and [6]. This laser system was found to be particularly useful due to its high power output at useful visible wavelengths, and was put into commercial production in 1966. From this point on the Argon ion laser was refined and understanding of the system rapidly grew. As a natural progression

from this work, Krypton and Xenon ion lasers were also developed, but these found fewer commercial applications due to their lower output power.

The Argon ion laser is the most efficient and powerful of all the noble gas ion lasers, with output powers of up to 100 W CW, or 10 kW pulsed, in the blue-green region of the spectrum. As shown on fig 5.1 [7], the two primary outputs are at 488.0 nm (blue) and 514.5 nm (green), and additional lines can be found between 457.9 nm and 514.5 nm. Using ultra-violet optics, a smaller output at 351.1 nm and 363.8 nm can be achieved and outputs in the infra-red are also possible. The Krypton ion laser is technically more demanding but gives both a blue-green output and a strong red output at 647.1 nm and 676.4 nm. This laser has the advantage of covering a much wider range of the visible spectrum, as well as outputs in the ultra-violet and infra-red. Although laser action has also been observed in Xenon [8]-[10], the performance of this laser was never good enough to warrant commercial development.

After the initial discovery of noble gas ion lasers, their performance was investigated as a function of parameters like tube diameter, gas pressure and operating voltage. Spectroscopic and electron energy and density studies were then carried out to investigate the excitation processes [11]-[19], and interaction cross-section data were collected [20]-[23] in order to calculate reaction rates and model the laser discharges.

The large current densities required to excite noble gas ion lasers initiated the search for suitable laser tubes which could withstand the high operating temperatures and the effects of ion bombardment for the full operational lifetime of the laser. The tube

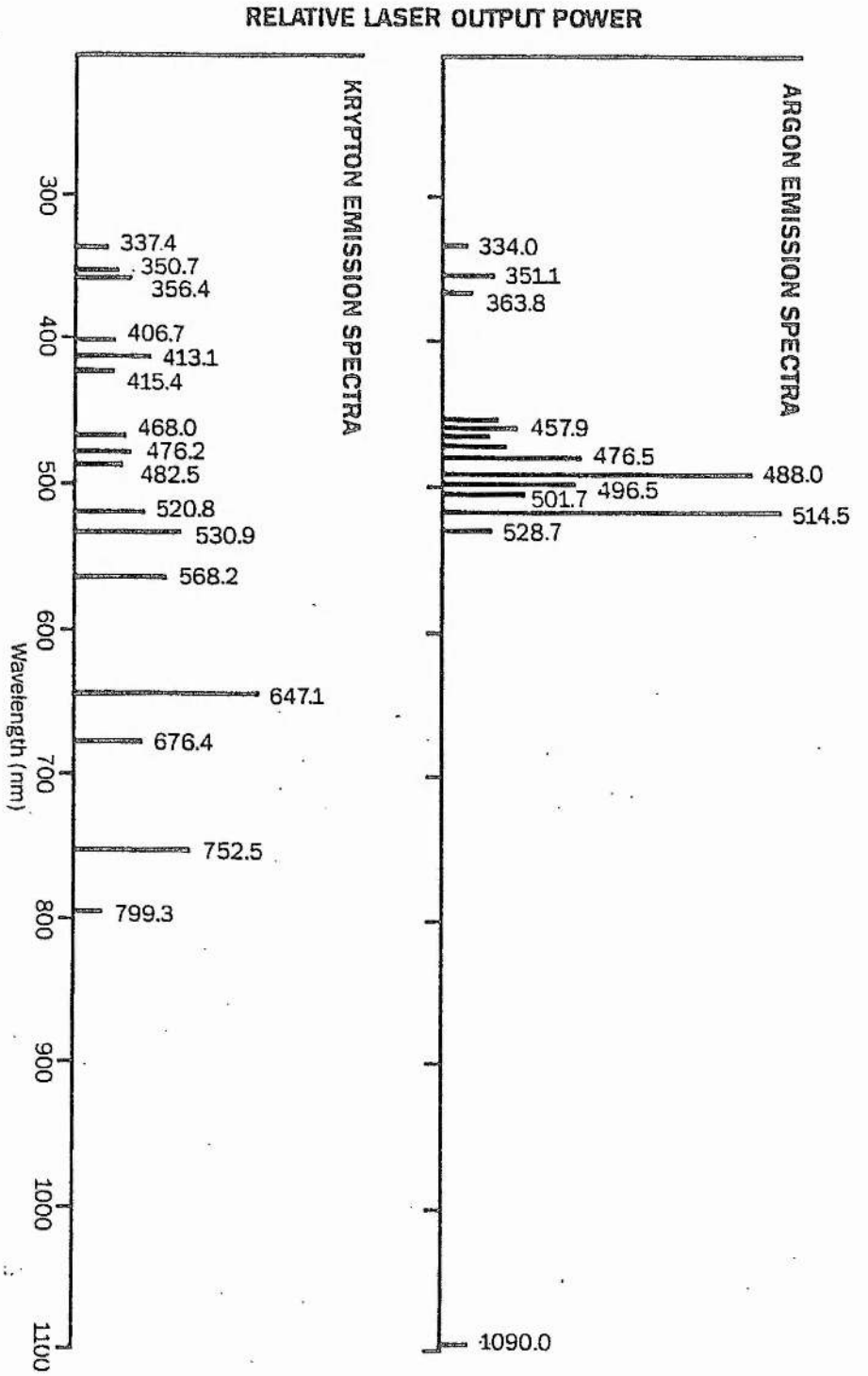


FIGURE 5.1 EMISSION SPECTRA OF THE ARGON ION AND KRYPTON ION LASERS. (From Spectra-Physics 1986, [7]).

material must have a high thermal conductivity so that thermal energy can be easily removed from the discharge region. Initially quartz was used and this was superseded by ceramic and metal segment arrangements [24]-[27]. Currently, low power Argon ion lasers use Beryllium-Oxide capillaries and high power lasers use a segmented arrangement with tungsten/copper discs braized onto an outer ceramic tube. Tungsten is used for its exceptional resistance to sputtering which can be a common reason for tube failure, and copper and beryllium-oxide are used for their high thermal conductivity and purity. These structures can withstand very high operating currents, but commercial models are run at more conservative currents to extend the tube life. Low power lasers generally use narrow bore capillaries with internal diameters of less than 3 mm. Tubes with large internal bores work better for high power lasers [28]-[29].

The Argon ion and Krypton ion lasers give a high power optical beam with a high radiation density, directionality, coherence and monochromaticity. These properties give noble gas ion lasers a whole host of applications in research, material processing, medicine, communications and entertainment. These include dye laser pumping, isotope separation, spectroscopy, optical data storage, platemaking, printing, holography, interferometry, surgery, irradiation, light shows and large screen projection. These applications and others have been dealt with at more length in [30]-[45].

Laser theory is not examined in this thesis but is covered in more detail in [46]-[51].

The Argon ion laser

A considerable amount of research has been carried out on DC-excited Argon ion lasers and a description of the properties of these will now be given. Many of the characteristics of a DC discharge are similar to those of a microwave excited discharge. Therefore, much of what is given here will also apply for a microwave excited laser.

(i) Characteristics of the Argon ion laser

Current densities in high power (5 - 20 W) Argon ion lasers can exceed 500 $A/cm^2$. Current is not easily measured in an electrodeless discharge, but in the high electric fields associated with a high power pulsed microwave signal, such current densities should be readily attained. Conventional lasers operate at an efficiency of 0.01 - 0.1% and the laser tube must thermally dissipate powers which can exceed 100 W/cm of tube length. Lower power CW DC-excited lasers use high thermal conductivity ceramic tubes, heat sinks and forced air cooling, whereas higher power lasers use water cooling and ceramic/metal tubes. Cooling is often less important for pulsed lasers because of the lower duty cycle used. Continuous DC Argon ion lasers operate at a tube voltage of around 300 V and, in a pulsed mode, around 15 kV is used. The internal diameter of the tube in the active region usually lies between 1 mm and 8 mm and electron densities of at least $10^{19}$ $m^{-3}$ are required for optimum laser output. Figure 5.2 shows the typical variation of optimum gas pressure against discharge current for different internal tube diameters [52]. The Argon pressure-tube diameter product is usually a constant and so lasers using a very small tube diameter have a higher operating pressure. Low power lasers use tube bores of less than 3 mm, and high power lasers generally favour larger diameters. The same sort of dependance on tube

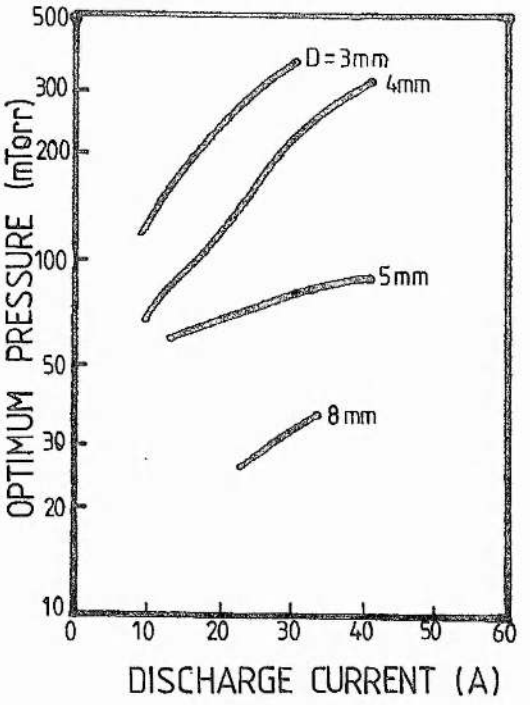


FIGURE 5.2 OPTIMUM GAS PRESSURE FOR MAXIMUM LASER OUTPUT AS A FUNCTION OF DISCHARGE CURRENT FOR VARIOUS CAPILLARY DIAMETERS. (From Bridges 1967, [52]).

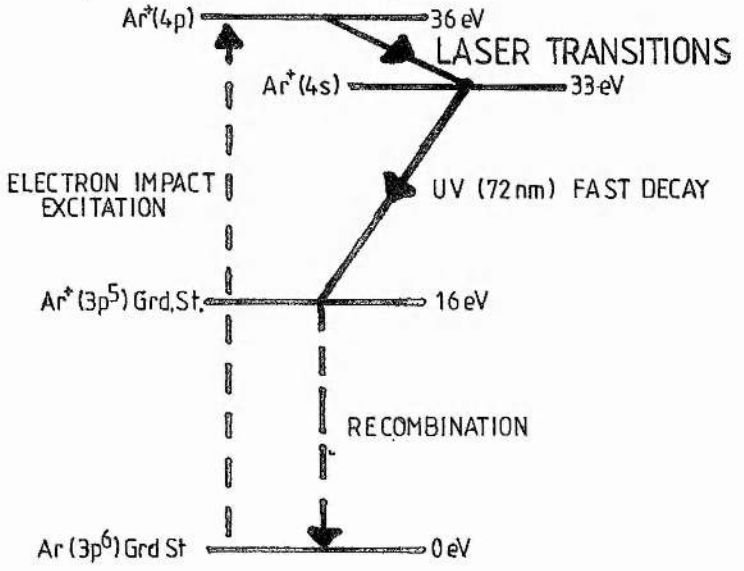


FIGURE 5.3 ENERGY LEVEL DIAGRAM OF THE ARGON ION LASER. (From Bennett 1964, [53]).

diameter can be expected for a microwave system because the electron diffusion process to the tube walls, which helps dictate the best tube diameter, is the same as for the DC-case.

In CW lasers a two-step excitation process populates the upper laser level. Electron collisions firstly ionise and then excite the Argon atoms of the gas. These normally operate at pressures around 0.5 mB. Pulsed ion lasers operate at pressures which are about an order of magnitude lower than for the CW case and a single-step excitation process operates.

The Argon ion laser oscillates in the visible at between 454.5 nm and 528.7 nm and all lines come from the singly ionised 4p - 4s transitions. The three most prominent lines are at 476.5 nm, 488.0 nm and 514.5 nm. These originate from the $(^3P)4p^2P^\circ_{3/2} \rightarrow (^3P)4s^2P_{1/2}$, $(^3P)4p^2D^\circ_{5/2} \rightarrow (^3P)4s^2P_{3/2}$ and $(^3P)4p^4D^\circ_{5/2} \rightarrow (^3P)4s^2P_{3/2}$ transitions, respectively. Energy level diagrams showing these optical transitions are given in figs 5.3 and 5.4 [53]-[54]. In the ultra-violet, the Argon ion laser oscillates at wavelengths between 291.3 nm and 363.8 nm. The main lines occur at 351.1 nm and 363.8 nm and originate from the doubly ionised $(^4S^o)4p^3P_2 \rightarrow (^4S^o)4s^3S_1$ and $(^4D^o)4p^1F_3 \rightarrow (^2D^o)4s^1D_2$ transitions. Emission in the infra-red occurs at 1.09 um from the $(^3P)4p^2P^\circ_{3/2} \rightarrow (^3P)3d^2D_{5/2}$ transition.

The unsaturated gain of the transitions in an Argon ion laser discharge depend, to a certain extent, upon the system being used. Nevertheless, the unsaturated gain in CW Argon ion lasers is normally largest for the 488.0 nm and 514.5 nm lines, and in pulsed systems, the 476.5 nm line can be very prominent. The most prominent lines have an unsaturated gain of up to 6 dB/m. The gain of an ion laser medium

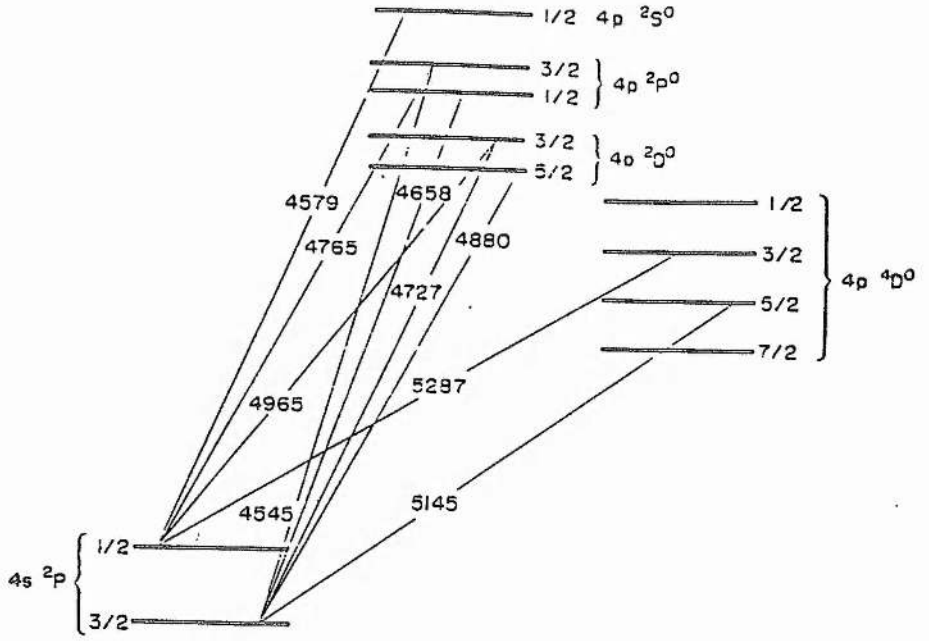


FIGURE 5.4 ENERGY LEVEL DIAGRAM OF THE ARGON ION LASER SHOWING THE MAIN LASER LINES FROM THE 4p - 4s TRANSITIONS. (From Cherrington 1979, [54]).

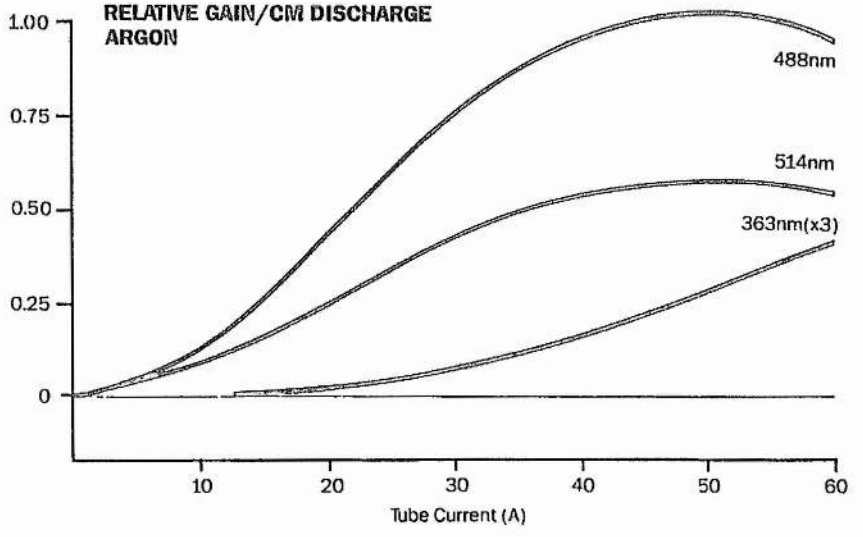


FIGURE 5.5 GAIN SATURATION OF AN ARGON ION LASER DISCHARGE. (From Spectra-Physics 1986, [7]).

generally increases with increasing current density up to some maximum value, followed by a decline as shown on fig 5.5. The decline is principally due to the pumping of higher lying ionic states at the expense of the singly ionised visible laser states. The unsaturated and saturated gain coefficients are independent of the nature of the exciting electric field and so this behaviour also applies for microwave excitation.

The addition of Helium to an Argon ion laser discharge, and the application of a longitudinal magnetic field can both enhance the output of an Argon ion laser [55]-[60]. The presence of Helium can increase the electron temperature of the laser discharge, thus improving the efficiency of the upper laser level population process and so increasing output. This effect is observed in the microwave excited laser reported in the next chapter. Helium can also act as a buffer gas improving discharge stability and breakdown consistency, and lowering the breakdown field. A magnetic field has the effect of reducing diffusion losses to the tube wall, thus increasing the electron density and temperature in the active region at the tube centre. An enhancement of power output of up to a factor of 5 can be achieved with a magnetic field. As shown by fig 5.6, the optimum magnetic field is between 1000 and 2000 gauss depending upon the gas pressure. The optimum magnetic field for a particular transition also depends upon the current density and decreases as the tube diameter is increased.

Ion lasers actually consume gas as ions are driven into the walls of the tube. Commercial lasers use either a ballast system with a volume much greater than that of the active region, or a pressurised

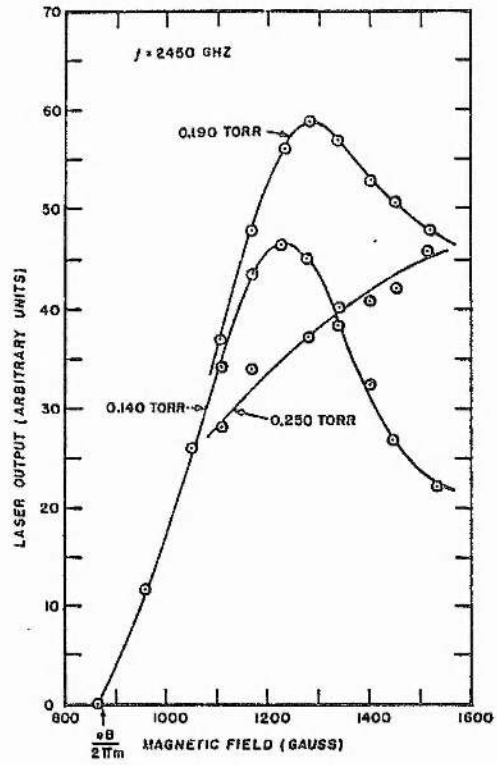


FIGURE 5.6 DEPENDENCE OF LASER OUTPUT ON MAGNETIC FIELD AND ARGON PRESSURE. (From Goldsborough 1966, [60]).

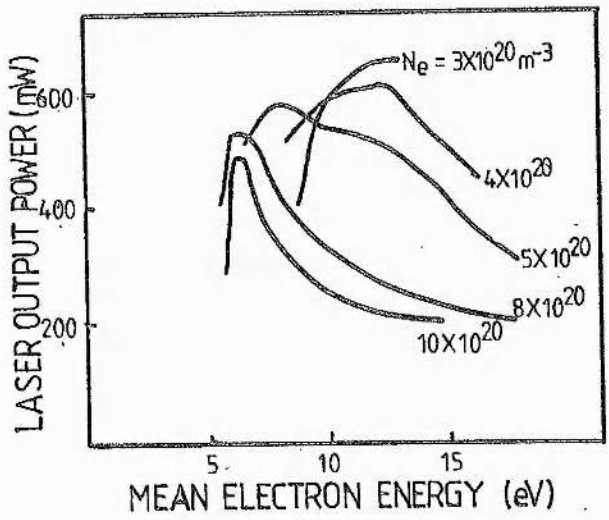


FIGURE 5.7 DEPENDENCE OF LASER OUTPUT POWER ON MEAN ELECTRON ENERGY WITH ELECTRON DENSITY AS A PARAMETER. (From Sakharov 1975, [18]).

container connected to the tube via an automatic filling valve and pressure sensitive controller. These help to maintain the optimum gas pressure throughout the life of a tube. In DC excited lasers, a pressure gradient can build up during operation due to the pumping of gas to the anode. This affects performance, and to combat this, some form of gas return path is usually provided. This can take the form of an external gas return tube, or in the case of a segmented tube, additional holes around the central bore [7]. Such pressure gradients are not a problem when using microwave excitation due to the oscillating nature of the field.

Commercial lasers give multi-line outputs from 5 mW to greater than 20 W CW. Low power Argon ion lasers have lifetimes which can exceed 10000 hours; whilst the higher powered versions last upwards of 1000 hours. Often laser tubes can be re-conditioned and this is particularly important for high power lasers which use very expensive tubes. The tube of a microwave excited laser can be made to a simpler design due to the lower stress imposed upon it as a result of the oscillating nature of the microwave electric field. Similarly the lifetime of such a tube should be favourable.

(ii) The Argon ion laser discharge

As can be seen from fig 5.3, the upper level of the Argon ion laser has an energy of 36 eV. In order to excite ions to this energy, the laser discharge must be very energetic. The upper laser levels are populated when atoms are excited by electron collisions. Because electrons play the dominant role in the excitation processes, the state of the electron population is very important. The parameters of most interest in a noble gas ion laser discharge are the electron energy,

the electron density, the electric field and the collision frequency.

The electron density and mean electron energy (equivalent to electron temperature) are inter-related and, as shown on figs 5.7 and 5.8, have a pronounced effect on the output of an Argon ion laser. The electron density in an ion laser discharge lies between $10^{19}$ and $10^{21}$ $m^{-3}$ [61]-[67]. It is dictated, to a large extent, by the size of the applied electric field. The mean electron energy dictates the amount of ionisation occurring in a discharge, and the electron production rate affects the electron density. Large numbers of high energy electrons are required to excite the upper laser levels, and so a high electron energy is required. The electron energy distribution function in an Argon ion laser discharge may be regarded here as Maxwellian, and only a small percentage of the electron population attains the high energies required for excitation. The mean electron energy is actually quite small and it is electrons in the tail of the distribution which excite the upper laser levels. The optimum mean electron energy depends on the electron density, and as can be seen from fig 5.7, the optimum electron energy is highest for the lower electron densities. As the electron density is increased, the optimum electron energy decreases. The optimum mean electron energy for an Argon ion laser is approximately 6 eV [65],[70], but this value relies upon the electron densities being attained in the discharge. High power lasers generally have a larger mean electron energy than lower power versions. As has been explained in chapter 2, the high energy tail of the electron energy distribution function is liable to be enhanced when microwave frequencies are used. Such an effect is beneficial in the excitation of the upper laser levels.

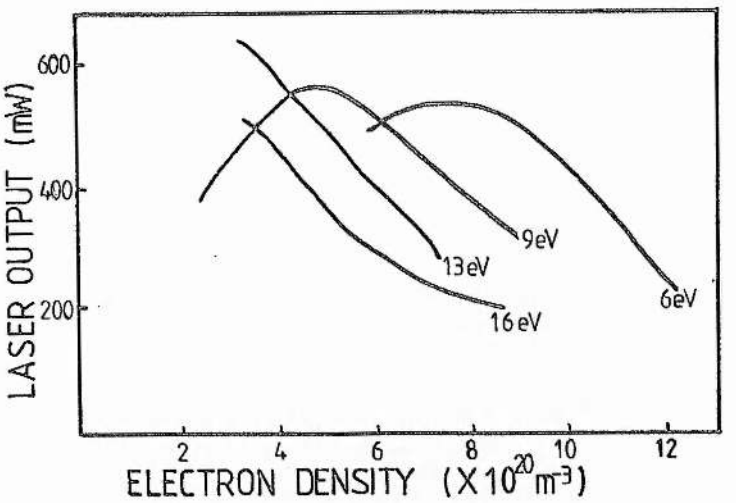


FIGURE 5.8 DEPENDENCE OF LASER OUTPUT POWER ON ELECTRON DENSITY WITH MEAN ELECTRON TEMPERATURE AS A PARAMETER. (From Sakharov 1975, [18]).

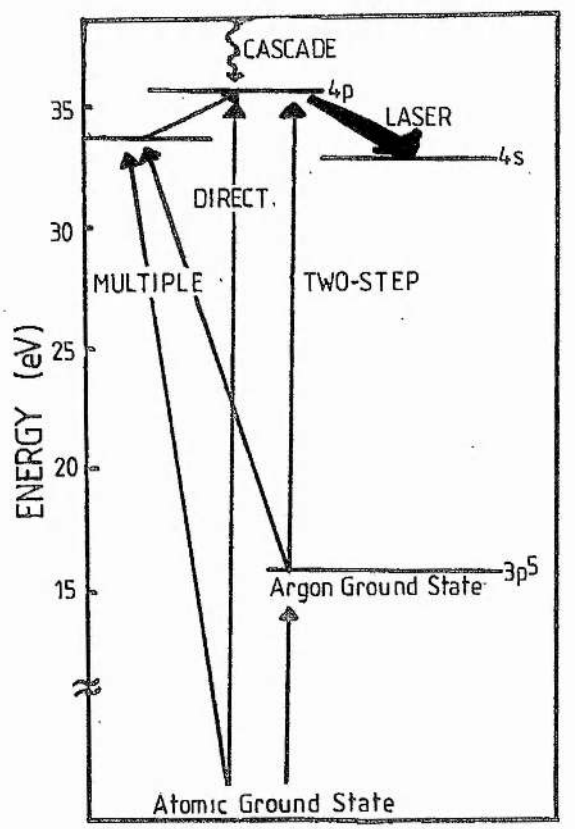


FIGURE 5.9 EXCITATION PROCESSES IN AN ARGON ION LASER DISCHARGE. (Not to scale).

The other discharge parameter of importance, the collision frequency, is dictated by gas pressure. The collision frequency influences the nature of the collisional processes in a discharge. If the collision frequency is high (high gas pressure), the energy gained from the accelerating field between collisions is low, and the degree of excitation is limited. When the collision frequency is low, high energy interactions are more likely to occur leading to ionisation. This is why CW Argon ion lasers, which usually use two-step excitation, operate at higher pressures than pulsed lasers which use single-step excitation. At the optimum collision frequency, dictated by an optimum gas pressure, the mean energy gained between collisions gives energy transfers which lead to the most efficient excitation of the upper laser level. In the next chapter it is shown that single-step excitation predominates in the pulsed microwave excited laser prototypes. This behaviour is the same as that usually observed for pulsed DC-excited ion lasers.

(iii) Excitation mechanisms

There are a number of possible excitation pathways used to populate the upper levels of the Argon ion laser. The major routes are shown on fig 5.9. Here, the excitation processes are described and the use of spectroscopy as an investigative tool is considered.

Before describing the excitation processes in more detail, it is worth considering the upper and lower laser levels themselves. A selective upper laser level population mechanism, and a favourable lifetime ratio between the upper and lower laser levels are both desirable for efficient laser operation. Favourable lifetime ratios exist for the Argon ion laser. The upper and lower levels of the 488.0

nm transition have lifetimes of 9.57 nS and 1.81 nS respectively, and for the 514.5 nm transition, 7.30 nS and 1.81 nS, [20]-[23]. A similar situation exists for the other laser transitions of fig 5.4. With the exception of the 496.5 nm and 514.5 nm lines, the 4p upper states cannot decay directly to the ion ground state because of parity rules, but instead, must decay principally via the lower laser states. A selective population mechanism is not therefore critical.

The single-step excitation process requires energetic electrons and is prevalent in low pressure ($\sim$0.05 mB), pulsed ion laser discharges. A high electric field is required to impart sufficient energy to electrons in the discharge within the duration of the pulse. The required E/p ratio, where E is the electric field and p is the gas pressure, is in excess of 100 kV/m-mB. As shown in chapter 2, such values are easily attained using microwave sources. The excitation reaction can be written as [12]-[16],

$$Ar\ (3p^6) + e^- \rightarrow Ar^{+'}\ (3p^4(^3P)4p) + 2e^- , \qquad (5.1)$$

where Ar $(3p^6)$ is the neutral atom ground state and $Ar^{+'}$ $(3p^4(^3P)4p)$ is the excited upper laser level.

In pulsed Argon ion lasers the upper laser level can also be populated by cascade excitation. In some cases cascade excitation can contribute to as much as 50% of the upper state population [69]. The amount of cascade excitation occurring can be found by summing the spontaneous emission intensities of all lines terminating at a specified upper laser level. This is then compared with the sum of the intensities of lines emanating from this level. This can be represented by the continuity equation,

$$\Sigma_i\ A_{i2}\ N_i\ +\ P_2\ =\ \Sigma_k\ A_{2k}\ N_2\ . \qquad (5.2)$$

Here, $A_{ik}$ are the Einstein spontaneous emission coefficients and $N_i$ are the numbers of atoms in state i. The summation on the left hand side represents all the transitions from states i down to the upper laser level, where the upper laser level is designated by 2. The pump rate due to all other population mechanisms from below is represented by $P_2$. The right hand side gives all the de-excitation routes from the upper laser level. The transitions due to cascade excitation and de-excitation of the 488.0 nm and 476.5 nm lines are tabulated on figs 5.10 and 5.11 [70]. These transitions can be used to evaluate the percentage of cascade excitation. Observations made of the microwave excited laser discharges in the next chapter indicate that cascade excitation is negligible for the prototypes under study. This is typical of a low energy Argon ion laser discharge.

The two-step excitation process is most common in CW ion lasers. Here, electron collisions excite ground state Argon atoms to the singly ionised ground state given by [12]-[16],

$$Ar\ (3p^6) + e^- \rightarrow Ar^+\ (3p^5) + 2e^- \ . \qquad (5.3)$$

The process is then completed by another collision giving,

$$Ar^+\ (3p^5) + e^- \rightarrow Ar^{+'}\ (3p^4(^3P)4p) + e^- \ . \qquad (5.4)$$

Here, a higher collision frequency is required than for the pulsed case, and the optimum gas pressure is around 0.5 mB. Apart from two-step excitation, other multi-step processes can occur via singly ionised metastable states [71].

The effects of cascade excitation are easily quantified simply by measuring the intensities of lines due to transitions down to the upper laser level. Population by direct and two-step excitation are harder to quantify. For these, the best indication is given by considering

| λ(nm) | TRANSITION | INTENSITY |
|---|---|---|
| 734.85 | $3d'^{2}D_{5/2}$ | 7 |
| 709.06 | $3d'^{2}D_{3/2}$ | 1 |
| 637.59 | $3d'^{2}P_{3/2}$ | 3 |
| 479.21 | $3d''^{2}D_{5/2}$ | 6 |
| 437.25 | $3s^{4}P_{5/2}$ | 5 |
| 425.56 | $5s^{4}P_{3/2}$ | 4 |
| 410.39 | $5s^{2}P_{3/2}$ | 20 |
| 400.76 | $4d^{4}D_{7/2}$ | 2 |
| 398.82 | $4d^{4}D_{5/2}$ | 9 |
| 395.84 | $4d^{4}D_{3/2}$ | 6 |
| 371.72 | $4d^{4}F_{7/2}$ | 10 |
| 365.61 | $4d^{4}F_{5/2}$ | 10 |
| 362.01 | $4d^{4}F_{3/2}$ | 3 |
| 360.39 | $4d^{4}P_{3/2}$ | 4 |
| 355.95 | $4d^{2}F_{7/2}$ | 25 |

**FIGURE 5.10a** LEVELS CASCADING INTO THE SINGLY IONISED ARGON $4p^{2}D^{o}_{5/2}$ STATE.
(From Striganov, 1968 [70]).

| λ(nm) | TRANSITION | INTENSITY |
|---|---|---|
| 1046.72 | $3d^2F_{7/2}$ | 20 |
| 1011.07 | $4s'^2D_{5/2}$ | 3 |
| 921.04 | $3d^4P_{5/2}$ | 1 |
| 890.45 | $3d^4P_{3/2}$ | 2 |
| 765.40 | $3d^2P_{3/2}$ | 2 |
| 650.91 | $3d^4F_{3/2}$ | 6 |
| 639.92 | $3d^4F_{5/2}$ | 15 |
| 624.31 | $3d^4F_{7/2}$ | 25 |
| 487.99 | $4s^2P_{3/2}$ | 30 |
| 422.82 | $4s^2P_{3/2}$ | 20 |
| 408.24 | $4s^2P_{5/2}$ | 15 |
| 383.04 | $3d^4D_{3/2}$ | 10 |
| 380.86 | $3d^4D_{5/2}$ | 11 |
| 378.64 | $3d^4D_{7/2}$ | 12 |

FIGURE 5.10b LEVELS DE-EXCITING FROM THE SINGLY IONISED ARGON $4p^2D^o_{5/2}$ STATE.
(From Striganov, 1968 [70]).

| λ(nm) | TRANSITION | INTENSITY |
|---|---|---|
| 705.50 | $3d'^{2}P_{3/2}$ | 3 |
| 516.58 | $3d''^{2}D_{5/2}$ | 8 |
| 468.15 | $5s^{2}P_{5/2}$ | 2 |
| 454.78 | $5s^{2}P_{3/2}$ | 4 |
| 440.17 | $5s^{4}P_{1/2}$ | 2 |
| 437.49 | $5s^{2}P_{3/2}$ | 6 |
| 424.36 | $4d^{4}D_{5/2}$ | 2 |
| 422.26 | $5s^{2}P_{1/2}$ | 10 |
| 420.99 | $4d^{4}D_{3/2}$ | 1 |
| 386.96 | $4d^{4}F_{5/2}$ | 2 |
| 385.52 | $4d^{4}P_{1/2}$ | 4 |
| 384.54 | $4s^{4}P_{5/2}$ | 10 |
| 383.02 | $4d^{4}F_{3/2}$ | 1 |
| 381.12 | $4d^{4}P_{3/2}$ | 2 |
| 375.10 | $4d^{4}P_{5/2}$ | 2 |
| 365.53 | $4d^{2}F_{5/2}$ | 12 |

FIGURE 5.11a LEVELS CASCADING INTO THE SINGLY IONISED ARGON $4p^{2}P^{o}_{3/2}$ STATE.
(From Striganov, 1968 [70]).

| λ (nm) | TRANSITION | INTENSITY |
|---|---|---|
| 1092.34 | $3d\,^2D_{5/2}$ | 7 |
| 990.64 | $4d\,^2F_{5/2}$ | 5 |
| 877.19 | $4s'\,^2D_{5/2}$ | 15 |
| 860.40 | $4s'\,^2D_{3/2}$ | 6 |
| 784.94 | $3d\,^4P_{3/2}$ | 3 |
| 768.35 | $3d\,^4P_{1/2}$ | 1 |
| 686.13 | $3d\,^2P_{3/2}$ | 15 |
| 643.76 | $3d\,^2P_{1/2}$ | 8 |
| 476.49 | $4s\,^2P_{1/2}$ | 25 |
| 454.50 | $4s\,^2P_{3/2}$ | 25 |
| 405.77 | $4s\,^2P_{1/2}$ | 1 |
| 397.45 | $4s\,^4P_{3/2}$ | 10 |
| 362.10 | $3d\,^4D_{3/2}$ | 3 |
| 360.15 | $3d\,^4D_{5/2}$ | 4 |

**FIGURE 5.11b** LEVELS DE-EXCITING FROM THE SINGLY IONISED ARGON $4p\,^2P^o_{3/2}$ STATE.
(From Striganov, 1968 [70]).

the degree of excitation occurring to the laser states themselves and other states of similar energies. For example, if the pump power is low, the bulk of the excitation will occur to states below the laser level. And, if the pump power is very high, states above the laser levels will be excited more efficiently. Multiple-step excitation can be studied by considering the population rates into metastables and other important states involved in the excitation pathway. These excitation routes can be examined in more detail using tables of spectral lines and energy level diagrams [70]-[72].

The lasers reported in this thesis operate in a pulsed mode where 1 uS microwave pulses are used to pump the laser medium. The pulsed Argon ion laser usually operates with an E/p ratio of around 100kV/m-mB and a single-step excitation mechanism predominates. The discharge structures reported in chapters 3 and 4 produce a field giving an E/p ratio of up to 400 kV/m-mB. With such fields, excitation is certainly single-step. However, as reported in chapter 2, the field may be significantly reduced because the microwave field has difficulty penetrating the discharge boundary. Taking this into account, E/p in the gas reaches an estimated 4 kV/m-mB. This is still significantly above that used in a CW Argon ion laser which uses multi-step excitation. The high E/p values present here generally result in single-step excitation.

So far it has been assumed that the lower laser level always de-excites quickly, thus maintaining the population inversion. However a process can occur, particularly in pulsed lasers, called radiation trapping [73]-[74]. This prevents the de-population of the lower laser level and reduces the population inversion, thus impairing the

output power. Radiation trapping occurs most often in high power Argon ion lasers and can be neglected for the low power lasers reported here.

## The Helium-Krypton ion laser

The Argon ion laser described in the previous section uses electron-impact excitation. Another regime can be created when a Helium-Krypton gas mixture is used. Here, the upper laser levels are populated by resonant transfer of energy between high potential energy Helium metastables and Krypton ions in their ground state. This regime will now be discussed.

### (i) Characteristics of the Helium-Krypton ion laser

The Helium-Krypton ion laser emits principally at 469.4 nm and operates in the afterglow of a pulsed discharge. The research which has been carried out to study this type of laser is much more limited than that for the Argon ion laser. Microwave excitation of the Helium-Krypton ion laser is reported in [58],[66]-[67] and [75]-[76]. These papers, (all written by Kato et al.), describe a laser which uses a 4-20 kW, 9 GHz microwave source producing 0.5 - 4 uS pulses at 200 pps. The use of tubes with an internal diameter of 2.5 - 8.2 mm is reported, and the highest output is obtained using a 4.5 mm tube and a 20 kW peak pump power. The characteristics of the output depend upon the input power and a 2.5 mm tube is found best when using a low input power of 4 kW. The optimum Helium and Krypton pressures are found to be around 15 mB, and 0.06 mB respectively. The optimum pressure is seen to increase with increasing input power. The optimum mixture ratio (= $P_{He}/P_{Kr}$) is around 250, but this is found to increase with increasing tube

diameter. Unlike Argon and Krypton ion lasers, the gas pressure-tube diameter product is not constant. The output power is found to be almost independent of the input pulse length for pulses between 0.5 and 4 uS in length.

As shown on fig 5.12, the upper laser level is excited by resonant transfer of energy from Helium metastables to Krypton ions. A higher efficiency is possible here compared with the Krypton ion laser because the electron temperature is less than is required for pure Krypton. This is because electron-impact excitation is only required to excite Helium metastables, whereas in pure Krypton, atoms must be ionised and then excited. The laser radiation appears 1 - 2 uS after the exciting microwave pulse has stopped. The peak of the laser pulse occurs 1 - 2 uS after this and lasts a total of up to 5 uS. Saturation of the output is observed as the input power is increased.

(ii) The Helium-Krypton ion laser discharge

Argon and Krypton ion laser discharges require high electron temperatures in order to ionise and excite the atoms to the upper laser levels. Because the Helium-Krypton laser uses resonant transfer excitation, the electron temperature does not have to be as high. In this laser, a high electron density is more important so that a high amount of Helium metastable excitation is achieved. During the microwave pulse an electron density in the region of $10^{21}$ $m^{-3}$ is achieved in the Helium-Krypton gas mixture. Helium ionisation can be considered negligible because it has a high ionisation energy compared with Krypton.

As soon as the microwave pulse has finished, the electron density begins to drop due to recombination and, as shown on fig 5.13, the

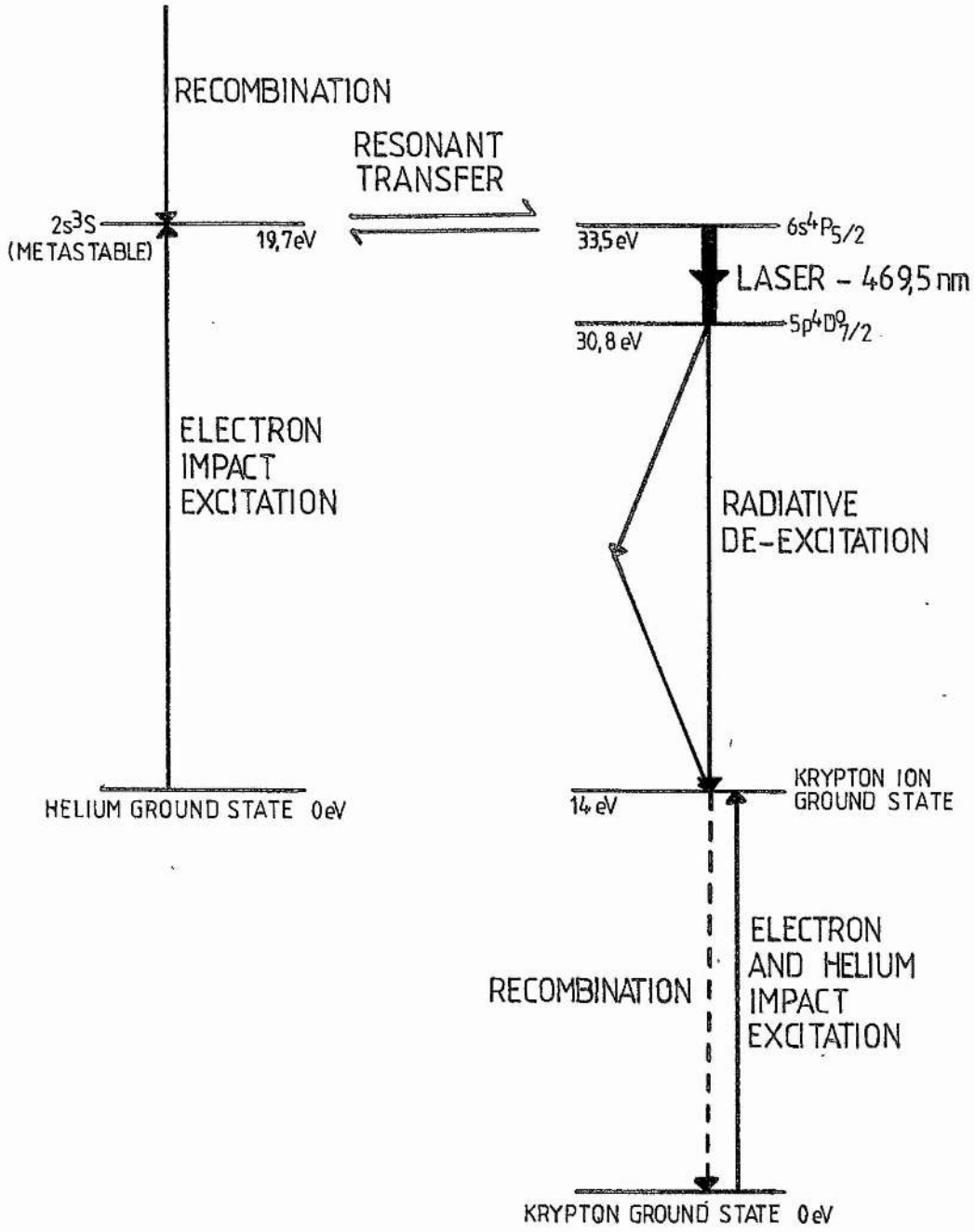


FIGURE 5.12 ENERGY LEVEL DIAGRAM OF THE HELIUM–KRYPTON ION LASER. (Not to scale).

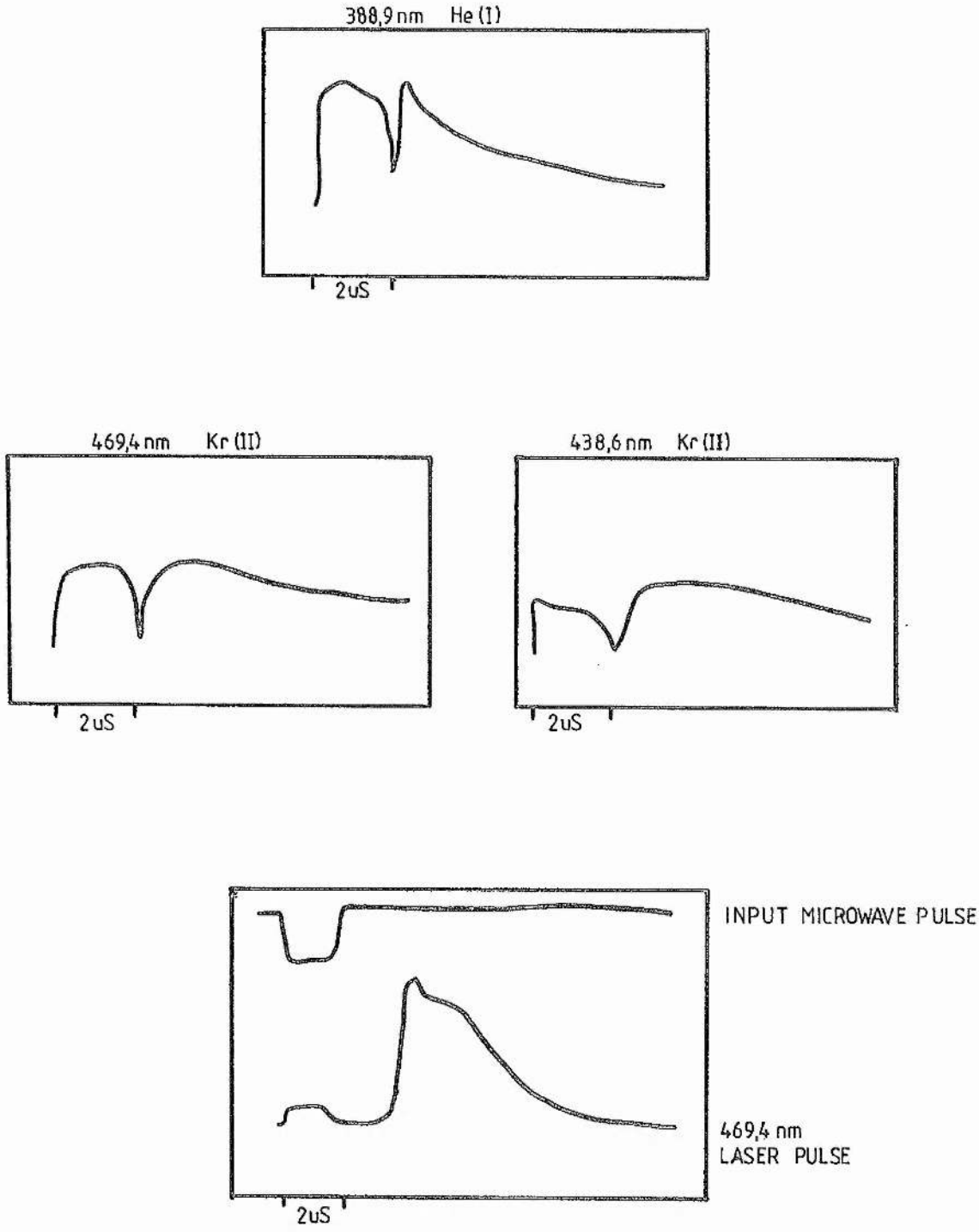


FIGURE 5.13 TIME-RESOLVED SIDE-LIGHT FROM A HELIUM-KRYPTON ION LASER DISCHARGE AND THE RESULTING LASER OUTPUT PULSE. (From Kato et al. 1975, 1977 [66], [76]).

atomic Helium intensities are observed to rapidly fall. After this, the intensities of the transitions associated with the Helium metastable states quickly climb again to a maximum value which is attained 1 - 2 uS after the end of the microwave pulse. The intensities of the transitions then gradually decline. The Krypton transitions which are excited by resonant transfer also exhibit an afterglow enhancement, and it is from these lines that laser action is expected.

(iii) Excitation mechanisms and spectroscopy

The 438.6 nm and 469.4 nm Krypton ion lines emit strongly in the afterglow of the Helium-Krypton ion laser discharge. These lines are due to the $6s^4P_{5/2} \rightarrow 5p^4P^\circ_{3/2}$ and $6s^4P_{5/2} \rightarrow 5p^4D^\circ_{7/2}$ transitions, respectively. The energies of the upper state of these transitions, as measured from the ionic ground state, closely coincide with that of the Helium $2s^3S$ metastable state. No afterglow radiation is observed from the 438.6 nm and 469.4 nm transitions in a pure Krypton discharge. Resonant transfer excitation therefore occurs between the $He^*$ $(2s^3S)$ metastable state atoms and $Kr^+$ ground state ions. This can be written as,

$$He^* (2s^3S) + Kr^+ \rightarrow Kr^{+'} (6s^4P_{5/2}) + He \ . \qquad (5.5)$$

The Krypton ions are created by the following process,

$$He^* (2s^3S) + Kr \rightarrow He + Kr^+ + e^- \ . \qquad (5.6)$$

Another way in which ionisation of Krypton takes place is,

$$\begin{aligned} He^* + He^* &\rightarrow He + He^+ + e^- \ , \\ He^+ + Kr &\rightarrow He + Kr^+ \ , \end{aligned} \qquad (5.7)$$

where $He^*$ represents Helium metastable states. Excitation process 5.7 is not as likely to occur as 5.6 because the latter is simpler and has

components of a lower energy.

It can be seen that Helium metastables play the dominant role in the excitation process. The cascade processes $3p^3P_{2,1,0} \rightarrow 2s^3S$ and $3p^1P_1 \rightarrow 2s^1S$ emit at 388.9 nm and 501.6 nm respectively, and the time variation and strengths of these transitions gives an indication of the $2s^3S$ and $2s^1S$ metastable populations. The $2s^3S$ metastable population is observed to be larger than the $2s^1S$ metastable population by up to a factor of 8 [58]. The metastables are populated by single and multi-step electron-impact excitation processes, and indirectly via cascade excitation. Figure 5.13 shows the time variation of the $2s^3S$ Helium metastable population and the resulting Krypton spontaneous and laser emission.

References

[1] J.P.Gordon et al.
"The maser - new type of microwave amplifier, frequency standard, and spectrometer."
Phys. Rev. 99 1264 1955.

[2] A.L.Schawlow & C.H.Townes
"Infrared and optical masers."
Phys. Rev. 112 1940 1958.

[3] T.H.Maiman
"Stimulated optical radiation in Ruby."
Nature 187 493 1960.

[4] A.Javan et al.
"Population inversion and continuous optical maser oscillation in a gas discharge containing a He-Ne mixture."
Phys. Rev. Letts. 6 106 1961.

[5] W.B.Bridges
"Laser oscillation in singly ionised Argon in the visible spectrum."
Appl. Phys. Letts. 4 128 1964.

[6] G. Convert et al.
"Visible laser transitions in ionised Argon."
C.R.Acad. Sci. 258 4467 1964.

[7] "Model 2020 Ion Laser."
Spectra-Physics Inc., 1986.

[8] W.W.Simmons & R.S.Witte
"High power pulsed Xenon ion lasers."
IEEE J. Qu. Elect. QE-6 466 1970.

[9] D.T.Hodges & O.L.Tang
"New CW ion laser transitions in Argon, Krypton and Xenon."
IEEE J. Qu. Elect. QE-6 757 1970.

[10] J.P.Goldsborough & A.L.Bloom
"New CW ion laser oscillating in microwave-excited Xenon."
IEEE J. Qu. Elect. QE-3 96 1967.

[11] A. Chutjian & D.C.Cartwright
"Electron-impact excitation of electronic states in argon at incident energies between 16 and 100 eV."
Phys. Rev. A 23 2178 1981.

[12] B. van der Sijde

"Excitation mechanisms in the Argon ion spectrum at near laser conditions and temperatures and densities in a hollow cathode Argon-arc discharge."

J. Qu. Spect. Transf. 12 1517 1972.

[13] V.F.Kitaeva et al.

"Dependencies of the populations of the ArII levels in a CW Argon laser on the discharge tube diameter and magnetic field."

Sov. J. Qu. Elect. 1 341 1972.

[14] W.Demtroder

"Excitation mechanisms of pulsed Argon ion lasers at 4880A."

Phys. Letts. 22 436 1966.

[15] I.D.Latimer & R.M.St.John

"Simultaneous excitation and ionisation of Argon by electrons to the upper laser states of $Ar^+$."

Phys. Rev. A 1 1612 1970.

[16] H.S.Brandi

"On the mechanisms of excitation of laser states in singly ionised Argon."

Revisita Brasileira 4 469 1974.

[17] M.H.Dunn & J.N.Ross

"Investigation of population inversion by perturbation spectroscopy."

Phys. Letts. 44A 247 1973.

[18] I.E.Sakharov et al.
"Effect of plasma parameters on emission in an ion laser."
Sov. Phys.-Tech. Phys. 19 1081 1975.

[19] C.B.Zarowin
"Electron temperature and density in Argon ion laser discharges."
Appl. Phys. 15 36 1969.

[20] H.Statz et al.
"Transition probabilities, lifetimes and related considerations in ionised Argon lasers."
J. Appl. Phys. 36 2278 1965.

[21] L.Ward et al.
"Radiative lifetimes of excited levels in the homologous ions ArII, KrII and XeII."
Physica. Scripta. 31 149 1985.

[22] P.R.Woodruff et al.
"A measurement of the cross section for electron impact ionisation of $Ar^+$."
J. Phys. B 11 L305 1978.

[23] A.V.Loginov & P.F.Gruzdev
"Semiempirical calculation of transition probabilities and lifetimes of levels in the spectra of NeII and ArII ions: 3: Transition probabilities and lifetimes in the spectrum of ArII."
Opt. Spectrosc. 44 500 1978.

[24] J.D.Ridgen

"Metallic plasma tube for ion lasers."

IEEE J. Qu. Elect. QE-1 221 1965.

[25] K.G.Hernqvist & J.R.Fendley Jr.

"Construction of long life Argon lasers."

IEEE J. Qu. Elect. QE-3 66 1967.

[26] A.Maitland

"A plasma jet as cathode for an Argon laser."

Brit. J. Appl. Phys. (J. Phys. D) 2 535 1969.

[27] A.Maitland & J.C.L.Cornish

"Electron temperatures in a segmented metal argon-ion laser."

J. Phys. D 5 1807 1972.

[28] H.Boersch et al.

"High power ion lasers with wall stabilised arc discharge."

Phys. Letts. 24A 695 1967.

[29] H.Boersch et al.

"Saturation of laser power of CW ion laser with large bored tubes and high CW UV."

Phys. Letts. 31A 188 1970.

[30] R.Paananen

"Progress in ionised-Argon lasers."

IEEE Spectrum 3 88 1966.

[31] P.M.Armand

"The ionised Argon laser."

Ann. de Radioelectr. 22 191 1967.

[32] W.R.Bridges & A.N.Chester
"Spectroscopy of ion lasers."
IEEE J. Qu. Elect. QE-1 66 1965.

[33] S.N.Suchard
"Lasers - where are we now and where are we going?"
SPIE 92 174 1976.

[34] M.W.Dowley
"Reliability and commercial lasers."
Appl. Opt. 21 1791 1982.

[35] J.G.Eden
"Laser technology: theory and operating principles."
IEEE Potentials p.7 May 1985.

[36] B.H.Akerley & C.B.Hitz
"1987 laser economic review and outlook."
Laser Focus/Electron-Optics p.50 Jan. 1987.

[37] L.Holmes
"Advances in commercial lasers 1986-87."
Laser Focus/Electron-Optics p.38 Jan. 1987.

[38] A.J.DeMaria
"Laser Technology: its evolution into the market place."
IEEE Potentials p.13 May 1985.

[39] M.Zorgno
"The laser for tactical military applications."
Mil. Tech. p.194 1985.

[40] O.V.Laos
"How and why a laser?"
Electronics and Power p.381 May 1985.

[41] C.B.Hitz

"Medical lasers: A paradox of profitless prosperity."

Laser Focus/Electron-Optics p.76 Jul. 1987.

[42] M.Moretti

"A status report on lasers in medicine."

Laser Focus/Electron-Optics p.88 Apr. 1987.

[43] R.K.Mosavi

"Comparing laser and water jet cutting."

Laser and Optronics p.65 Jul. 1987.

[44] A.Masia

"Innovations in laser printing."

Photonics Spectra p.173 Apr. 1987.

[45] C.P.Christensen

"Some emerging applications of lasers."

Science 218 115 1982.

[46] W.Demtroder

"Laser Spectroscopy: Basic Concepts and Instrumentation."

Springer-Verlag, 1982.

[47] O.Svelto

"Principles of Lasers."

Plenum Press, 1986.

[48] A.Corney

"Atomic and Laser Spectroscopy."

Oxford University Press, 1977.

[49] A.Yariv

"Introduction to Optical Electronics."

Holt, Rinehart and Winston inc., 1971.

[50] A.Yariv

"Quantum Electronics"

J.Wiley inc., 1975.

[51] A.Maitland and M.H.Dunn

"Laser Physics."

North-Holland, 1969.

[52] W.B.Bridges et al.

"Gaseous ion laser research."

Tech. Rpt. No. AFAL-TR-67-69, Hughes Res. Labs. 1967.

[53] W.R.Bennett et al.

"Super-radiance, excitation mechanisms and quasi-CW oscillation in the visible $Ar^+$ laser."

Appl. Phys. Letts. 4 180 1964.

[54] B.E.Cherrington

"Gaseous Electronics and Gas Lasers."

Pergamon Press, 1979.

[55] T.Goto et al.

"Properties of Argon-ion lasers in Ar-He gas mixtures."

IEEE J. Qu. Elect. 6 159 1970.

[56] D.V.Veselov et al.

"Suppression of a plasma instability in an argon ion laser by a helium admixture."

Sov. Phys.-Tech. Phys. 23 1034 1978.

[57] V.A.Gilson

"Gas additives for stable pulse Argon ion lasers."

Rev. Sci. Inst. 40 448 1969.

[58] I.Kato et al.
"Time variation of the concentration of helium metastable atoms in He-$Kr^+$ ion laser."
J. Opt. Soc. Am. 69 175 1979.

[59] M.Birnbaum
"Improved performance of pulsed noble gas ion lasers with an axial magnetic field."
Appl. Phys. Letts. 12 86 1968.

[60] J.P.Goldsborough
"Cyclotron resonance excitation of gas-ion laser transitions."
Appl. Phys. Letts. 8 218 1966.

[61] T.Goto & S.Hattori
"Electron density in high-current pulsed Argon discharges."
J. Appl. Phys. 42 3005 1971.

[62] V.F.Kitaeva et al.
"Probe measurements of $Ar^+$-laser plasma parameters."
IEEE J. Qu. Elect. QE-10 803 1974.

[63] W.B.Bridges et al.
"Ion laser plasmas."
Proc. IEEE 59 724 1971.

[64] M.H.Dunn & J.N.Ross
"The Argon ion laser."
Prog. Quant. Electr. 4 233 1976.

[65] T.Fujimoto et al.
"Measurement of electron density and temperature in a pulsed Argon ion laser."
Mem. Sac. Eng. -Kyoto Univ. (Jap) 32 236 1970.

[66] I.Kato et al.
"Time variation of electron density in a pulsed He-$Kr^+$ laser."
J. Appl. Phys. 46 5051 1975.

[67] I.Kato et al.
"Time variation of internal plasma parameters in microwave-pulse-excited He-$Kr^+$ ion laser."
Jap. J. Appl. Phys. 16 597 1977.

[68] J.Eichler & H.J.Eichler
"Calculation of the optimum energy in an $Ar^+$-laser plasma."
Appl. Phys. 9 53 1976.

[69] R.I.Rudko & C.L.Tang
"Effects of cascade in the excitation of the ArII laser."
Appl. Phys. Letts. 9 41 1966.

[70] A.R.Striganov & N.S.Sventitskii
"Tables of spectral lines of neutral and ionised atoms."
Plenum Press, 1968.

[71] E.F.Labuda et al.
"A study of capillary discharges in noble gases at high current densities."
$18^{th}$ Gaseous Electronics Conf., Minneapolis, Minn.
20-22 Oct. 1965.

[72] S.Bashkin & J.O.Stoner
"Atomic energy level and Grotrian diagrams." Vol. II
North Holland, 1978.

[73] P.K.Cheo & H.G.Cooper
"Evidence for radiation trapping as a mechanism for quenching and ring-shaped beam formation in ion lasers."
Appl. Phys. Letts. 6 177 1965.

[74] J.Boscher et al.
"Output power saturation in high current regions of different noble-gas ion lasers."
Appl. Phys. 5 203 1974.

[75] I.Kato et al.
"Output power characteristics of microwave-pulse-excited He-$Kr^+$ ion laser."
Jap. J. Appl. Phys. 14 2001 1975.

[76] I.Kato et al.
"Spectroscopic studies of microwave-pulse-excited He-$Kr^+$ ion laser."
Jap. J. Appl. Phys. 16 1219 1977.

## Chapter 6 Laser Performance and Spectroscopy

This chapter contains the results of the experiments carried out to investigate the performance of the laser prototypes described in chapters 3 and 4. The output of these lasers is given as a function of gas pressure, tube diameter and input power characteristics. Time-resolved spectroscopy is used to monitor the pulsed laser output and the gas discharge properties. Conclusions are drawn about the excitation mechanisms occurring in the laser discharges, and a comparison is made between excitation frequencies and the use of transverse and longitudinal electric fields. Firstly a description of the apparatus used will be given.

### Experimental apparatus

This section describes the equipment which was used to obtain the results reported later in this chapter. It covers the gas handling system, the spectrometer and photomultiplier, the microwave sources and the laser coupling structures and their optics. The experimental procedures, the operating conditions, and to a certain extent, the reasons for the equipment choices, will also be given.

(i) The gas handling system

The laser tubes were filled with gas from the gas handling system. The gas handling system was based around an Edwards turbomolecular pump, and was constructed principally out of Edwards system components and connectors. Components were joined together via 'O'-ring type seals [1]. In order to minimise pressure gradient effects, the system was constructed out of large bore tubing and lengths were kept to a minimum.

In particular, the pressure gauges were located as close to the points of interest as possible. A block diagram and photograph of the arrangement are given on figs 6.1 and 6.2.

An Edwards Pirani gauge was used to measure pressures in the discharge below 0.2 mB. A Pirani gauge is sensitive to the gas type being measured and the absolute pressures are reported here [2]. A Vacuum General capacitance manometer was used to make measurements in the higher pressure regions between 0.2 and 10 mB.

The gas handling system was fitted with Neon, Argon, Krypton, Xenon and Helium cylinders, and small quantities of gas were easily manipulated using needle valves. Spectroscopy and leak rate measurements indicated that no significant impurities were present in the laser tubes. The tubes ranged in length from 40 to 100 cm depending upon the laser coupling structure used and had Brewster angled window holders attached at both ends. The tubes had an internal diameter of either 2, 3, 4 or 5 mm.

(ii) Time-resolving spectroscopic apparatus

An indication of the excitation processes occurring in a gas discharge can be found by observing the emission spectrum. The exciting microwave pulses were typically 1 uS long and the discharge pulses were of a similar duration. In order to effectively resolve these, an EMI9817B photomultiplier was used as a detector. This is a fast linear focused tube with a response time of around 2 nS and a transit time of 41 nS [3]. The photomultiplier was operated at a cathode-anode voltage of up to 2100 V giving a gain of around $10^7$. A fast rise-time photodiode was tried but its sensitivity was too low for carrying out the spectroscopy of the discharges. This was unfortunate as photodiodes are easier to use and have a less noisy output. The voltage divider circuit

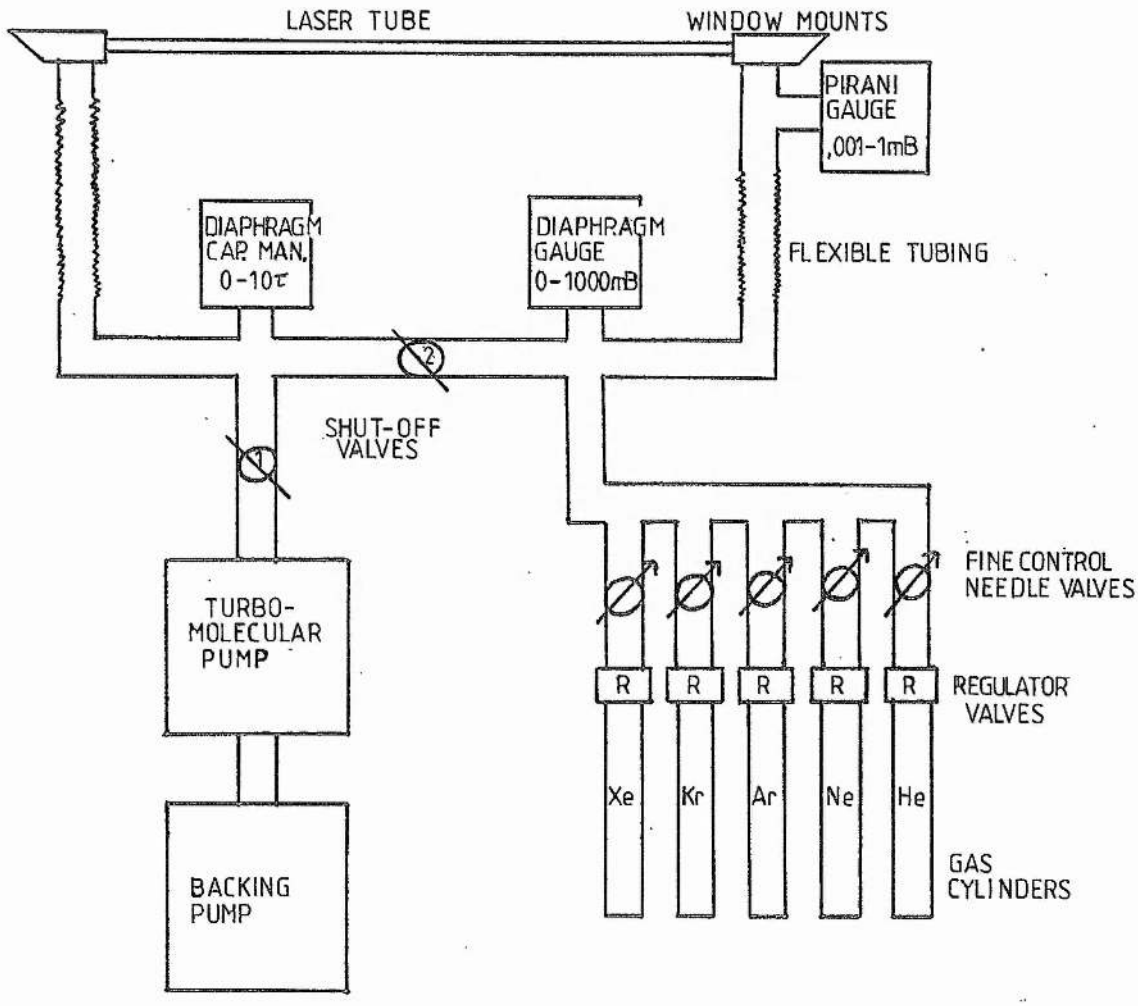


FIGURE 6.1 BLOCK DIAGRAM OF THE GAS HANDLING SYSTEM.

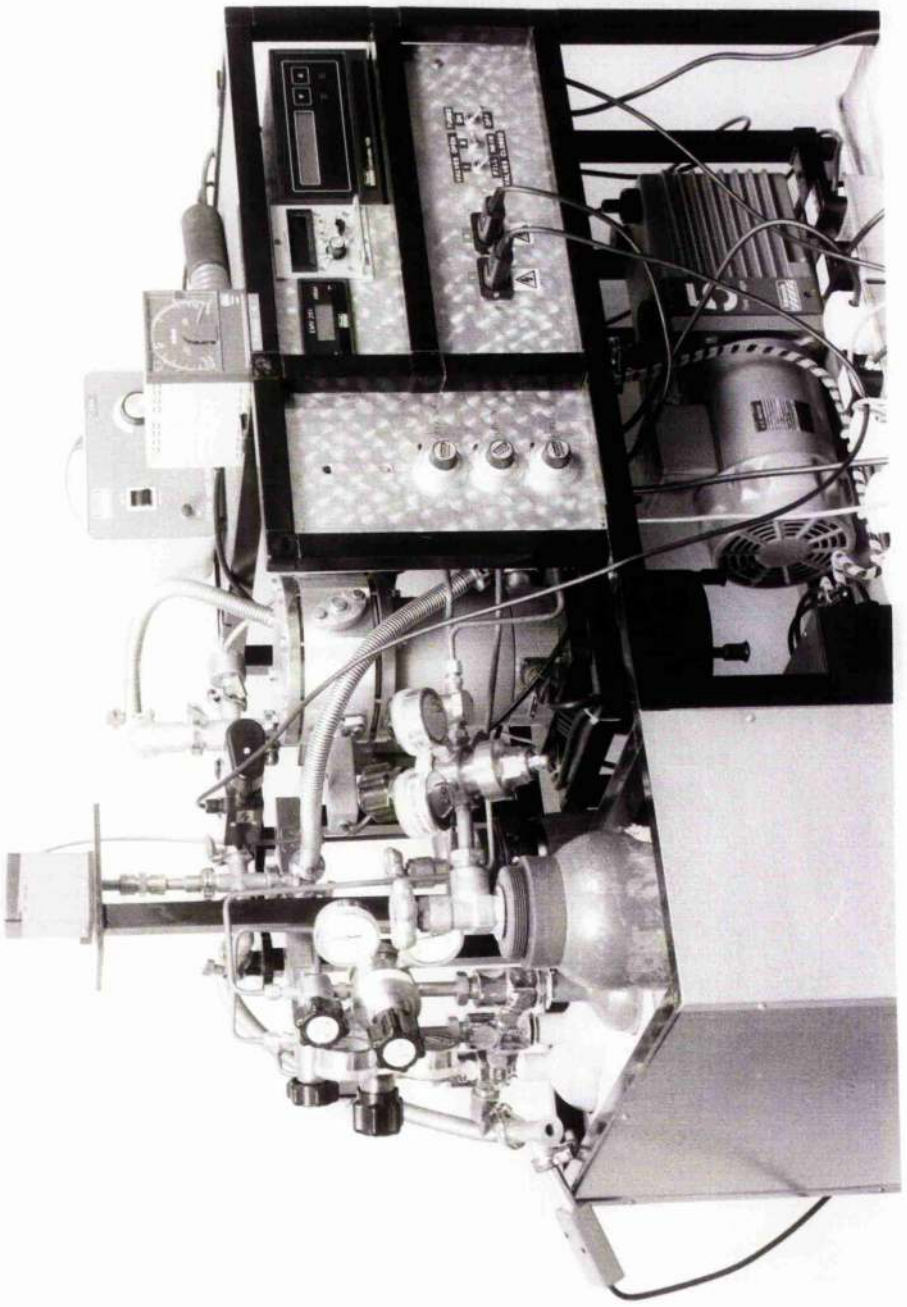

FIGURE 6.2 THE GAS HANDLING SYSTEM.

used to feed the dynode chain of the photomultiplier is shown on fig 6.3. This circuit was specially chosen and constructed for the high speed operation of the photomultiplier, and to maximise the linearity and dynamic range of the output [4].

The photomultiplier output current increases linearly with increasing incident light intensity until the onset of saturation. The anode current at which linearity starts to degenerate depends upon the photomultiplier used, the dynode chain, and the operating conditions. For fast focused tubes this usually lies at around 100 mA. The photomultiplier used for the experiments reported here was always operated in the linear region.

Generally speaking, a voltage divider network should be chosen for optimum performance for a particular application. There are a number of standard designs [4], but these must often be modified to best suit the required application. The circuit used on fig 6.3 was found to be well suited to the application reported here, although the output did have a tendency to saturate. This saturation was due primarily to an excessively large light intensity on the cathode. (Saturation can also be due to excessive gain of the dynode chain leading to a large anode current, but this was not considered to be a problem here). Saturation of the cathode resulted in an intensity saturation and distortion of the pulse shape. The entrance slit size of the spectrometer was used to regulate the light intensity to ensure that the photomultiplier operated in its linear region, thus avoiding saturation effects.

The spectral range of the EMI9817B lies between 300 nm and 800 nm as shown on fig 6.4. The output of the photomultiplier was fed into an oscilloscope via a 50 $\Omega$ coaxial line, and the oscilloscope was used to observe the time variation of the spectral line intensities isolated by

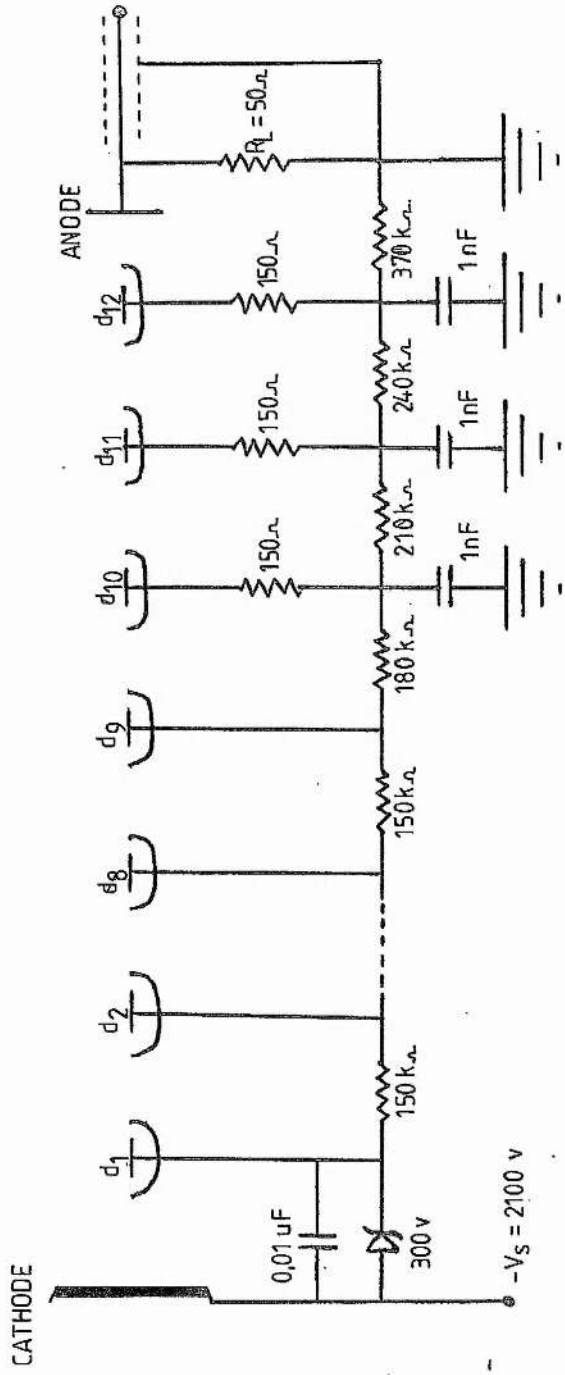


FIGURE 6.3 VOLTAGE DIVIDER NETWORK FOR A FAST LINEAR FOCUSED PHOTOMULTIPLIER.
(From Thorn EMI 1982, [4]).

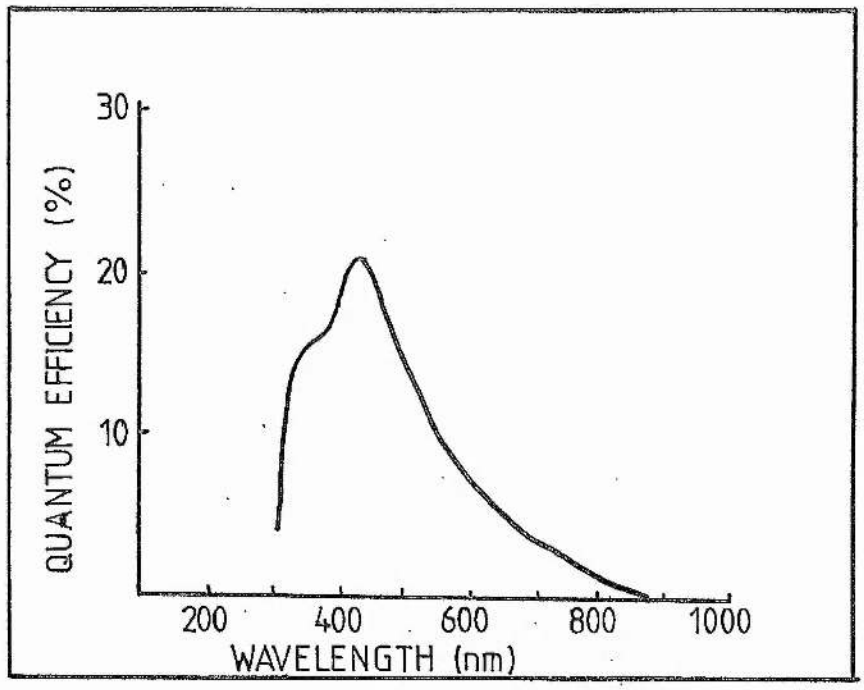


FIGURE 6.4 PHOTOMULTIPLIER SPECTRAL RESPONSE.
(From Thorn EMI 1986, [ 3]).

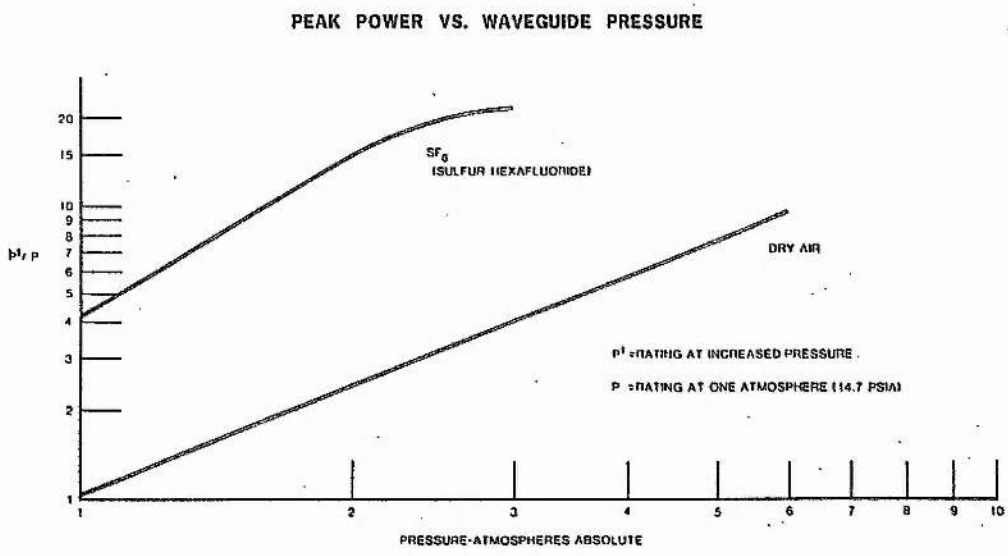


FIGURE 6.5 EFFECT OF GAS PRESSURE IN A WAVEGUIDE UPON BREAKDOWN POWER.
(From Litton Precision Products [ 5]).

the spectrometer.

A JENA SPM2 prism spectrometer was used which covered the spectral range 0.36 - 2.8 um. The spectral bandwidth admitted by the spectrometer into the photomultiplier chamber is a function of wavelength, as dictated by the dispersion of the prism, and of the entrance slit size. As an example, at 500 nm with a slit size of 0.1 mm, the admitted bandwidth is 0.5 nm. Spectral observations were made over the 360 - 800 nm range where the admitted bandwidth varied from around 0.2 to 2 nm respectively for a 0.1 mm entrance slit size. Entrance slit sizes of between 0.02 mm and 0.1 mm were used depending upon the intensity of the line being studied and the behaviour of the photomultiplier. This experimental arrangement was sufficient to identify all the major visible transitions occurring in the discharges.

(iii) The microwave power sources

Both CW and pulsed laser excitation were investigated. A TWT capable of delivering up to 120 W CW at 7.5 - 16.5 GHz was used to drive the CW discharges. Laser action was not observed for the CW case and this will be discussed later. The majority of the research was aimed at the analysis of pulsed discharges. These were powered by magnetrons capable of delivering up to 70 kW peak at 17 GHz, 120 kW at 10 GHz and 1 MW at 3 GHz, at a duty cycle in all cases of around 0.1%. Depending upon the magnetron used, microwave pulse lengths of 0.1 - 5 uS were available at repetition rates of 200 - 3000 pulses per second. Square pulses were produced with rise times of 10 - 20 nS and fall times of 30 - 50 nS.

At the upper power ranges of each of the three bands, breakdown of the air occurred either in the waveguide apparatus associated with the magnetron, or in the laser coupling structure. Such breakdown absorbs a lot of the power from the system and can also cause damage. As can be

seen from fig 6.5, pressurising the air inside a waveguide can greatly improve its power handling capacity. Compressed air at pressures of up to 5 atmospheres was available from the factory supply and this was sufficient to prevent breakdown in most of the laser coupling structures even when using the maximum available powers.

(iv) The laser coupling structures and their optics

Four laser coupling structures were constructed to investigate the effects of microwave frequency and the direction of the electric field upon the properties of the laser discharges. The transverse electric fields associated with microwaves in a waveguide are employed in three of the laser prototypes which operate at 3, 10 and 17 GHz (see chapter 3). In these prototypes, the laser tube is placed along the axis of a waveguide and microwave power is fed in from the sides via slots connecting the supply waveguide to the tube guide. The fourth prototype employs a helical structure which produces an axial electric field at 10 GHz (see chapter 4). The transverse and longitudinal field devices both produce electric fields at the laser tubes of around 100 kV/m.

Two sets of concave cavity mirrors were available, one set of two 100% reflecting mirrors, and another set comprising a 100% reflecting mirror and a 1% output coupler. The 100% reflectors had a transmission loss of less than 0.01% over a 430 - 680 nm bandwidth. The output coupler of the second set of mirrors had a transmission of 1% in the range 460 - 530 nm and 610 - 680 nm, (from Tech optics limited, Isle of Man). The mirrors all had a 3 m radius of curvature, and the lengths of the laser cavities were in the range 0.6 - 1.2 m. These cavities therefore, were all stable [6].

Ideally the cavity mirrors should have been placed in direct contact with the ends of the gas discharge tube. This is common practice

in low power ion lasers where hard coated optics are used. In the high power lasers however, the tube is sealed by windows at the Brewster angle [7] and the cavity is placed outside these. This is done partly to facilitate the easy change of optics and also because high power laser discharges have a tendency to damage the optics. The introduction of Brewster angled windows into a cavity increases the losses, and for low powered lasers in particular, this is undesirable. The laser prototypes all used quartz Brewster angled windows. A prototype was constructed which did not use these and its power output was approximately a factor of two higher as a result of the reduced cavity losses. However, this arrangement was less convenient to use because the optics could not be changed while the system was running. Another more serious problem was that the discharges tended to damage the mirror coatings. This occurred despite the fact that the mirrors had "hard" coatings.

**Laser Performance**

Pulsed laser action is observed in Argon, Helium-Argon and Helium-Krypton gas fills. No laser action is observed using a CW source. The parameters for the best operation of the microwave excited Argon ion and Helium-Krypton ion lasers are reported here. This includes the dependence of the output on the microwave frequency and the field direction.

(i) Pressure dependence of the laser output

The upper levels in a noble gas ion laser are excited by collisional encounters involving the high energy electrons in the laser discharge. The rate at which these collisions occur depends upon the gas pressure in the discharge. If collisions occur too frequently, the electrons have insufficient time between collisions to build up enough

energy from the electric field to populate the upper laser levels. Similarly, if there are too few collisions, insufficient excitation will occur. Hence, there is an optimum pressure at which the population processes operate most efficiently.

The presence of additional gases in a discharge often affects its properties. For example, impurities such as water usually have a detrimental effect on a laser discharge, reducing the electron density and temperature. The gas handling system, described earlier in the chapter, is of good quality, ensuring the cleanliness of the system. Helium, on the other hand, can enhance the output of a laser by increasing the electron temperature or by resonant transfer excitation via metastable levels.

In order to find the optimum gas pressures for the four laser prototypes described earlier, the outputs were measured as a function of gas pressure. From figs 6.6 to 6.9, it can be seen that for the Argon ion laser, the 488.0 nm and 476.5 nm lines are the most prominent. Generally the 496.5 nm and 514.5 nm lines are below threshold in pure Argon, but when Helium is added they are observed. In all cases, the optimum Argon pressure, when Helium is added, is approximately 0.09 mB for all transitions. This is higher than the optimum pressure in pure Argon, which is around 0.06 mB. A similar study was carried out for the Helium-Krypton ion laser. The optimum Krypton pressure is found to be 0.05 mB in all cases and a Helium pressure of around 10 mB is best. Laser action is only observed for the 469.4 nm transition. The output is found to be a sensitive function of Krypton pressure with laser action being limited to the range 0.04 to 0.06 mB. The Helium pressure is less critical. No laser action is observed in pure Krypton.

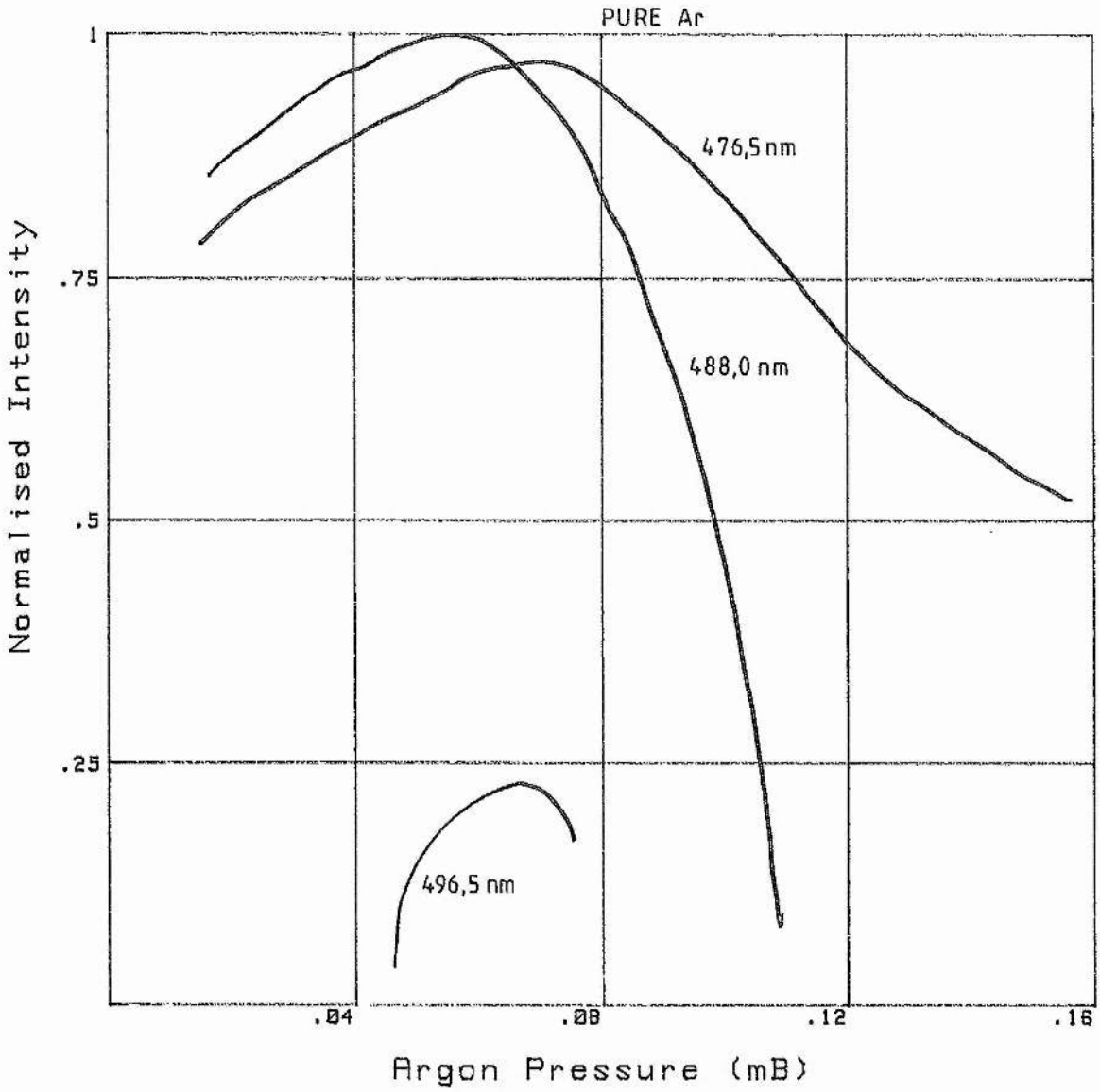


FIGURE 6.6a

EFFECT OF Ar & He PRESSURE ON THE OUTPUT OF THE 3 GHz TRANSVERSELY EXCITED LASER

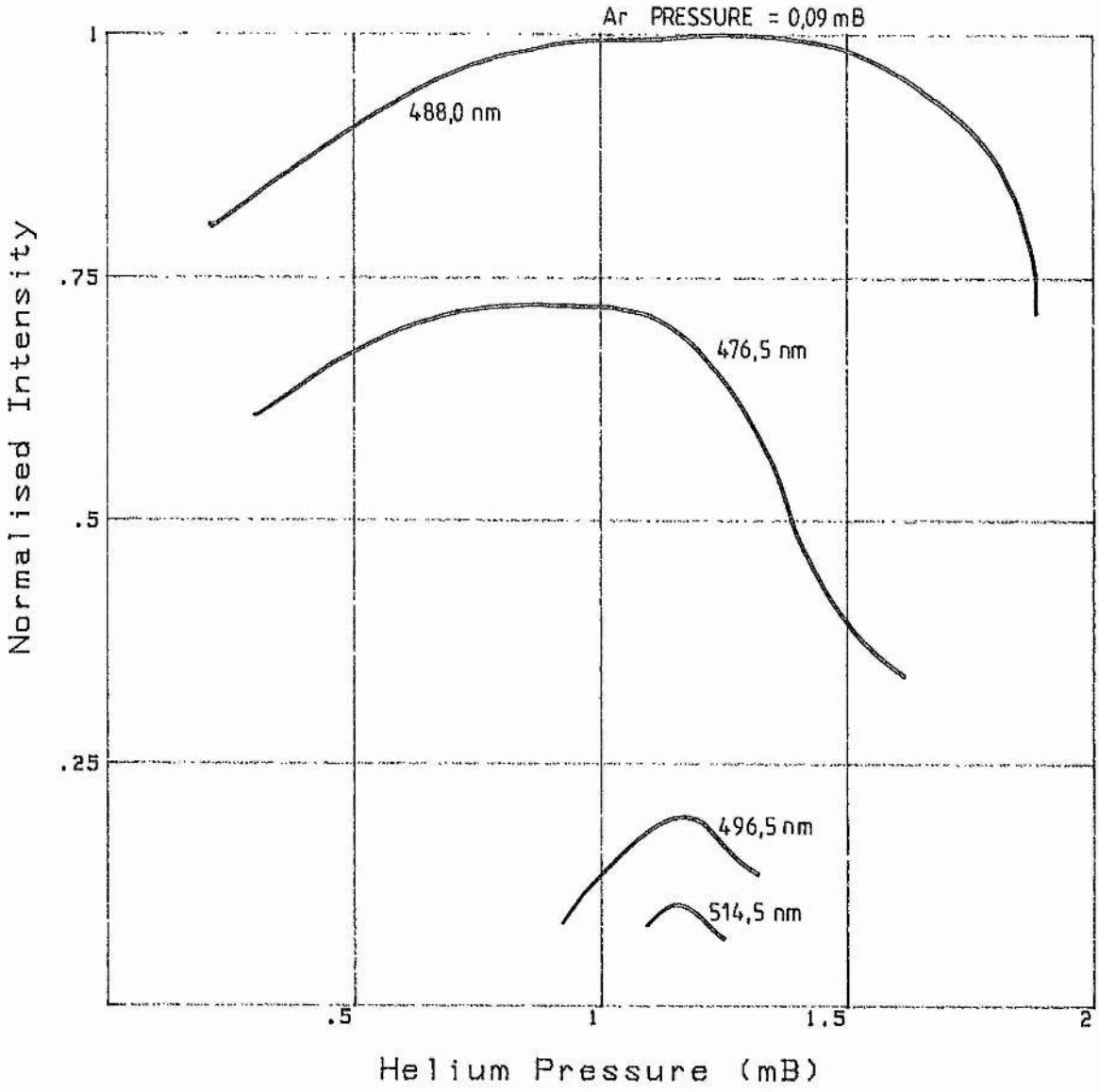


FIGURE 6.6b

EFFECT OF Ar & He PRESSURE ON THE OUTPUT OF THE 3 GHz TRANSVERSELY EXCITED LASER

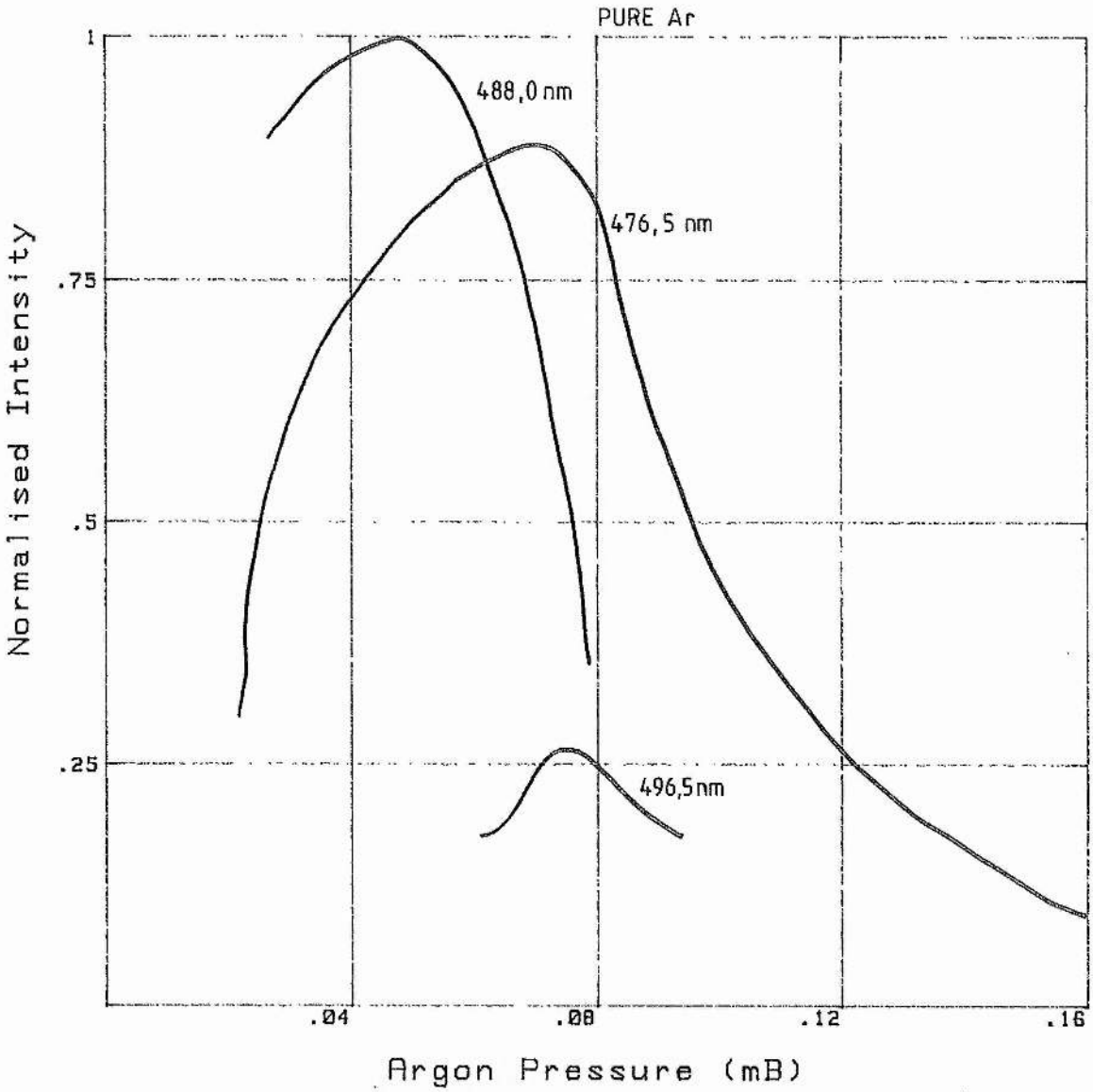


FIGURE 6.7a

EFFECT OF Ar & He PRESSURE ON THE OUTPUT OF THE 10 GHz TRANSVERSELY EXCITED LASER

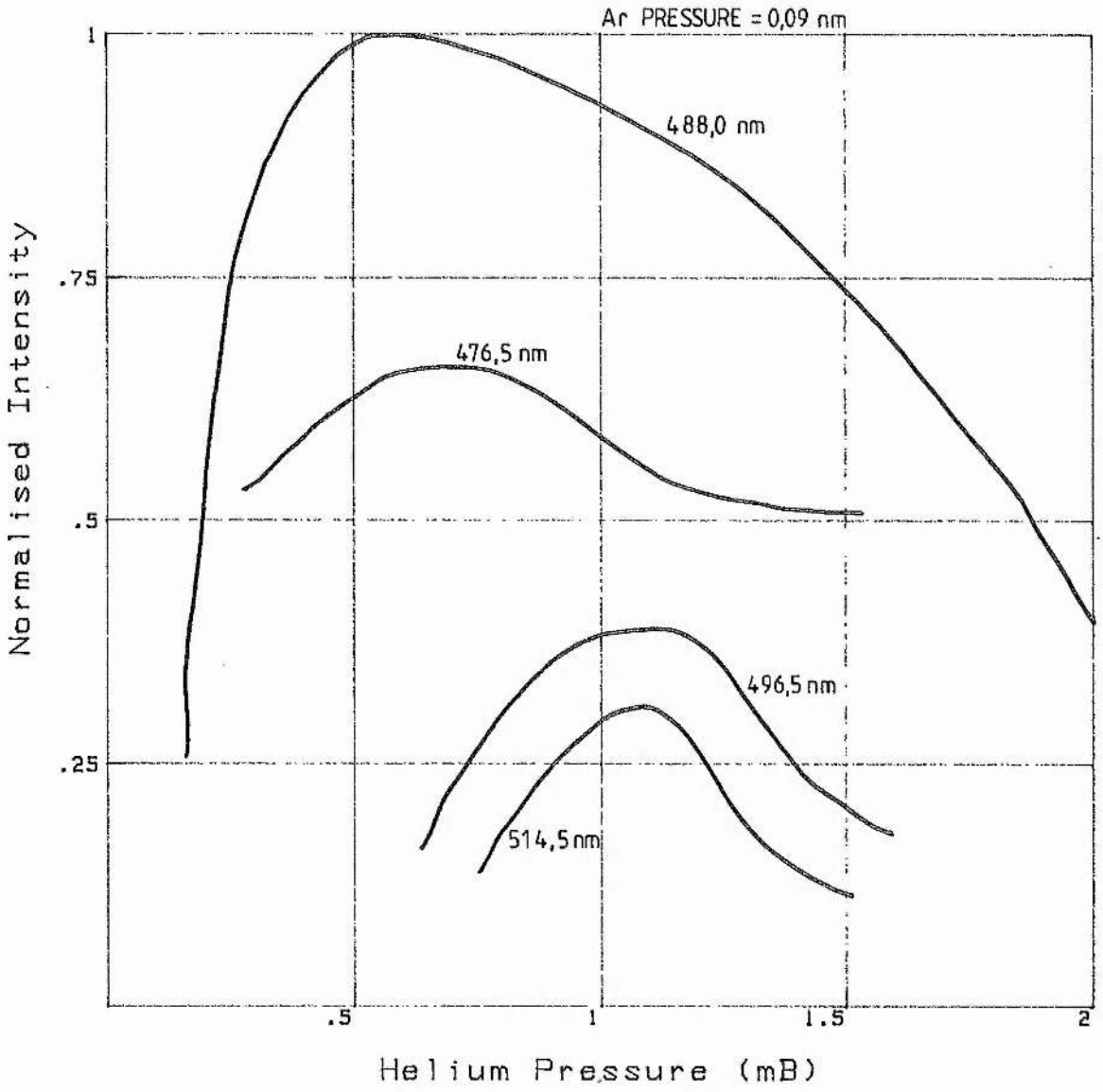


FIGURE 6.7b

EFFECT OF Ar & He PRESSURE ON THE OUTPUT OF THE 10 GHz TRANSVERSELY EXCITED LASER

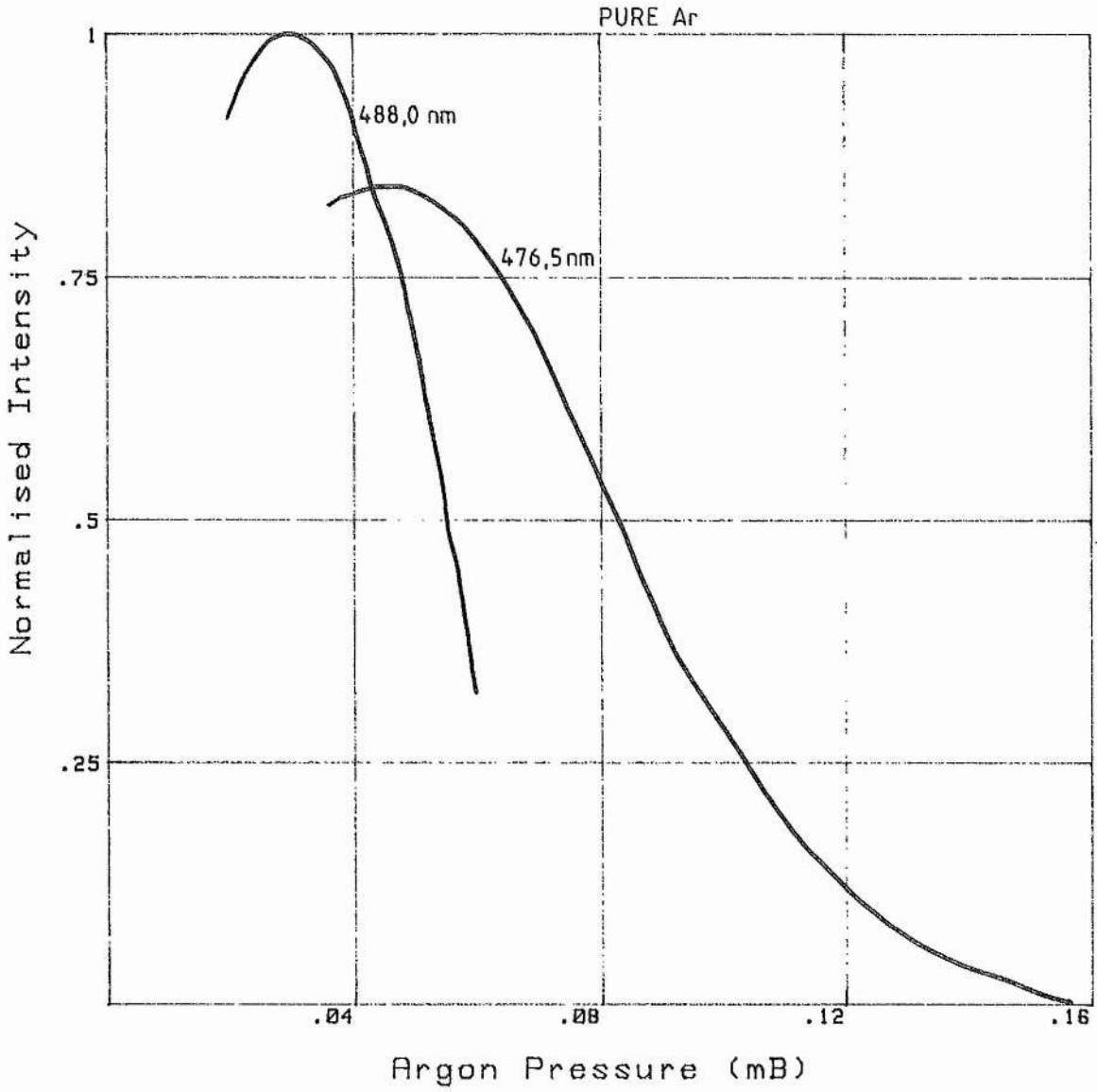


FIGURE 6.8a

EFFECT OF Ar & He PRESSURE ON THE OUTPUT OF THE 17 GHz TRANSVERSELY EXCITED LASER

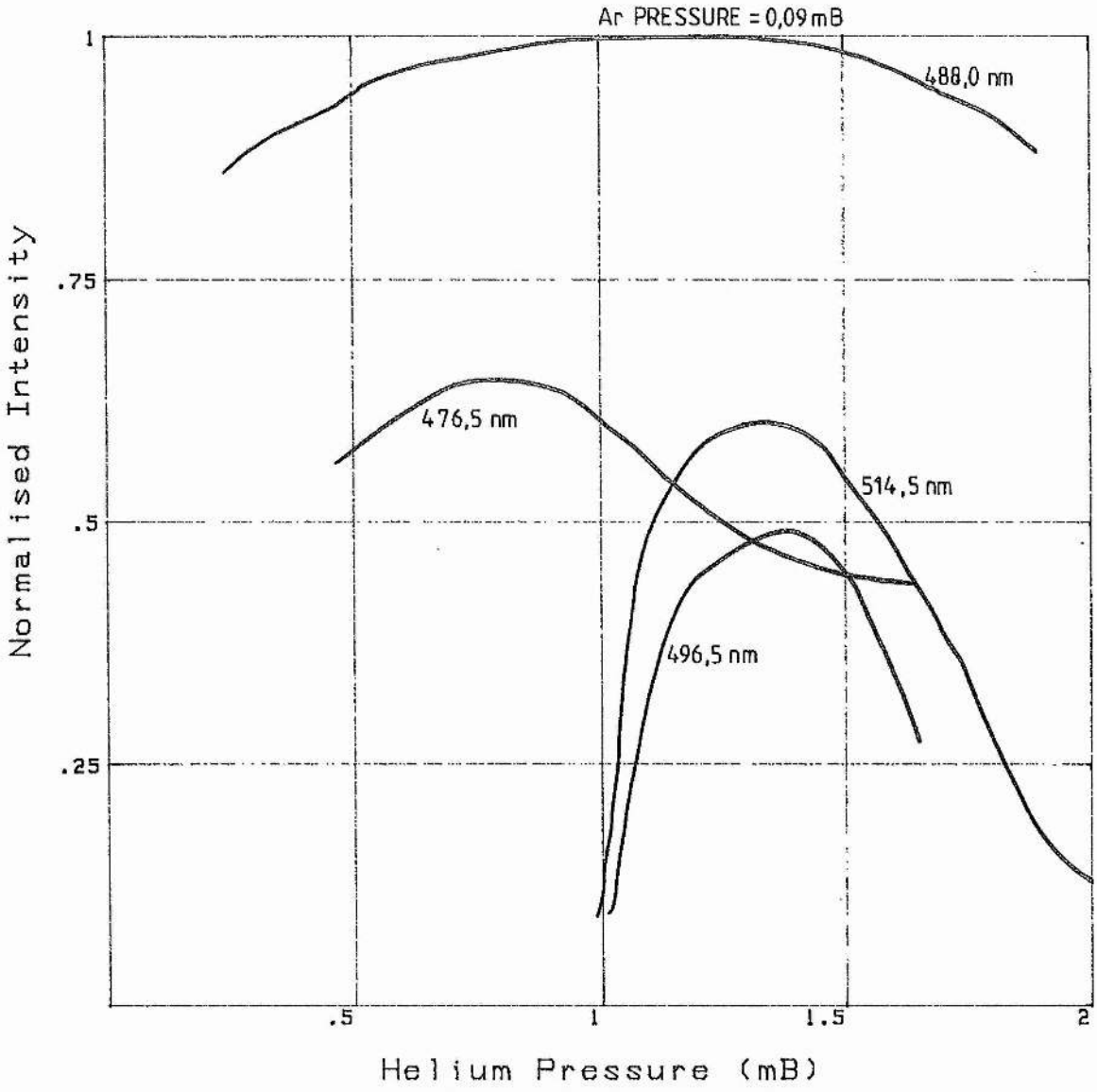


FIGURE 6.8b

EFFECT OF Ar & He PRESSURE ON THE OUTPUT OF THE 17 GHz TRANSVERSELY EXCITED LASER

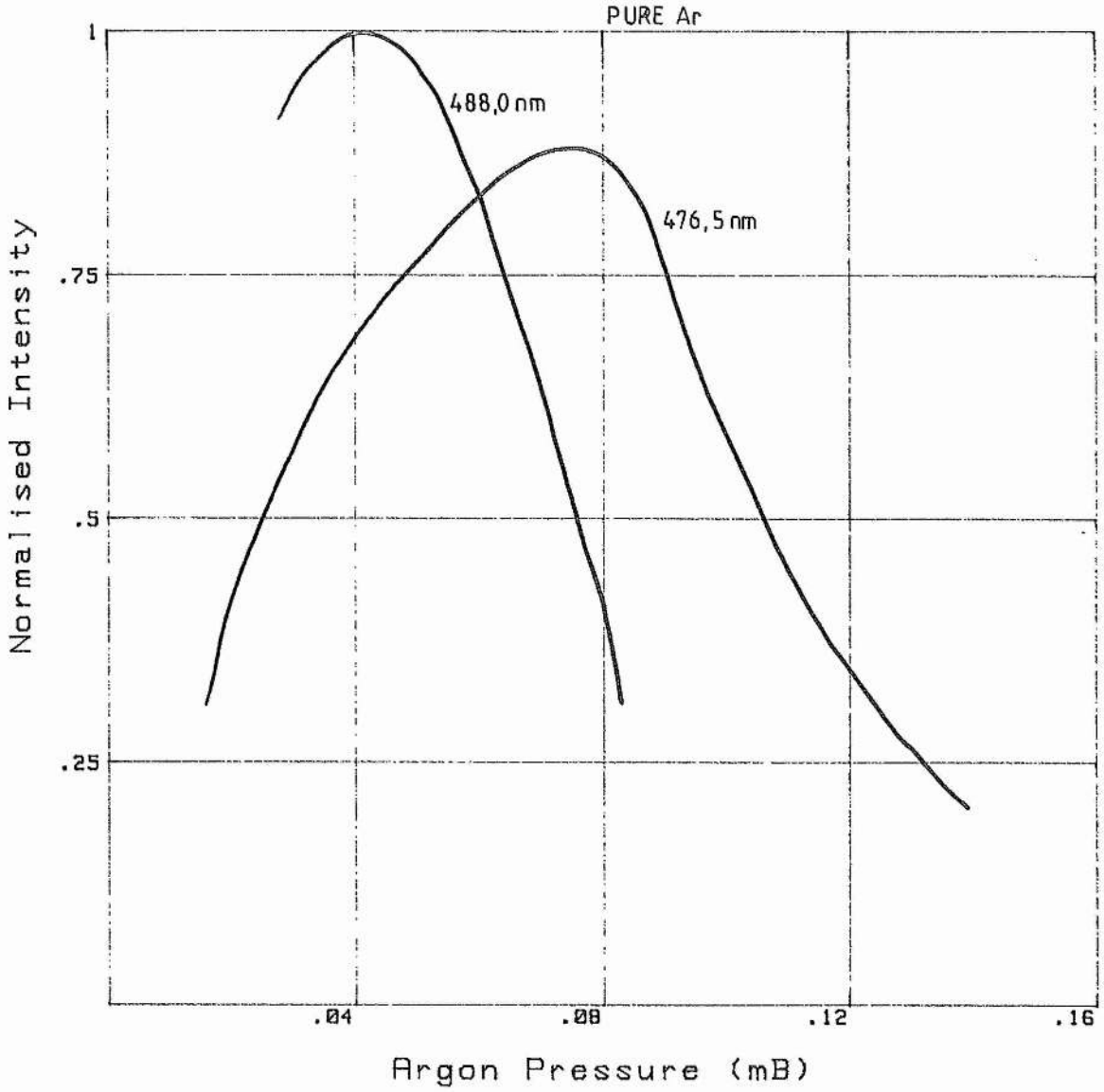


FIGURE 6.9a

EFFECT OF Ar & He PRESSURE ON THE OUTPUT OF THE 10 GHz LONGITUDINAL EXCITED LASER

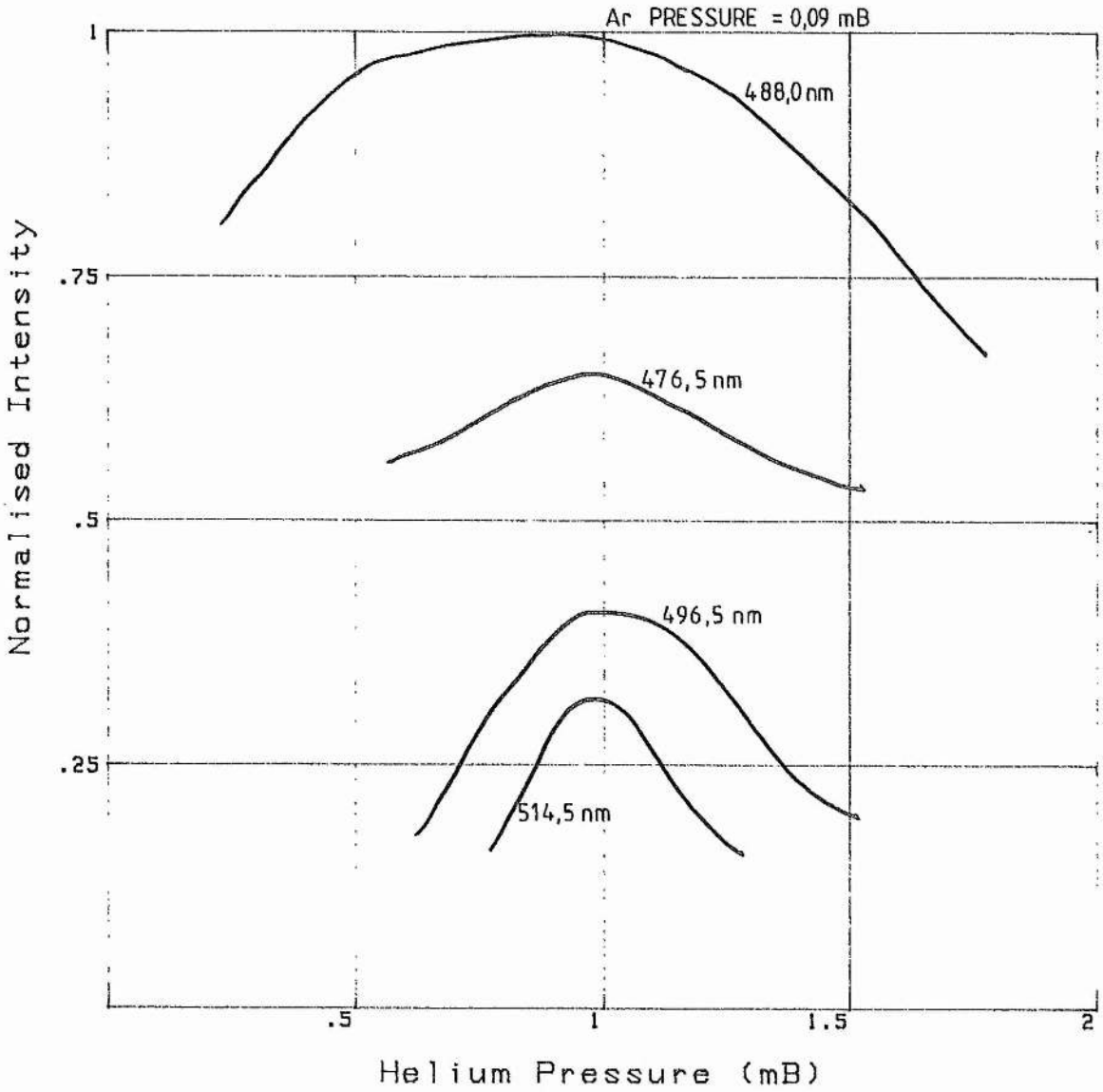


FIGURE 6.9b

EFFECT OF Ar & He PRESSURE ON THE OUTPUT OF THE 10 GHz LONGITUDINAL EXCITED LASER

(ii) Effect of tube diameter

Noble gas ion lasers require a high current density and so narrow bore tubes are generally used. (High power Argon ion lasers are able to use larger tube diameters because of their higher input powers). Current density requirements normally place an upper limit on the tube diameter. Electron losses at the container walls are largest for small tube diameters thus imposing the lower limit on the diameter. At the optimum tube diameter, a balance is normally set between current density requirements and an acceptable electron loss rate. As will be discussed shortly, the direction of the exciting electric field is unimportant when using microwave frequencies. This is not the case when using a DC field because here, electrons are driven into the tube walls by a transverse field thus increasing electron losses.

The Argon ion laser outputs from all four laser prototypes are observed to be a sensitive function of tube diameter. In all cases, the best internal tube diameter is 3 mm. The tube diameter-optimum pressure product is found to equal a constant ($\sim$0.15 mm-mB). The optimum tube diameter for the Helium-Krypton ion laser is observed to be between 3 and 4 mm. The output in this case is not as sensitive a function of tube diameter.

(iii) Effect of the input power characteristics

The microwave sources described in the previous section have a variable power, pulse length and pulse repetition frequency (prf). These were used to investigate the variation of the laser output as a function of the input parameters. The pulse repetition frequency was found to have no noticeable effect on the output at the prfs used. This is because de-excitation and recombination generally occur in times much shorter than the time between pulses. Increasing the prf increases the

duty cycle of the output, and if a supply is operating at maximum power, a corresponding reduction in the power per pulse is required. For high power pulses therefore, a low prf must be used. An increase in the prf should improve the residual ionisation level between pulses, thus improving the breakdown consistency.

The pulse length is observed to have a significant effect on the laser output. The pulse length must be long enough to firstly create sufficient ionisation for breakdown, and then to allow the build up of the upper laser level populations. The more powerful the pulse is, the shorter is the minimum required pulse length. It can be seen from fig 6.10 that, after a delay of around 0.4 uS, the 488.0 nm Argon ion laser pulse approximately follows the temporal behaviour of the exciting microwave pulse. This is typical of all the observed Argon ion laser lines. The microwave pulses have a fall time of up to 50 nS and the Argon ion laser pulses cease 50 - 300 nS after the microwave pulse has started to decline. Microwave pulses longer than 5 uS were not available, but there is no reason to suggest that CW excitation is not possible for a sufficiently high pump power. The intensity of the 5 uS laser pulses is smaller than for the 1 uS pulses because the peak power of the pump pulse was reduced so that the maximum duty cycle of the supply was not exceeded. The laser pulse of the Helium-Krypton ion laser is independent of the pulse length for pulses longer than 0.5 uS. This is because population of the upper laser level occurs in the afterglow due to interaction with Helium metastables after the end of the microwave pulse.

No saturation of output is observed as the input power is increased either in Argon or Krypton. In all cases, increasing the power input, increases the output. No laser action is observed using a CW source, or

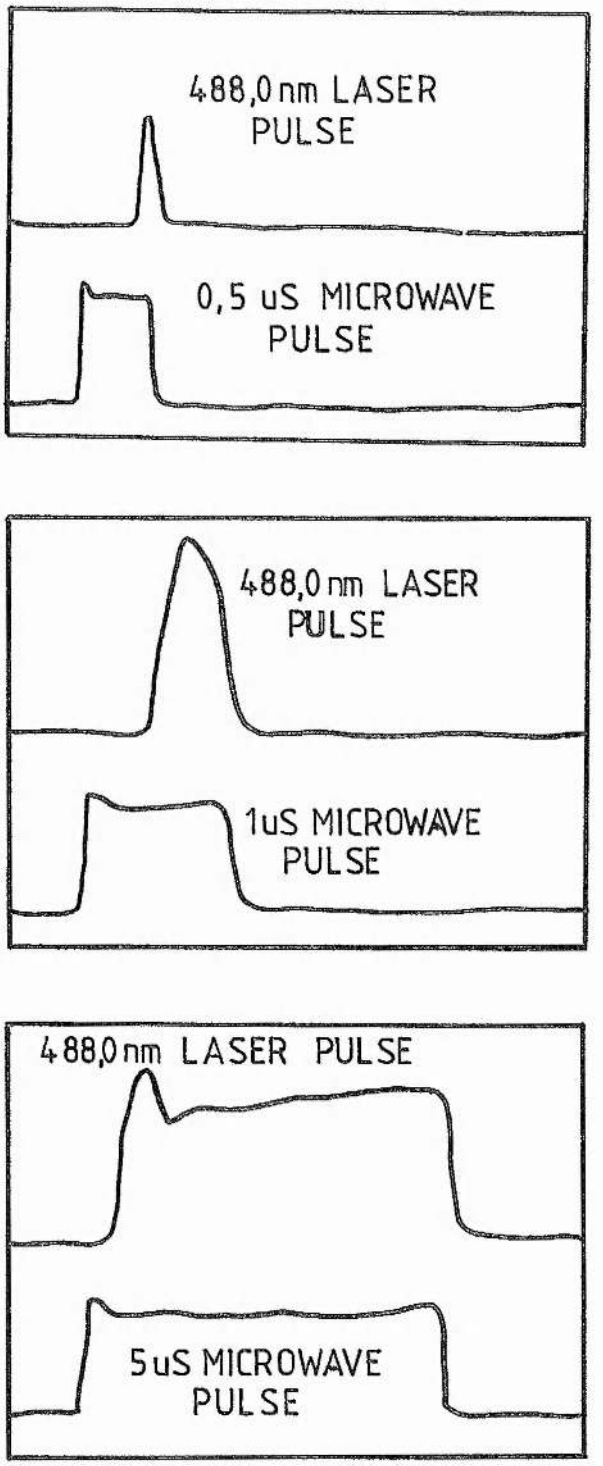


FIGURE 6.10 EFFECT OF MICROWAVE PULSE LENGTH UPON THE 488.0 nm ARGON ION LASER PULSE.

in pure Krypton or Xenon using a pulsed source. The Argon and Helium-Krypton ion lasers have the highest gains of all those tried.

(iv) Time-resolved spectroscopy of the laser output

The spectrometer and photomultiplier were used to display the laser pulses on an oscilloscope. Care has to be taken not to saturate the photomultiplier as this badly distorts the recorded pulse shapes. The form that this distortion takes depends upon the type of photomultiplier used and its associated voltage divider network. For the configuration used here, a saturating pulse looked narrower than it really was. Often this had the effect of making the laser pulse look as if it had finished well before the end of the microwave pulse. The entrance slit size was used to keep the light intensity incident upon the photomultiplier within the linear limits of the photomultiplier. Knowing the time variation of the laser pulses, power measurements made using a pyrometric laser power meter can be used to give the peak output power.

For the Argon and Helium-Argon gas fills, all the observed lines follow a trend similar to those shown on fig 6.10. For a 1 uS microwave pulse the laser pulse is typically around 0.7 uS long. The addition of Helium can enhance the output of the laser due to the increase in the electron temperature of the discharge. No afterglow laser action is observed. Using the pyrometric laser power meter all four prototypes are found to have a maximum output of up to approximately 0.1 mW mean. This gives a typical maximum peak power of up to around 100 mW.

The output of the Helium-Krypton ion laser is shown on fig 6.11. It can be seen that laser action at the 469.4 nm line occurs in the afterglow about 2 uS after the end of the microwave pulse. The laser pulse then lasts for up to 5 uS. A mean output power of up to 0.1 mW is observed giving a peak power of about 30 mW.

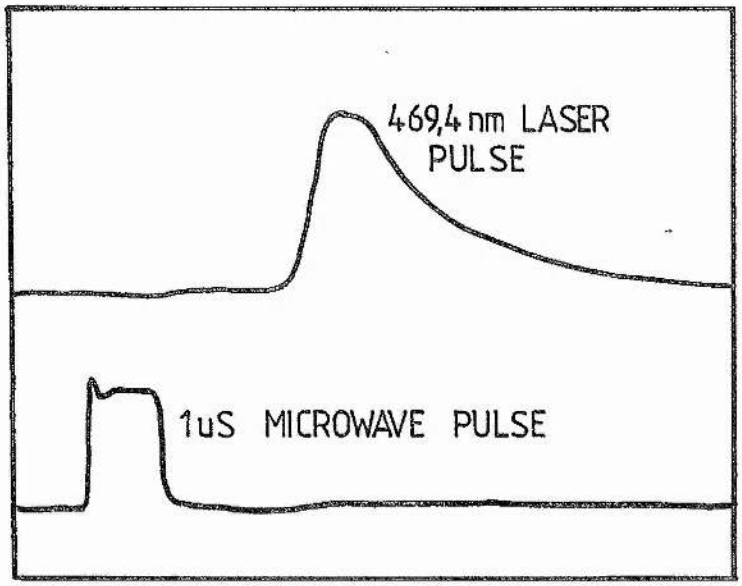


FIGURE 6.11 TIME VARIATION OF THE 469.4 nm HELIUM-KRYPTON ION LASER PULSE.

(v) Effect of microwave frequency

The microwave-to-collision frequency ratio is an important parameter of the microwave discharge dictating the power absorption efficiency, the significance of wall collisions and transmission at a boundary. The three transverse excitation prototypes were used to compare performance as a function of microwave frequency. These operate at 3, 10 and 17 GHz giving an $\omega/\nu_m$ ratio of between 90 and 500.

As has been described in chapter 2, the field which actually penetrates the dielectric/laser-discharge boundary is very small ($\lesssim$ 1%). This means that the effects of microwave frequency upon the excitation processes in the gas discharge tend to be masked. (For example, the fields in the 3 GHz laser tube are liable to be highest, because low frequency fields generally find it easier to penetrate the dielectric/gas-discharge boundary of the prototypes). In all cases, the electric fields inside the laser tubes are small enough so that wall collisions due to the transverse electric field can be neglected. For very large fields, such wall collisions would be most significant at low frequencies because electrons would get driven into the walls before the field direction had reversed.

No significant differences in the performance of the 3, 10 and 17 GHz prototypes is observed when using Helium, Argon and Krypton gas mixtures. They all have approximately the same optimum gas pressures and tube diameters and the output pulses are very similar. The small differences which are observed between the prototypes cannot definitely be attributed to frequency effects. No obvious differences are observed in the spectra of the laser discharges excited at 3, 10 and 17 GHz. It is likely therefore, that the laser level population processes are similar in each case. This is in agreement with the findings in chapter

2, where it is shown that, provided $\omega$ is much greater than $\omega_p$ and $\omega/\nu_m$ is greater than 1, microwave power absorption is approximately independent of frequency. For the cases reported here therefore, the exciting microwave frequency can be chosen for convenience, depending on the equipment available.

(vi) Comparison between transverse and longitudinal excitation

Transverse excitation of an ion laser using a DC field is not viable due to the large electron losses and damage to the container walls which would occur. Because of the oscillating nature of a microwave field, transverse microwave excitation is feasible. The coupling structures of chapters 3 and 4 produce fields which are predominantly transverse for the waveguide coupler, or axial for the helical structure. The fields produced and the active lengths of the 10 GHz waveguide coupler and the 10 GHz helical structure are similar, thus allowing a comparison to be made between transverse and longitudinal excitation. For the magnitude of the fields used, both devices performed equally well. If much larger fields were to be applied to the discharge, the longitudinal field prototype would be expected to perform better than the transverse prototype. This is because the electric field would then be large enough to drive electrons into the tube walls before the field direction had reversed.

**Time-resolved spectroscopy of the laser discharges**

The apparatus described at the start of the chapter was used to carry out time-resolved spectroscopy of the laser discharges. This information can be used in conjunction with the laser performance data to give an indication of the excitation processes in the discharge, and to suggest ways of improving the output.

(i) Laser discharge spectroscopy

No laser action is observed in pure Krypton or Xenon. Observations of the spontaneous emission spectra show a good degree of ionisation and the atomic transitions are observed to be weak. The laser transitions are prominent, and cascade excitation is negligible. The same properties are observed in the Argon ion laser discharge. A typical Argon ion discharge spectrum is given on fig 6.12, where it can be seen that singly ionised transitions dominate. Over the range of microwave frequencies used, field frequency and direction have no noticeable effect on the discharge spectra.

By using the tables on figs 5.10 and 5.11 and in [8], it can be seen that, in all the cases examined, the high lying singly ionised and doubly ionised state populations are low, hence the negligible laser level population via cascade transitions. In order to improve the high lying state populations, the pump power should be increased. Doing this would improve the Argon ion laser output and bring the Krypton and Xenon discharges above threshold.

In order for the upper levels of an Argon ion laser to be populated as efficiently as possible, the discharge must have a mean electron energy of around 6 eV (see chapter 5). The low output powers observed suggest that the electron energy of the discharges is below this value. An estimate of 4 eV has been made on the basis that ionic transitions predominate but that cascade excitation is negligible. At mean electron energies of much lower than 4 eV, insufficient energy is available to populate the laser levels. The addition of Helium increases the electron energy of a discharge slightly and this accounts for the slight increase in the observed laser output from a Helium-Argon gas mixture.

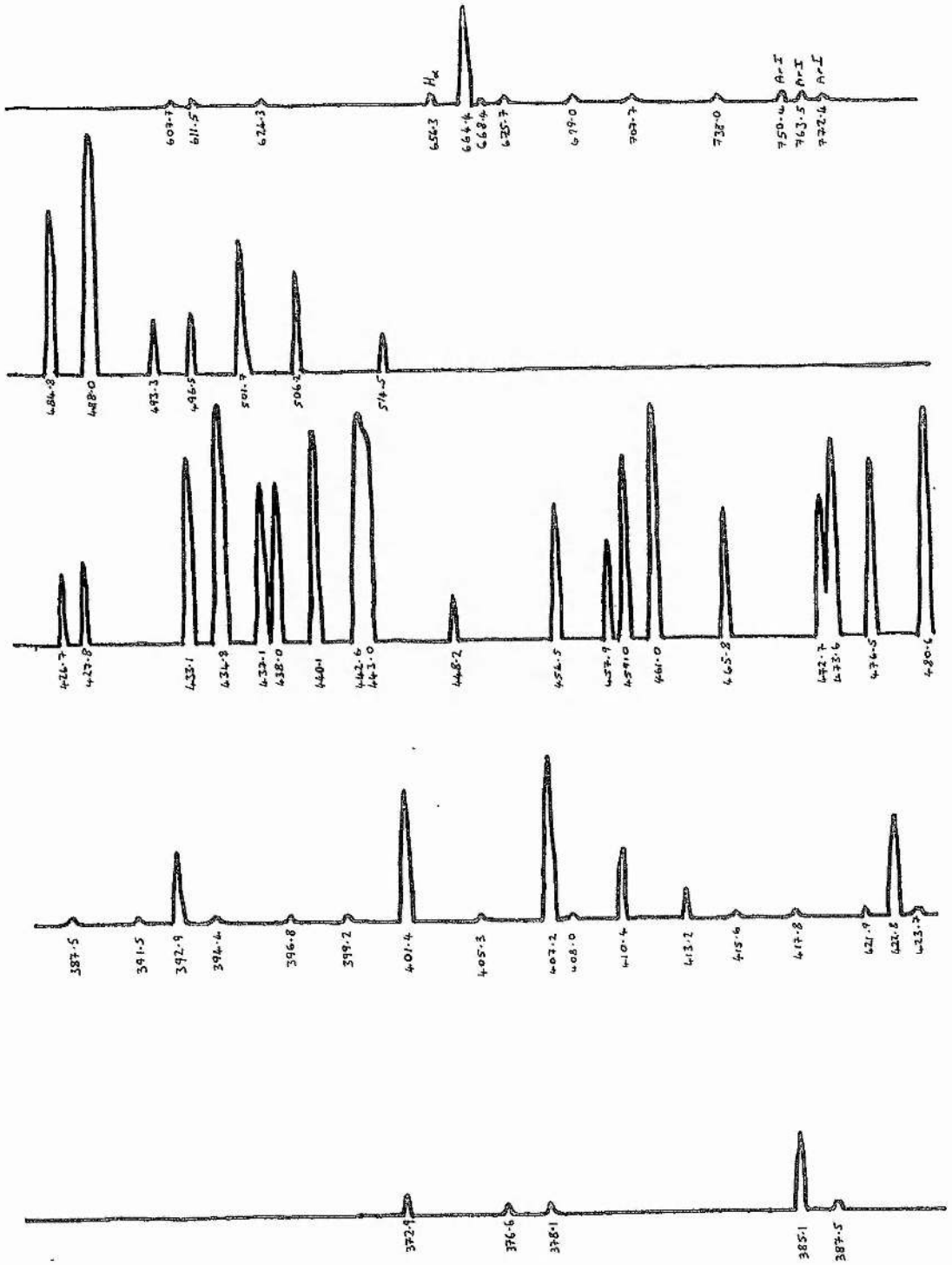


FIGURE 6.12 SPONTANEOUS EMISSION SPECTRUM OF A 10 GHz LONGITUDINALLY EXCITED ARGON ION LASER DISCHARGE.

(ii) Time-resolved transition behaviour

The temporal behaviour of the spontaneous emission of selected lines in an Argon ion laser discharge is given on fig 6.13. It is seen that the atomic and singly ionised transitions have the same temporal form, although, as has already been stated, the singly ionised lines are considerably stronger than the atomic lines. The delay between the start of the microwave pulse and the discharge is, in both cases, approximately 250 nS. All emission stops at the end of the microwave pulse and the laser pulses are similar in form to the spontaneous emission. The doubly ionised transitions are weak and it can be seen from the figure that the doubly ionised states take longer to populate. This is probably due to the multi-step excitation processes which populate these states. In a more energetic discharge, the doubly ionised transitions would be more prominent.

In a pure Krypton discharge, the transition behaviour is very similar to that observed for Argon. Many Krypton lines however are observed also in the afterglow although this radiation is generally weak. When Helium is added, certain Krypton transitions are observed to exhibit strong afterglow action. The 469.4 nm and 438.6 nm lines are particularly prone to this due to resonant transfer excitation from Helium metastables (see chapter 5). This is shown on fig 6.14, where the 388.8 nm atomic Helium line indicates the time variation of the population of the $2s^3S$ Helium metastable involved in the excitation of the 469.4 nm and 438.6 nm upper levels. Although laser action is only observed at 469.4 nm, because of the 438.6 nm line enhancement, laser action should also be possible here for a sufficiently high pump power.

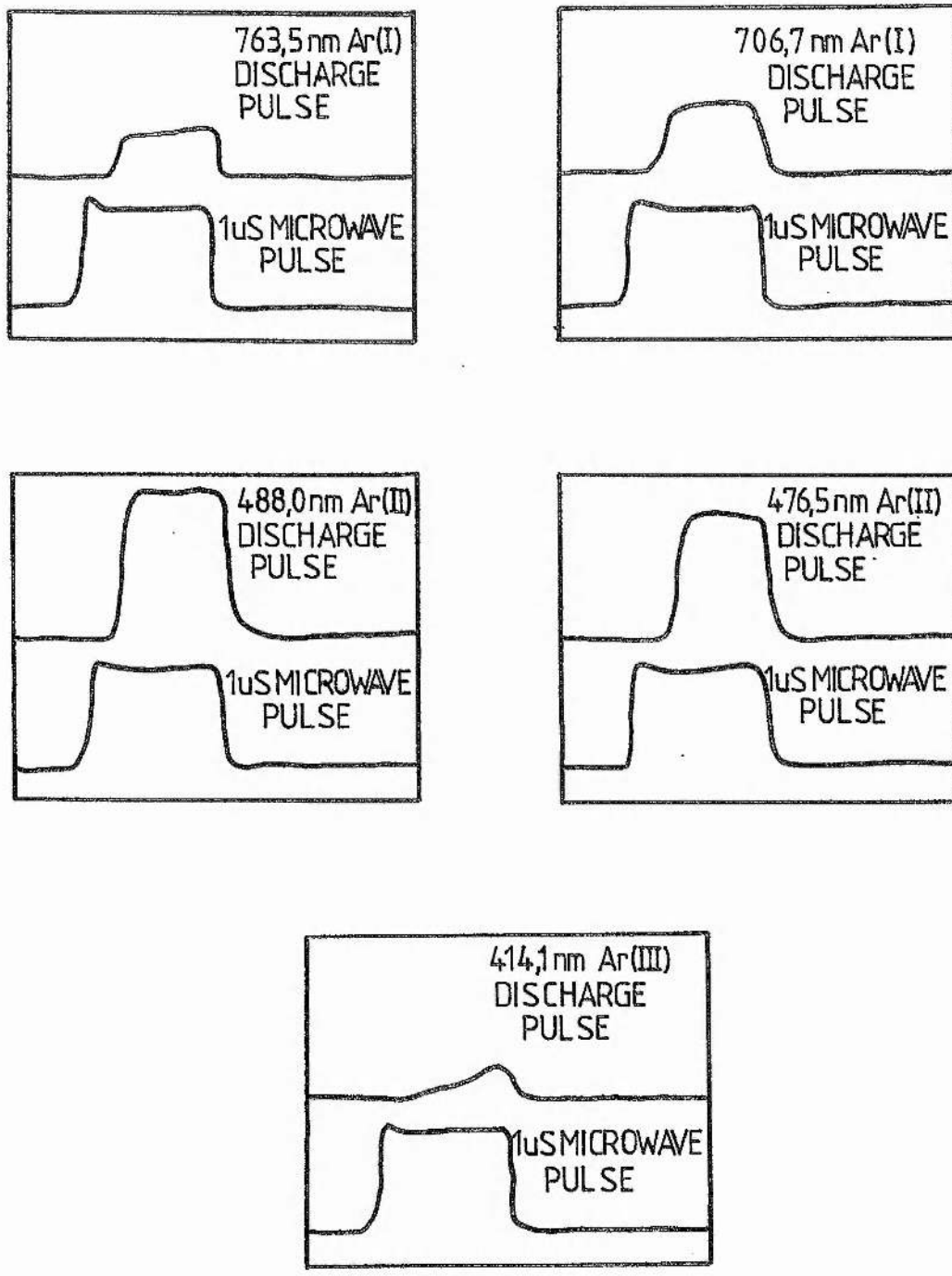


FIGURE 6.13 SPONTANEOUS EMISSION OF SELECTED LINES FROM A PULSED ARGON ION LASER DISCHARGE.

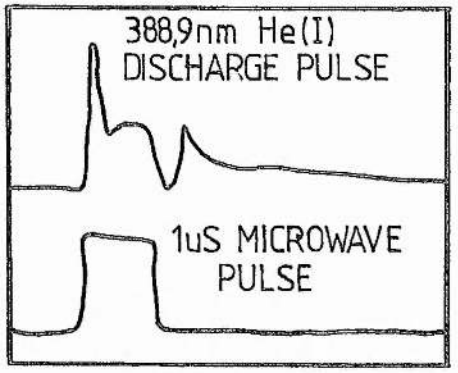


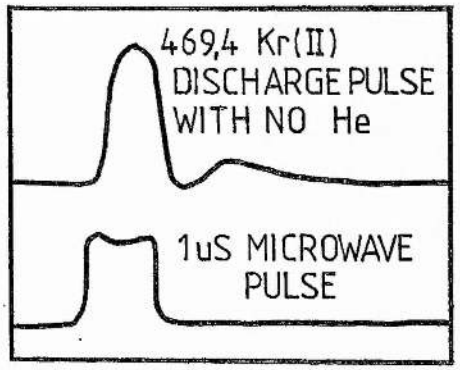


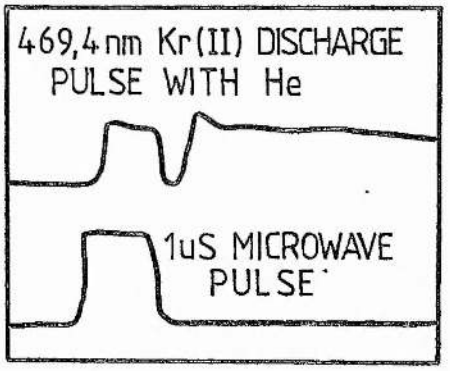


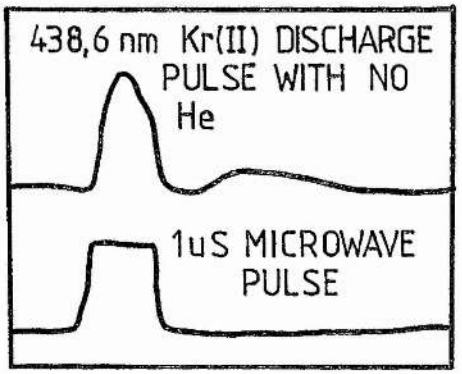


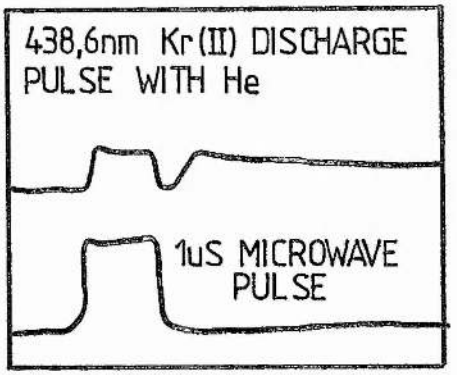


FIGURE 6.14 SPONTANEOUS EMISSION OF SELECTED LINES FROM A PULSED HELIUM-KRYPTON ION LASER.

(iii) Excitation mechanisms

There are a number of possible excitation processes which can occur in the laser discharges studied here and these have been described in chapter 5. Because of the lack of atomic lines in the spectrum of the Argon ion laser discharge, a multiple-step excitation process is not the predominant excitation process. Similarly, cascade excitation is observed to be negligible due to the poor excitation of states with energies above the laser levels. A two-step excitation process via the Argon ion ground state is likely to play some part in the discharge, but because of the pulsed nature of the field and the lack of observed atomic lines, a single-step excitation process is the most likely.

In the Helium-Krypton ion laser discharges, the presence of Helium is essential for laser action and the spontaneous emission of the laser transition in the afterglow is considerably enhanced by the addition of Helium. Resonant transfer of energy between Helium $2s^3S$ metastables and Krypton ground state ions is the excitation process which populates the upper laser levels. The ground state Krypton ion population is created by direct excitation and also by Helium-Krypton atom interactions.

**References**

[1] "Vacuum."
Edwards gas handling component catalogue, 1984.

[2] "Pirani Gauge Heads."
Edwards High Vacuum, 1985.

[3] "Photomultipliers."
Thorn EMI, Electron Tubes Ltd., 1986.

[4] "Voltage Divider Design."
Thorn EMI, Electron Tubes Ltd., 1982.

[5] "Transmitting microwave science into service."
Microwave component and waveguide catalogue,
Litton Precision Products, Slough, England, 1988.

[6] O.Svelto
"Principles of lasers."
Plenum Press, 1986.

[7] F.A.Jenkins & H.E.White
"Fundamentals of Optics."
McGraw-Hill, 1981.

[8] A.R.Striganov & N.S.Sventitskii
"Tables of spectral lines of neutral and ionised atoms."
Plenum Press, 1968.

# Chapter 7 Conclusions

The principal aim of the research reported in this thesis was to assess the feasibility of using microwave power to pump a laser. Noble gas ion lasers were chosen to study the main characteristics of a microwave excited laser discharge. Two different discharge structure designs were used, one producing a longitudinal electric field, and the other, a transverse field. Laser action is reported in Argon, and in Helium-Argon and Helium-Krypton gas mixtures, using pulsed microwave sources at discrete frequencies between 3 and 17 GHz.

A spectroscopic investigation reveals that the degree of ionisation in the microwave excited laser discharges is high. There is no evidence of double ionisation, and cascade excitation of the laser levels is minimal. As the input microwave power is increased, the laser output increases and no saturation is observed. This evidence suggests that increasing the pump power will increase the laser output power.

Analysis of the microwave discharge shows that microwave power absorption is high for the laser discharges under study. However, it seems that, at a dielectric/gas-discharge boundary, only a small amount of the incident power actually penetrates the boundary. For the microwave frequencies used and an electron density typical of a noble gas ion laser, only about 1% (or even less) of the applied power is admitted into the discharge. The two laser coupling structures reported herein both use a microwave field which is applied externally to the laser tube. This means that only a small amount of the power fed into these structures is used to drive the laser. When this is taken into

account, the observed efficiencies approach those of conventional noble gas ion lasers.

The characteristics of a microwave discharge are seen to be good for laser excitation. The concept of producing a commercial microwave excited laser is a feasible proposition, provided a more efficient technique of applying the microwave power can be found. The microwave power should be applied directly to the gas, via an electrode in the laser tube. One possible structure would use a launch electrode to produce a surface wave plasma as microwave power propagates through the gas from the electrode. Alternatively, an internal helix could be used which would produce an axial microwave electric field. To proceed any further, more research into coupler structures of these types must be undertaken.